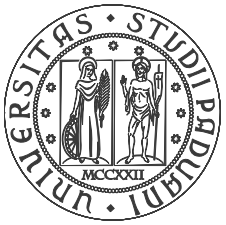

UNIVERSITÀ
DEGLI STUDI
DI PADOVA

UNIVERSITÀ DEGLI STUDI DI PADOVA

Dipartimento di Ingegneria Industriale

Scuola di Dottorato di Ricerca in Ingegneria Industriale
Curriculum in Ingegneria dell'Energia Elettrica
Ciclo XXX

Innovative Predictive Current Control for Synchronous Reluctance Machines

Direttore della Scuola:
Ch.mo Prof. Paolo Colombo

Coordinatore d'Indirizzo:
Prof. Roberto Turri

Supervisore:
Ch.mo Prof. Silverio Bolognani

Dottorando: Ing. Davide Da Rù

31 Ottobre 2017

Contents

Preface **1**

1 Synchronous Reluctance Machine **5**

1.1 Introduction 5

1.2 General model of the doubly-fed three phase machine 6

1.2.1 Energy equations 8

1.2.2 Equation without saturation 9

1.3 General model of the doubly-fed two phase machine 11

1.3.1 Energy equations 13

1.3.2 Model without saturation 14

1.4 Synchronous Reluctance Machine 16

1.4.1 Energy equations 17

1.4.2 Model without saturation 17

1.4.3 Machine with sinusoidally distributed windings 18

1.5 Conclusions 20

2 Predictive Current Control **21**

2.1 Introduction 21

2.2 Predictive Current Control 23

2.2.1 Cost function 24

2.2.2 Model-Based PCC 28

2.2.3 Effect of parameter mismatch and variation 29

2.2.4 Model-Free PCC 31

2.3 Conclusion 36

3 Avoiding stagnation in Model-free Predictive Current Control 37
3.1 Introduction . . . 37
3.2 Analysis of stagnation effects . . . 38
3.3 Proposed anti-stagnation method . . . 40
3.4 Sequence Identification . . . 44
3.5 Model validation . . . 46
3.6 Limitations and inherent stagnation . . . 49
3.7 Startup . . . 53
3.8 Conclusions . . . 54

4 Model Predictive Hysteresis Current Control 57
4.1 Introduction . . . 57
4.2 Proposed control scheme . . . 59
4.2.1 Speed loop . . . 59
4.2.2 Operating line . . . 59
4.2.3 MP-HCC logic . . . 61
4.2.4 Voltage loop . . . 63
4.3 Implementation and Results . . . 65
4.4 Conclusions . . . 69

Conclusions 71

Future works 75

Bibliography 77

Acknowledgments 81

Preface

This Preface describes the motivation and the main contributions of the thesis. The contents of each chapter of the thesis are briefly summarized. Finally, a list of publications of the author is reported.

Background

In recent decades, the use of power converters has become very popular in the field of electric drives. Several control techniques have been proposed for power converters and every year, the ongoing research and the always more powerful microprocessors, lead to new high performance solutions. Despite this, since the output of the worldwide research often results in complex and hardly applicable solutions, other well-established techniques, such as linear and hysteresys control with pulsewidth modulation, are still the main choice in a great number of industrial applications. The reasons of their leadership can be found considering the characteristics of these methods: on one side simplicity of comprehension and implementation and, on the other, sufficiently good performance and robustness. Due to these relevant features, despite there is still extensive room for improvements, it is not painless to propose solutions that can be attractive for people working in industry and to compete with, and possibly to replace, traditional methods.

Desirably, a control algorithm for electric drives has to be simple and easily understandable. Besides, it has to be suitable for real-time applications. Robustness and reliability, beyond that performance, have to be guaranteed since the nature of the different applications, e.g. home appliances and automotive.

In this perspective, Predictive Control could represent a candidate to introduce improvements and gains in the aforementioned industrial applications. Predictive control is a wide class of controllers that uses the model of the system for the prediction of the future behavior of the controlled variables. This information is used by the regulator in order to obtain the optimal actuation, according to a predefined optimization criterion represented by a cost function. This control techique is based on concepts that are extremely simple and intuitive and besides, depending on the type of predictive control, the implementation can also be simple. In particular, Finite Control Set allows considering the discrete nature of the power converter and results in an extremely simple implementation. Beyond simplicity, other advantages can be recognized. First, with

predictive control it is possible to avoid the cascaded structure obtaining a very fast transient response. Besides, nonlinearities can be included in the model avoiding the need of linearizing the model for a given operating point and improving the operation of the system for all conditions. Finally, it is possible to include limitations of the variables when designing the regulator.

The aim of this thesis is to study Predictive Control applied to the current control of synchronous machines, analysing and addressing some open research topics regarding this kind of control. In particular, two main aspects are studied, namely the need of a precise knowledge of the machine model and the possibility to drive a synchronous machine along the Maximum Torque per Ampere, the Flux Weakening and the Maximum Torque per Voltage operations.

The performance are strictly related to the accuracy of the model used for the prediction. In case of parameters mismatch or variation, rather than other model inadequacies, the prediction could be affected causing a worsening of the overall behaviour of the drive. The first part of this work is commited to study this aspect, analysing the effects of mismatches and variations focusing in particular on the detrimental effects of iron saturation. A novel model-free solution is presented to overcome the limitations given by an inadequate model.

In order to fully exploit the characteristics of the drive while assuring the lowest power losses in every working condition, a proper control algorithm has to be used. In the second part of this work, a predictive regulator able to track the most suitable trajectory depending on the machine operation is presented. The proposal is a combination of predictive control and hysteresis control since its aim is to keep the current error within a certain hysteresis band.

This study is carried out considering Predictive Current Control for Synchronous Reluctance machines. This kind of machine is of great interest due to the fact that it features high power density, superior reliability, high efficiency and it is cost effective due to the absence of permanent magnets and circuits in the rotor. Besides, since the significant iron saturation, its control represents a challenge (in particular) for predictive control schemes and for this reason it is a perfect case study.

Outline of the thesis

Hereafter, the contents of the each Chapter of the thesis are briefly described:

Chapter 1 The model of the synchronous reluctance machine is derived and described. The electrical equations are first obtained considering a doubly-fed three phase machine that is the most general representation for an electrical machine. The model is developed with the only assumption of no hysteresis and no eddy currents. After that, the case of linearity, i.e. with no iron saturation effects, is studied. The three phase system is later transformed in the equivalent two phase machine. Finally, a specific representation for the reluctance machine is obtained by imposing appropriate conditions on the rotor currents.

Chapter 2 The Predictive Current Control is presented starting with an overview of the main features. After that, the system is described considering the specific

case of synchronous reluctance machine applications. Some considerations on the choice of the cost function are provided to avoid improper operations when controlling an anisotropic machine. The remainder of the chapter describes Model-based and Model-free prediction. The former is presented and analysed including the effect of parameters mismatch. In particular, the effects of iron saturation on the predictive regulator are presented. Model-free prediction is introduced highlighting the merits of this technique. Besides, the so called voltage vector stagnation is analyzed.

Chapter 3 Model-free predictive schemes suffer from voltage vector stagnation. The latter occurs when a value of current variation is not updated for several steps. This phenomenon leads to an imprecise current prediction and, if its effects persist, instabilities and loss of control could occur. In this, chapter a novel anti-stagnation solution is presented. The proposed method allows a continuous update without forcing non optimal voltage vectors.

Chapter 4 A predictive control scheme for the wide speed operation of the synchronous reluctance machine is presented. The algorithm belongs to both predictive control and hysteresis control, since its aim is keeping the current error within a tolerance band. The proposed scheme is able to control the machine along the Maximum Torque per Ampere, the Flux-Weakening and the Maximum Torque per Voltage trajectories. The different operations are obtained introducing the operating line, i.e. a locus of operating points located between the MTPA and the MTPV.The transition between the different loci is obtained by mean of an innovative voltage loop that does not require the knowledge of the base speed.

List of publications

Several parts of this Ph.D. thesis have been presented by the author during his Ph.D. course in international conferences and journals. The list of publications is here reported.

- M. De Soricellis, **D. Da Rù** and S. Bolognani, "*A Robust Current Control Based on Proportional-Integral Observers for Permanent Magnet Synchronous Machines*", 2017 IEEE Transactions on Industry Applications, *In Press.*
- M. De Soricellis, **D. Da Rù** and S. Bolognani, "*Real-time disturbance compensation algorithm for the current control of PMSM drives*", 2017 IEEE Energy Conversion Congress and Exposition (ECCE), Cincinnati, OH, 1-5 October 2017.
- V. Manzolini, **D. Da Rù** and S. Bolognani, "*An Effective Voltage Control Loop for a Deep Flux-Weakening in IPM Synchronous Motor Drives*", 2017 IEEE Energy Conversion Congress and Exposition (ECCE), Cincinnati, OH, 1-5 October 2017.
- F. Toso, **D. Da Rù** and S. Bolognani, "*A Moving Horizon Estimator for the Speed and Rotor Position of Sensorless PMSM Drive*", 2017 IEEE Symposium on Sensorless Control for Electrical Drives (SLED), Catania, Italy, 18-19 September 2017.

- **D. Da Rù**, M. Polato and S. Bolognani,"*Model-Free Predictive Current Control for a SynRM drive based on an effective update of measured current responses*", 2017 IEEE Symposium on Predictive Control of Electrical Drives and Power Electronics (PRECEDE), Pilsen, Czech Republic, 4-6 September 2017.

- V. Manzolini, **D. Da Rù** and S. Bolognani, "*A new control strategy for high efficiency wide speed range synchronous reluctance motor drives*", 2017 IEEE International Electric Machines and Drives Conference (IEMDC), Miami, FL, 2017, pp. 1-7. doi: 10.1109/IEMDC.2017.8002276

- **D. Da Rù**, M. Morandin, S. Bolognani and M. Castiello, "*Test bench for emulating a variety of salient rotor electrical propulsion machines with a single permanent-magnet synchronous machine drive*", in IET Electrical Systems in Transportation, vol. 7, no. 1, pp. 55-64, 3 2017. doi: 10.1049/iet-est.2016.0026

- M. De Soricellis,**D. Da Rù** and S. Bolognani, "*A robust current control based on proportional-integral observers for permanent magnet synchronous machines*", 2016 IEEE Energy Conversion Congress and Exposition (ECCE), Milwaukee, WI, 2016, pp. 1-8. doi: 10.1109/ECCE.2016.7854768

- **D. Da Rù**, M. Morandin, S. Bolognani and M. Castiello, "*Model Predictive Hysteresis Current Control for wide speed operation of a Synchronous Reluctance machine drive*", IECON 2016 - 42nd Annual Conference of the IEEE Industrial Electronics Society, Florence, 2016, pp. 2845-2850. doi: 10.1109/IECON.2016.7793925

- M. Pulvirenti, **D. Da Rù**, N. Bianchi, G. Scarcella and G. Scelba, "*Secondary saliencies decoupling technique for self-sensing integrated multi-drives*", 2016 IEEE Symposium on Sensorless Control for Electrical Drives (SLED), Nadi, 2016, pp. 1-6. doi: 10.1109/SLED.2016.7518801

- M. Morandin, **D. Da Rù**, S. Bolognani and N. Bianchi, "*An Integrated Starter-Alternator Based on a Sensorless Synchronous Reluctance Machine Drive*", 2015 IEEE Vehicle Power and Propulsion Conference (VPPC), Montreal, QC, 2015, pp. 1-6. doi: 10.1109/VPPC.2015.7352896

- **D. Da Rù**, M. Morandin, S. Bolognani and M. Castiello, "*An SPM Motor Drive Dressed as IPM Motor Drive for a Flexible Test Bench of Salient Rotor Propulsion Machines*", 2015 IEEE Vehicle Power and Propulsion Conference (VPPC), Montreal, QC, 2015, pp. 1-6. doi: 10.1109/VPPC.2015.7352898

- M. Morandin, **D. Da Rù**, S. Bolognani and M. Castiello, "*A test bench for hybrid propulsion train research and development*", 2014 IEEE International Electric Vehicle Conference (IEVC), Florence, 2014, pp. 1-8. doi: 10.1109/IEVC.2014.7056182

Chapter 1

Synchronous Reluctance Machine

Analysing and developing control schemes requires a deep understanding of the plant physics. This chapter includes the analysis of the electrical model of a synchronous reluctance machine and it is the fundamental basis of this work.

1.1. Introduction

In this chapter, the model of a Synchronous Reluctance Machine (SynRM) is derived and described. For the sake of generality, an universal model of a synchronous machine is derived at first. It is obtained by the equations of a doubly-fed three phase machine particolarized accordingly. The latter is the most general representation for an electrical machine since it has a three phase winding on both the stator and the rotor. According to this model, the machine is described by mean of equations relating the stator and rotor voltages with the currents and fluxes. The model is developed with the only assumption of no hysteresis and no eddy currents. Besides, the electrical equations are first derived considering a general relationship between flux and currents and then by introducing the hypothesis of linearity, i.e. iron saturation is neglected.

The three phase system is later transformed in the two phase system, obtaining the equations of the doubly-fed two phase machine. The same considerations made for the three phase machine are extended for the two phase system, starting with a general model obtained with no assumptions on the magnetic behaviour of the machine and then introducing the hypothesis of linearity.

Finally, a specific representation for a reluctance machine is obtained by imposing appropriate conditions on the rotor currents. Again, the model is developed starting from the most general representation, after that the hypothesis of no iron saturation is introduced and then the equations are derived considering a sinusoidal distribution of the winding at the airgap.

1.2. General model of the doubly-fed three phase machine

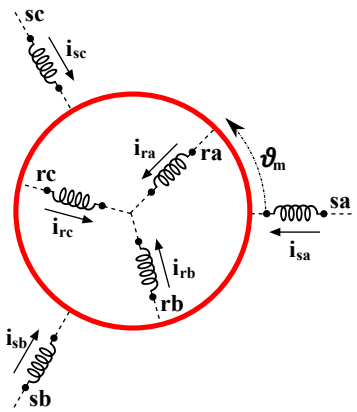

Figure 1.1: Doubly fed three phase machine representation

The general machine considered in this section, presents a three phase winding on both the stator and the rotor as shown in Fig. 1.1. The mechanical position of the rotor ϑ_m is indentified with the angle between winding sa and ra. In case of machines with multiple poles, i.e. with pole pair number $p > 1$, the relationship between the electrical and the mechanical position can be expressed as $\vartheta = p\vartheta_m$. Besides, the mechanical speed of the rotor is stated with ω_m and the electrical speed is $\omega = p\omega_m$. The electrical equations relating the voltages u, the currents i and the flux linkages λ are

$$\begin{cases} \mathbf{u}_s = \mathbf{R}_s \mathbf{i}_s + \frac{d}{dt}\boldsymbol{\lambda}_s \\ \mathbf{u}_r = \mathbf{R}_r \mathbf{i}_r + \frac{d}{dt}\boldsymbol{\lambda}_r \end{cases} \tag{1.1}$$

where $\mathbf{u}_s = [u_{sa}\ u_{sb}\ u_{sc}]^t$, $\mathbf{i}_s = [i_{sa}\ i_{sb}\ i_{sc}]^t$ and $\boldsymbol{\lambda}_s = [\lambda_{sa}\ \lambda_{sb}\ \lambda_{sc}]^t$ are the stator voltage, current and flux vectors respectively. The stator resistance matrix is defined as $\mathbf{R}_s = R_s \cdot \mathbf{I}_{3\times3}$ where $\mathbf{I}_{3\times3}$ is the identity matrix. The rotor quanties are easily defined using subscript r.

The set of six equations (1.1) represents the electric balance of each phase. The voltage at the terminals is the sum of the resistive voltage drop and the time variation of the flux coupled with the considered winding. Stator and rotor equations (1.1) can be unified in one expression as

$$\mathbf{u} = \mathbf{R}\mathbf{i} + \frac{d}{dt}\boldsymbol{\lambda} \tag{1.2}$$

where $\mathbf{u} = [\mathbf{u}_s\ \mathbf{u}_r]^t$, $\mathbf{i} = [\mathbf{i}_s\ \mathbf{i}_r]^t$, $\boldsymbol{\lambda} = [\boldsymbol{\lambda}_s\ \boldsymbol{\lambda}_r]^t$ are vectors with size 6×1. Besides, the resistance matrix $\mathbf{R}$ can be written as a block matrix

$$\mathbf{R} = \left[\begin{array}{c|c} \mathbf{R}_s & \mathbf{0}_{3\times3} \\ \hline \mathbf{0}_{3\times3} & \mathbf{R}_r \end{array}\right] \tag{1.3}$$

where $\mathbf{0}_{3\times3}$ is the null matrix.

Since the model is developed under the assumption of no hysteresis and eddy currents, the relationship that links the current and the flux linkage is bi-univocal. In

particular

$$\boldsymbol{\lambda} = \boldsymbol{\lambda}(\mathbf{i}_s, \mathbf{i}_r, \vartheta) = \begin{bmatrix} \boldsymbol{\lambda}_s(\mathbf{i}_s, \mathbf{i}_r, \vartheta) \\ \boldsymbol{\lambda}_r(\mathbf{i}_s, \mathbf{i}_r, \vartheta) \end{bmatrix} \tag{1.4}$$

and

$$\mathbf{i} = \mathbf{i}(\boldsymbol{\lambda}_s, \boldsymbol{\lambda}_r, \vartheta) = \begin{bmatrix} \mathbf{i}_s(\boldsymbol{\lambda}_s, \boldsymbol{\lambda}_r, \vartheta) \\ \mathbf{i}_r(\boldsymbol{\lambda}_s, \boldsymbol{\lambda}_r, \vartheta) \end{bmatrix} \tag{1.5}$$

For a certain position ϑ, the relationship between the flux and the current can be represented by the magnetization curve qualitatively reported in Fig. 1.2.

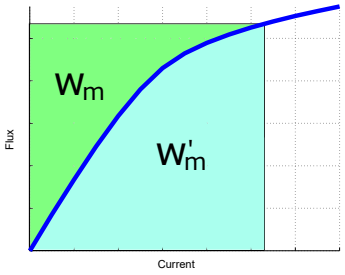

Figure 1.2: Magnetization curve

Fixed the position ϑ, the magnetic energy w_m and coenergy $w_m^{'}$ are defined as

$$\begin{aligned} w_m(\lambda, \vartheta) &= \int_0^{\lambda} i(\lambda, \vartheta) d\lambda \\ w_m^{'}(i, \vartheta) &= \int_0^{i} \lambda(i, \vartheta) di \end{aligned} \tag{1.6}$$

The geometrical meaning of these two quantities is represented in Fig. 1.2 and the relationship between them is

$$\mathbf{i}^t \boldsymbol{\lambda} = w_m + w_m^{'} \tag{1.7}$$

Since the flux linkage $\boldsymbol{\lambda}$ is a function of the currents $\mathbf{i}$ and the position ϑ, i.e. $\boldsymbol{\lambda} = \boldsymbol{\lambda}(\mathbf{i}, \vartheta)$, the electrical equation (1.2) can be rewritten splitting the flux derivative considering the partial derivatives with respect to the current and the position. It results

$$\mathbf{u} = \mathbf{R}\mathbf{i} + \boldsymbol{\ell} \frac{d}{dt}\mathbf{i} + \frac{\partial}{\partial \vartheta}\boldsymbol{\lambda} \frac{d}{dt}\vartheta \tag{1.8}$$

where $\boldsymbol{\ell}$ is the 6×6 differential inductance matrix (1.9). The latter represents the slope of the magnetization curve at the fixed current level and it can be explicitly written as

$$\boldsymbol{\ell} = \boldsymbol{\ell}(\mathbf{i}, \vartheta) = \begin{bmatrix} \frac{\partial \lambda_{sa}}{\partial i_{sa}} & \cdots & \frac{\partial \lambda_{sa}}{\partial i_{rc}} \\ \vdots & \ddots & \vdots \\ \frac{\partial \lambda_{rc}}{\partial i_{sa}} & \cdots & \frac{\partial \lambda_{rc}}{\partial i_{rc}} \end{bmatrix} \tag{1.9}$$

1.2.1. Energy equations

The energy balance can be obtained by multiplying (1.2) by $\mathbf{i}dt$. It can be expressed as

$$\underbrace{\mathbf{i}^t\mathbf{u}dt}_{dw_{in}} = \underbrace{\mathbf{i}^t\mathbf{R}\mathbf{i}dt}_{dw_J} + \underbrace{\mathbf{i}^t d\boldsymbol{\lambda}}_{dw_m+dw_{em}} \tag{1.10}$$

where dw_{in} is the input electrical energy, dw_J is the Joule loss component, dw_m is the variation of the magnetic energy stored in the system and dw_{em} is energy converted from electrical to mechanical. Under the assumption of no mechanical losses, the latter corresponds to the output mechanical work. The two latter terms of (1.10), can be easily identified starting from (1.8) and multiplying it by $\mathbf{i}dt$, as shown in (1.11).

$$\underbrace{\mathbf{i}^t\mathbf{u}dt}_{dw_{in}} = \underbrace{\mathbf{i}^t\mathbf{R}\mathbf{i}dt}_{dw_J} + \underbrace{\mathbf{i}^t\boldsymbol{\ell}d\mathbf{i}}_{dw_m} + \underbrace{\mathbf{i}^t\frac{\partial\boldsymbol{\lambda}}{\partial\vartheta}d\vartheta}_{dw_{em}} \tag{1.11}$$

Comparing (1.10) and (1.11), and imposing $dw_{em} = \tau d\vartheta_m$ it is possible to write

$$\mathbf{i}^t d\boldsymbol{\lambda} = dw_m + \tau d\vartheta_m \tag{1.12}$$

where τ is the instantaneous torque.

Since the magnetic energy is a function of the stator and rotor current beyond that the position, the infinitesimal variation dw_m can be expressed as

$$dw_m = \frac{\partial w_m}{\partial\boldsymbol{\lambda}}d\boldsymbol{\lambda} + \frac{\partial w_m}{\partial\vartheta}d\vartheta = \frac{\partial w_m}{\partial\lambda_{sa}}d\lambda_{sa} + \cdots + \frac{\partial w_m}{\partial\lambda_{ra}}d\lambda_{ra} + \cdots + \frac{\partial w_m}{\partial\vartheta}d\vartheta \tag{1.13}$$

Combining (1.12) and (1.13) it is possible to write

$$\mathbf{i}^t d\boldsymbol{\lambda} - \tau d\vartheta_m = \frac{\partial w_m}{\partial\boldsymbol{\lambda}}d\boldsymbol{\lambda} + \frac{\partial w_m}{\partial\vartheta}d\vartheta \tag{1.14}$$

Since the state variables are indipendent quantities, (1.14) can be separated and its two component can be identified as

$$\mathbf{i}(\boldsymbol{\lambda},\vartheta) = \frac{\partial w_m}{\partial\boldsymbol{\lambda}} \tag{1.15}$$

$$\tau(\boldsymbol{\lambda},\vartheta) = -p\frac{\partial w_m}{\partial\vartheta} \tag{1.16}$$

where the former represents the winding current and the latter the torque expression as a function of the magnetic energy.

The torque can be also expressed as a function of the current $\mathbf{i}$ and the position ϑ. This can be done by considering the magnetic coenergy and in particular

$$w_m'(\mathbf{i},\vartheta) = \mathbf{i}^t\boldsymbol{\lambda} - w_m(\boldsymbol{\lambda},\vartheta) \tag{1.17}$$

The new expression for the torque can be obtained by differentiating (1.17) and combining it with (1.16). The result is reported in (1.18).

$$\tau(\mathbf{i},\vartheta) = p\frac{\partial w_m'}{\partial\vartheta} \tag{1.18}$$

1.2.2. Equation without saturation

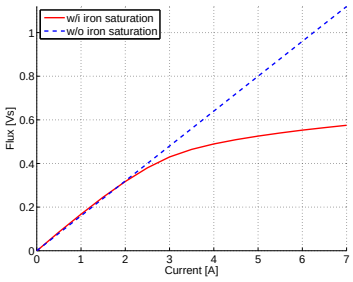

Figure 1.3: Magnetization curve in case of linearity

The model developed in Section 1.2, considers a general doubly-fed three phase machine. The equations are now specified for a linear machine, i.e. the iron saturation is neglected. The magnetization curve is qualitatively reported in Fig. 1.3. In this case, the flux can be expressed as

$$\boldsymbol{\lambda}(\mathbf{i}, \vartheta) = \mathbf{L}(\vartheta)\mathbf{i} \tag{1.19}$$

where $\mathbf{L}$ is the 6×6 inductance matrix that depends on the position and not on the currents. It can be expressed as

$$\mathbf{L} = \begin{bmatrix} \mathbf{L}_s(\vartheta) & \mathbf{M}_{sr}(\vartheta) \\ \mathbf{M}_{rs}(\vartheta) & \mathbf{L}_r(\vartheta) \end{bmatrix} \tag{1.20}$$

and its submatrices are

$$\begin{aligned} \mathbf{L}_s(\vartheta) &= \begin{bmatrix} L_{s,a}(\vartheta) & M_{s,ab}(\vartheta) & M_{s,ac}(\vartheta) \\ M_{s,ba}(\vartheta) & L_{s,b}(\vartheta) & M_{s,bc}(\vartheta) \\ M_{s,ca}(\vartheta) & M_{s,cb}(\vartheta) & L_{s,c}(\vartheta) \end{bmatrix} \\ \mathbf{M}_{sr}(\vartheta) = \mathbf{M}_{rs}^t(\vartheta) &= \begin{bmatrix} M_{sr,aa}(\vartheta) & M_{sr,ab}(\vartheta) & M_{sr,ac}(\vartheta) \\ M_{sr,ba}(\vartheta) & M_{sr,bb}(\vartheta) & M_{sr,bc}(\vartheta) \\ M_{sr,ca}(\vartheta) & M_{sr,cb}(\vartheta) & M_{sr,cc}(\vartheta) \end{bmatrix} \\ \mathbf{L}_r(\vartheta) &= \begin{bmatrix} L_{r,a}(\vartheta) & M_{r,ab}(\vartheta) & M_{r,ac}(\vartheta) \\ M_{r,ba}(\vartheta) & L_{r,b}(\vartheta) & M_{r,bc}(\vartheta) \\ M_{r,ca}(\vartheta) & M_{r,cb}(\vartheta) & L_{r,c}(\vartheta) \end{bmatrix} \end{aligned} \tag{1.21}$$

where self inductances are stated with $L(\vartheta)$, while $M(\vartheta)$ is used for the mutual inductance between two windings.

It is worth highlighting that $\mathbf{L}_s(\vartheta)$, $\mathbf{L}_r(\vartheta)$ and $\mathbf{M}_{sr}(\vartheta)$ are circulant matrix in which each row vector is shifted one element to the right with respect with the precedent row vector. As an example

- $M_{s,ab}(\vartheta) = M_{s,ba}(\vartheta)$
- $L_{s,b}(\vartheta) = L_{s,a}(\vartheta - 2/3\pi)$ and $L_{s,c}(\vartheta) = L_{s,a}(\vartheta - 4/3\pi)$

The stator and rotor flux linkage can be expressed as

$$\begin{aligned}\boldsymbol{\lambda}_s &= \mathbf{L}_s\mathbf{i}_s + \mathbf{M}_{sr}\mathbf{i}_r \\ \boldsymbol{\lambda}_r &= \mathbf{M}_{rs}\mathbf{i}_s + \mathbf{L}_r\mathbf{i}_r\end{aligned} \tag{1.22}$$

In case of linearity, the magnetic energy and coenergy are equal. In addition considering $w_m = 1/2\mathbf{i}^t\boldsymbol{\lambda}$, it possible to write

$$\begin{aligned}\tau(\mathbf{i},\vartheta) &= p\frac{\partial}{\partial\vartheta}w_m^{'}(\mathbf{i},\vartheta) = p\frac{\partial}{\partial\vartheta}w_m(\boldsymbol{\lambda},\vartheta) \\ &= \frac{1}{2}p\mathbf{i}^t\frac{\partial}{\partial\vartheta}\boldsymbol{\lambda} = \frac{1}{2}p\mathbf{i}^t\frac{d}{d\vartheta}\mathbf{L}\mathbf{i}\end{aligned} \tag{1.23}$$

The torque can be splitted in

$$\tau(\mathbf{i},\vartheta) = \underbrace{\frac{1}{2}p\mathbf{i}_s^t\left[\frac{d}{d\vartheta}\mathbf{L}_s(\vartheta)\right]\mathbf{i}_s}_{\tau_r} + \underbrace{p\mathbf{i}_s^t\left[\frac{d}{d\vartheta}\mathbf{M}_{sr}(\vartheta)\right]\mathbf{i}_r}_{\tau_{ed}} + \underbrace{\frac{1}{2}p\mathbf{i}_r^t\left[\frac{d}{d\vartheta}\mathbf{L}_r\vartheta\right]\mathbf{i}_r}_{\tau_c} \tag{1.24}$$

where τ_r is the reluctance torque, τ_{ed} the electro-dynamic torque and τ_c is the cogging torque.

The reluctance torque τ_r is related to the variations of the stator inductance matrix with the rotor position, that occurs every time the rotor has an anisotropic structure due to pole saliencies or flux barriers. It can be seen as

$$\begin{aligned}\tau_r &= \frac{1}{2}p\frac{\partial\boldsymbol{\lambda}_s^t(\mathbf{i}_s,0,\vartheta)}{\partial\vartheta}\mathbf{i}_s \\ &= \frac{1}{2}p\mathbf{i}_s^t\frac{\partial}{\partial\vartheta}\boldsymbol{\lambda}_s(\mathbf{i}_s,0,\vartheta) \\ &= p\frac{\partial}{\partial\vartheta}w_m(\mathbf{i}_s,0,\vartheta)\end{aligned} \tag{1.25}$$

where $\boldsymbol{\lambda}_s(\mathbf{i}_s,0,\vartheta)$ is the stator flux linkage due to the stator current only, i.e. $\mathbf{i}_r = 0$.

The electrodynamic torque is related to the variation of the mutual inductances between the stator and the rotor windings with the rotor position. The main reason for this variation is the movement of the rotor with respect to the stator. It can be expressed as

$$\begin{aligned}\tau_{ed}(\mathbf{i}_s,\mathbf{i}_r,\vartheta) &= p\mathbf{i}_s^t\frac{\partial\mathbf{M}_{sr}(\vartheta)}{\partial\vartheta}\mathbf{i}_r \\ &= p\frac{\partial\boldsymbol{\lambda}_{sr}^t(0,\mathbf{i}_r,\vartheta)}{\partial\vartheta}\mathbf{i}_s = p\mathbf{i}_s^t\frac{\partial}{\partial\vartheta}\boldsymbol{\lambda}_{sr}^t(0,\mathbf{i}_r,\vartheta) \\ &= p\frac{\partial\boldsymbol{\lambda}_{rs}^t(\mathbf{i}_s,0,\vartheta)}{\partial\vartheta}\mathbf{i}_r = p\mathbf{i}_r^t\frac{\partial}{\partial\vartheta}\boldsymbol{\lambda}_{rs}(\mathbf{i}_s,0,\vartheta)\end{aligned} \tag{1.26}$$

where $\boldsymbol{\lambda}_{sr}(0,\mathbf{i}_r,\vartheta)$ is the stator flux linkage due to the rotor current only, i.e. $\mathbf{i}_s = 0$, and $\boldsymbol{\lambda}_{rs}(\mathbf{i}_s,0,\vartheta)$ is the rotor flux linkage due to the stator current only, i.e. $\mathbf{i}_r = 0$.

The cogging torque is due to stator anisotropies mainly caused by the slots opening. It can be expresses as

$$\begin{aligned}\tau_{cog}(\mathbf{i}_r,\vartheta) &= \frac{1}{2}p\mathbf{i}_r^t\frac{\partial\mathbf{L}_r(\vartheta)}{\partial\vartheta}\mathbf{i}_r \\ &= \frac{1}{2}p\frac{\partial\boldsymbol{\lambda}_r^t(0,\mathbf{i}_r,\vartheta)}{\partial\vartheta}\mathbf{i}_r \\ &= \frac{1}{2}p\mathbf{i}_r^t\frac{\partial\boldsymbol{\lambda}_r^t(0,\mathbf{i}_r,\vartheta)}{\partial\vartheta} \\ &= p\frac{\partial w_m(0,\mathbf{i}_r,\vartheta)}{\partial\vartheta}\end{aligned} \tag{1.27}$$

where $\boldsymbol{\lambda}_r(0,\mathbf{i}_r,\vartheta)$ is the stator flux linkage due to the rotor current only, i.e. $\mathbf{i}_s = 0$.

1.3. General model of the doubly-fed two phase machine

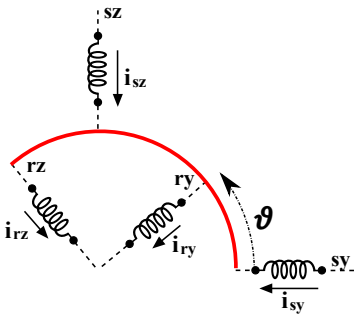

Figure 1.4: Doubly fed two phase machine representation

The three-phase winding on the stator and on the rotor can be studied considering an equivalent two phase system yz represented in Fig. 1.4. Here, both windings are transformed in the equivalent two phase system.

- The transformation is expressed for a general three-phase winding abc rotating with an angular speed ω_{abc}. The position of the phase a with respect to the abscissa axis is ϑ_{abc}.
- The two-phase reference frame yz is rotating with an angular speed of ω_{yz}. The position of the phase y with respect to the abscissa axis is ϑ_{yz}.
- the homopolar component is assumed to be zero.

The relationship between the three-phase abc and the two-phase yz systems can be expressed as

$$\mathbf{f}_{yz} = \mathbf{T}\mathbf{f}_{abc} \quad \Longrightarrow \quad \mathbf{f}_{abc} = \mathbf{T}^{-1}\mathbf{f}_{yz} \tag{1.28}$$

where $\mathbf{f}$ is used to represent a general quantity, e.g. the voltage, the current and the flux, while subscripts abc and yz refer to the three-phase and the two-phase system

respectively. $\mathbf{T}$ is the transformation matrix with size 2×3 and $\mathbf{T}^{-1}$ is the inverse matrix. They can be expressed as

$$\begin{aligned}\mathbf{T}(\Delta\vartheta) &= \begin{bmatrix} cos[\Delta\vartheta] & cos[\Delta\vartheta - 2/3\pi] & cos[\Delta\vartheta + 2/3\pi] \\ -sin[\Delta\vartheta] & -sin[\Delta\vartheta - 2/3\pi] & -sin[\Delta\vartheta + 2/3\pi] \end{bmatrix} \\ \mathbf{T}^{-1}(\Delta\vartheta) &= \begin{bmatrix} cos[\Delta\vartheta] & -sin[\Delta\vartheta] \\ cos[\Delta\vartheta - 2/3\pi] & -sin[\Delta\vartheta - 2/3\pi] \\ cos[\Delta\vartheta + 2/3\pi] & -sin[\Delta\vartheta + 2/3\pi] \end{bmatrix}\end{aligned} \tag{1.29}$$

where $\Delta\vartheta = \vartheta_{yz} - \vartheta_{abc}$. In the following, the dependency on $\Delta\vartheta$ is omitted. It is worth highlighting that the inverse matrix can be found by reintroducing the third row in the matrix $\mathbf{T}$, i.e. considering the homopolar component. In this way, the trasformation matrix is a square 3×3 matrix and its inverse can be written as in (1.29), where the homopolar component is again omitted after the inversion.

Starting from the equation of the three-phase winding and using (1.28), it possible to write

$$\begin{aligned}\mathbf{u}_{abc} &= \mathbf{R}\mathbf{i}_{abc} + \frac{d}{dt}\boldsymbol{\lambda}_{abc} \\ \mathbf{T}^{-1}\mathbf{u}_{yz} &= \mathbf{R}\mathbf{T}^{-1}\mathbf{i}_{yz} + \frac{d}{dt}\left(\mathbf{T}^{-1}\boldsymbol{\lambda}_{yz}\right) \\ \mathbf{T}^{-1}\mathbf{u}_{yz} &= \mathbf{R}\mathbf{T}^{-1}\mathbf{i}_{yz} + \mathbf{T}^{-1}\frac{d}{dt}\boldsymbol{\lambda}_{yz} + \frac{d}{dt}\left(\mathbf{T}^{-1}\right)\boldsymbol{\lambda}_{yz}\end{aligned} \tag{1.30}$$

The derivative of the transformation matrix is obtained by an element-by-element derivation

$$\begin{aligned}\frac{d}{dt}\left(\mathbf{T}^{-1}\right) &= (\omega_{yz} - \omega_{abc}) \begin{bmatrix} -sin[\Delta\vartheta] & -cos[\Delta\vartheta] \\ -sin[\Delta\vartheta - 2/3\pi] & -cos[\Delta\vartheta - 2/3\pi] \\ -sin[\Delta\vartheta + 2/3\pi] & -cos[\Delta\vartheta + 2/3\pi] \end{bmatrix} \\ &= (\omega_{yz} - \omega_{abc})\mathbf{T}^{-1}\mathbf{J}\end{aligned} \tag{1.31}$$

where

$$\mathbf{J} = \begin{bmatrix} 0 & -1 \\ -1 & 0 \end{bmatrix} \tag{1.32}$$

Combining (1.30) and (1.31), it is possible to write

$$\begin{aligned}\mathbf{T}^{-1}\mathbf{u}_{yz} &= \mathbf{R}\mathbf{T}^{-1}\mathbf{i}_{yz} + \mathbf{T}^{-1}\frac{d}{dt}\boldsymbol{\lambda}_{yz} + \mathbf{T}^{-1}\mathbf{J}\boldsymbol{\lambda}_{yz}(\omega_{yz} - \omega_{abc}) \\ \mathbf{u}_{yz} &= \mathbf{R}\mathbf{i}_{yz} + \frac{d}{dt}\boldsymbol{\lambda}_{yz} + \mathbf{J}\boldsymbol{\lambda}_{yz}(\omega_{yz} - \omega_{abc})\end{aligned} \tag{1.33}$$

It is worth mentioning that (1.33) is valid for both the stator and the rotor. They can be differentiated by imposing the speed of the two systems, namely $\omega_{abc} = 0$ and $\omega_{abc} = \omega$ for the stator and the rotor respectively.

In the analysis of the synchronous machine, two particular transformations are extensively used, namely the Clarke and the Park transformations. The first is obtained

considering a two-phase stationary winding named $\alpha\beta$ with $\omega_{yz} = 0$. In this case, the axis representing the coil α is aligned with the phase a. The transformation matrix can be rewritten considering $\vartheta_{yz} = \vartheta_{abc}$ and $\omega_{yz} = \omega_{abc} = 0$ and the equations are

$$\begin{cases} \mathbf{u}_{s,\alpha\beta} &= \mathbf{R}\mathbf{i}_{s,\alpha\beta} + \frac{d}{dt}\boldsymbol{\lambda}_{s,\alpha\beta} \\ \mathbf{u}_{r,\alpha\beta} &= \mathbf{R}\mathbf{i}_{r,\alpha\beta} + \frac{d}{dt}\boldsymbol{\lambda}_{r,\alpha\beta} - \omega\mathbf{J}\boldsymbol{\lambda}_{r,\alpha\beta} \end{cases} \tag{1.34}$$

The second useful transformation is obtained considering a two-phase winding named dq synchronously rotating with the rotor. In this case the transformation matrix can be obtained with $\omega_{yz} = \omega$ and the equations are

$$\begin{cases} \mathbf{u}_{s,dq} &= \mathbf{R}\mathbf{i}_{s,dq} + \frac{d}{dt}\boldsymbol{\lambda}_{s,dq} + \omega\mathbf{J}\boldsymbol{\lambda}_{s,dq} \\ \mathbf{u}_{r,dq} &= \mathbf{R}\mathbf{i}_{r,dq} + \frac{d}{dt}\boldsymbol{\lambda}_{r,dq} \end{cases} \tag{1.35}$$

To derive a more general expression that includes both the stator and the rotor equations, the transformation matrix $\mathbf{P}$, with size 4×6, is defined as

$$\mathbf{P} = \begin{bmatrix} \mathbf{T}(\vartheta_{yz}) & \mathbf{0}_{2\times3} \\ \mathbf{0}_{2\times3} & \mathbf{T}(\vartheta_{yz} - \vartheta) \end{bmatrix} \tag{1.36}$$

and its inverse

$$\mathbf{P}^{-1} = \begin{bmatrix} \mathbf{T}^{-1}(\vartheta_{yz}) & \mathbf{0}_{3\times2} \\ \mathbf{0}_{3\times2} & \mathbf{T}^{-1}(\vartheta_{yz} - \vartheta) \end{bmatrix} \tag{1.37}$$

that are obtained considering the position of the stator winding $\vartheta_{abc} = 0$ as represented in Fig. 1.4. The inversion of $\mathbf{P}$ can be obained by reintroducing the homopolar component. In this way, the matrix is square with size 6×6. After the inversion, the homopolar component is omitted again. In this way, (1.2) can be rewritten as

$$\mathbf{u}_{yz} = \mathbf{R}\mathbf{i}_{yz} + \frac{d}{dt}\boldsymbol{\lambda}_{yz} + \mathbf{G}\boldsymbol{\lambda}_{yz} \tag{1.38}$$

where

$$\mathbf{G} = \begin{bmatrix} 0 & -\omega_{yz} & 0 & 0 \\ \omega_{yz} & 0 & 0 & 0 \\ 0 & 0 & 0 & -(\omega_{yz} - \omega) \\ 0 & 0 & \omega_{yz} - \omega & 0 \end{bmatrix} \tag{1.39}$$

1.3.1. Energy equations

The energy balance for a two phase machine can be obtained multiplying (1.38) by $\mathbf{i}_{yz}dt$.

$$\underbrace{\mathbf{i}_{yz}^t\mathbf{u}_{yz}dt}_{dw_{in}} = \underbrace{\mathbf{i}_{yz}^t\mathbf{R}\mathbf{i}_{yz}dt}_{dw_J} + \underbrace{\mathbf{i}_{yz}^t d\boldsymbol{\lambda}_{yz} + \mathbf{i}_{yz}^t\mathbf{G}\boldsymbol{\lambda}_{yz}dt}_{dw_m + dw_{em}} \tag{1.40}$$

The variation of the stored energy and the mechanical energy output can be written as

$$\frac{3}{2}\mathbf{i}_{yz}^t d\boldsymbol{\lambda}_{yz} + \mathbf{i}_{yz}^t\mathbf{G}\boldsymbol{\lambda}_{yz}dt = dw_m + \tau d\vartheta_m \tag{1.41}$$

The electromagnetic torque τ can be expressed starting from the energy balance as

$$\tau = \frac{1}{\omega_m}\left[\omega_{yz}(\lambda_{sy}i_{sz} - \lambda_{sz}i_{sy}) + (\omega_{yz} - \omega)(\lambda_{ry}i_{rz} - \lambda_{rz}i_{ry})\right] + p\mathbf{i}_{yz}^t\frac{\partial\boldsymbol{\lambda}_{yz}}{\partial\vartheta} - p\frac{d}{d\vartheta}w_m \quad (1.42)$$

where ω_m is the mechanical speed of the rotor, defined as $\omega_m = \omega/p$.

Besides, considering the relationship between magnetic energy and coenergy $w_m + w_m^{'} = \mathbf{i}^t\boldsymbol{\lambda}$, the equation becomes

$$\tau = \frac{1}{\omega_m}\left[\omega_{yz}(\lambda_{sy}i_{sz} - \lambda_{sz}i_{sy}) + (\omega_{yz} - \omega)(\lambda_{ry}i_{rz} - \lambda_{rz}i_{ry})\right] + p\frac{\partial}{\partial\vartheta}w_m^{'} \quad (1.43)$$

1.3.2. Model without saturation

The same considerations presented in Section 1.2.2 for the unsaturated three phase machine can be done for the two phase equivalent machine. In particular, the relationship (1.19) linking the flux and the current is still valid and the two phase system can be obtained by mean of the transformation matrix $\mathbf{P}$ as follows

$$\begin{aligned}\boldsymbol{\lambda}(\mathbf{i},\vartheta) &= \mathbf{L}(\vartheta)\mathbf{i}\\ \mathbf{P}^{-1}\boldsymbol{\lambda}_{yz}(\mathbf{i},\vartheta) &= \mathbf{L}(\vartheta)\mathbf{P}^{-1}\mathbf{i}_{yz}\\ \boldsymbol{\lambda}_{yz}(\mathbf{i},\vartheta) &= \underbrace{\mathbf{P}\mathbf{L}(\vartheta)\mathbf{P}^{-1}}_{\mathbf{L}_{yz}(\vartheta)}\mathbf{i}_{yz}\end{aligned} \quad (1.44)$$

and the inductance matrix can be expressed as

$$\begin{aligned}\mathbf{L}_{yz} &= \mathbf{P}\mathbf{L}(\vartheta)\mathbf{P}^{-1}\\ &= \begin{bmatrix}\mathbf{T}(\vartheta_{yz}) & \mathbf{0}_{2\times3}\\ \mathbf{0}_{2\times3} & \mathbf{T}(\vartheta_{yz}-\vartheta)\end{bmatrix}\begin{bmatrix}\mathbf{L}_s(\vartheta) & \mathbf{M}_{sr}(\vartheta)\\ \mathbf{M}_{rs}(\vartheta) & \mathbf{L}_r(\vartheta)\end{bmatrix}\begin{bmatrix}\mathbf{T}^{-1}(\vartheta_{yz}) & \mathbf{0}_{3\times2}\\ \mathbf{0}_{3\times2} & \mathbf{T}^{-1}(\vartheta_{yz}-\vartheta)\end{bmatrix}\\ &= \begin{bmatrix}\mathbf{T}(\vartheta_{yz})\mathbf{L}_s(\vartheta)\mathbf{T}^{-1}(\vartheta_{yz}) & \mathbf{T}(\vartheta_{yz})\mathbf{M}_{sr}(\vartheta)\mathbf{T}^{-1}(\vartheta_{yz}-\vartheta)\\ \mathbf{T}(\vartheta_{yz}-\vartheta)\mathbf{M}_{rs}(\vartheta)\mathbf{T}^{-1}(\vartheta_{yz}) & \mathbf{T}(\vartheta_{yz}-\vartheta)\mathbf{L}_r(\vartheta)\mathbf{T}^{-1}(\vartheta_{yz}-\vartheta)\end{bmatrix}\\ &= \begin{bmatrix}\mathbf{L}_{s,yz} & \mathbf{M}_{sr,yz}\\ \mathbf{M}_{rs,yz} & \mathbf{L}_{r,yz}\end{bmatrix}\end{aligned} \quad (1.45)$$

where

$$\begin{aligned}\mathbf{L}_{s,yz} &= \mathbf{T}(\vartheta_{yz})\mathbf{L}_s(\vartheta)\mathbf{T}^{-1}(\vartheta_{yz})\\ \mathbf{M}_{sr,yz} &= \mathbf{M}_{rs,yz}^t = \mathbf{T}(\vartheta_{yz})\mathbf{M}_{sr}(\vartheta)\mathbf{T}^{-1}(\vartheta_{yz}-\vartheta)\\ &= \mathbf{T}(\vartheta_{yz}-\vartheta)\mathbf{M}_{rs}(\vartheta)\mathbf{T}^{-1}(\vartheta_{yz})\\ \mathbf{L}_{r,yz} &= \mathbf{T}(\vartheta_{yz}-\vartheta)\mathbf{L}_r(\vartheta)\mathbf{T}^{-1}(\vartheta_{yz}-\vartheta)\end{aligned} \quad (1.46)$$

It is worth mentioning that (1.45) and (1.46) are totally general and are valid for every choice of the reference frame. The matrixes in (1.46) are not explicitly expressed since their complicated form does not provide useful informations. The precise expression will be given considering the Clarke and Park transformations.

If the Clarke transformation is performed, i.e. $\omega_{yz} = 0$, the equivalent inductance matrix is

$$\mathbf{L}_{\alpha\beta} = \begin{bmatrix} \mathbf{L}_{s,\alpha\beta} & \mathbf{M}_{sr,\alpha\beta} \\ \mathbf{M}_{rs,\alpha\beta} & \mathbf{L}_{r,\alpha\beta} \end{bmatrix} \tag{1.47}$$

where

$$\begin{aligned} \mathbf{L}_{s,\alpha\beta} &= \begin{bmatrix} L_{s,\alpha} & L_{s,\alpha\beta} \\ L_{s,\beta\alpha} & L_{s,\beta} \end{bmatrix} \quad \mathbf{M}_{sr,\alpha\beta} = \mathbf{M}_{rs,\alpha\beta} = \begin{bmatrix} M_{sr,\alpha\alpha} & M_{sr,\alpha\beta} \\ M_{sr,\beta\alpha} & M_{sr,\beta\beta} \end{bmatrix} \\ \mathbf{L}_{r,\alpha\beta} &= \begin{bmatrix} L_{r,\alpha} & L_{r,\alpha\beta} \\ L_{r,\beta\alpha} & L_{r,\beta} \end{bmatrix} \end{aligned} \tag{1.48}$$

and

$$\begin{aligned} L_{s,\alpha} &= \frac{1}{6}(4L_{s,a} + L_{s,b} + L_{s,c} - 4M_{s,ab} - 4M_{s,ac} + 2M_{s,bc}) \\ L_{s,\alpha\beta} = L_{s,\beta\alpha} &= \frac{-L_{s,b} + L_{s,c} + 2M_{s,ab} - 2M_{s,ac}}{2\sqrt{3}} \\ L_{s,\beta} &= \frac{1}{2}(L_{s,b} + L_{s,c} - 2M_{s,bc}) \end{aligned} \tag{1.49}$$

$$\begin{aligned} M_{sr,\alpha\alpha} &= \frac{1}{6}(4M_{sr,aa} + M_{sr,bb} + M_{sr,cc} - 4M_{sr,ab} - 4M_{sr,ac} + 2M_{sr,bc}) \\ M_{sr,\alpha\beta} = M_{sr,\beta\alpha} &= \frac{-M_{sr,bb} + M_{sr,cc} + 2M_{sr,ab} - 2M_{sr,ac}}{2\sqrt{3}} \\ M_{sr,\beta\beta} &= \frac{1}{2}(M_{sr,bb} + M_{sr,cc} - 2M_{sr,bc}) \end{aligned} \tag{1.50}$$

$$\begin{aligned} L_{r,\alpha} &= \frac{1}{6}(4L_{r,a} + L_{r,b} + L_{r,c} - 4M_{r,ab} - 4M_{r,ac} + 2M_{r,bc}) \\ L_{r,\alpha\beta} = L_{r,\beta\alpha} &= \frac{-L_{r,b} + L_{r,c} + 2M_{r,ab} - 2M_{r,ac}}{2\sqrt{3}} \\ L_{r,\beta} &= \frac{1}{2}(L_{r,b} + L_{r,c} - 2M_{r,bc}) \end{aligned} \tag{1.51}$$

In this reference frame the torque (1.24) can be rewritten as

$$\begin{aligned} \tau(\mathbf{i}_{\alpha\beta}, \vartheta) = &\underbrace{\frac{1}{2} p \mathbf{i}_{s,\alpha\beta}^t \left[\frac{d}{d\vartheta} \mathbf{L}_{s,\alpha\beta}(\vartheta) \right] \mathbf{i}_{s,\alpha\beta}}_{\tau_r} + \underbrace{p \mathbf{i}_{s,\alpha\beta}^t \left[\frac{d}{d\vartheta} \mathbf{M}_{sr,\alpha\beta}(\vartheta) \right] \mathbf{i}_{r,\alpha\beta}}_{\tau_{ed}} \\ &+ \underbrace{\frac{1}{2} p \mathbf{i}_{r,\alpha\beta}^t \left[\frac{d}{d(\vartheta)} \mathbf{L}_{r,\alpha\beta} \vartheta \right] \mathbf{i}_{r,\alpha\beta}}_{\tau_c} \end{aligned} \tag{1.52}$$

Differently, if the Park transformation is performed the inductance matrix can be written as

$$\mathbf{L}_{dq} = \begin{bmatrix} \mathbf{L}_{s,dq} & \mathbf{M}_{sr,dq} \\ \mathbf{M}_{rs,dq} & \mathbf{L}_{r,dq} \end{bmatrix} \tag{1.53}$$

Starting from (1.43), and considering $\omega_{yz} = \omega$, the torque can be rewritten as

$$\begin{aligned} \tau &= \frac{1}{\omega_m}\left[\omega(\lambda_{sd} i_{sq} - \lambda_{sq} i_{sd})\right] + p\frac{\partial}{\partial \vartheta} w_m^{'} \\ \tau &= p(\lambda_{sd} i_{sq} - \lambda_{sq} i_{sd}) + p\frac{\partial}{\partial \vartheta} w_m^{'} \end{aligned} \tag{1.54}$$

Under the assumption of linearity the energy and the coenergy are equal, and

$$\frac{\partial}{\partial \vartheta} w_m^{'} = \frac{\partial}{\partial \vartheta} w_m = \frac{1}{2}\mathbf{i}^t \frac{\partial}{\partial \vartheta}\boldsymbol{\lambda} = \frac{1}{2}\mathbf{i}^t \frac{\partial}{\partial \vartheta}\mathbf{L}\mathbf{i} \tag{1.55}$$

The coenergy can be written as

$$\frac{\partial}{\partial \vartheta} w_m^{'} = \frac{1}{2}\mathbf{i}_{s,dq}^t \frac{d}{d\vartheta}\mathbf{L}_{s,dq}\mathbf{i}_{s,dq} + \mathbf{i}_{s,dq}^t \frac{d}{d\vartheta}\mathbf{M}_{sr,dq}\mathbf{i}_{r,dq} + \frac{1}{2}\mathbf{i}_{r,dq} \frac{d}{dt}\mathbf{L}_{r,dq}\mathbf{i}_{r,dq} \tag{1.56}$$

Putting together (1.54) and (1.56), it is possible to obtain

$$\begin{aligned} \tau &= p(\lambda_{sd} i_{sq} - \lambda_{sq} i_{sd}) \\ &+ \frac{1}{2} p\mathbf{i}_{s,dq}^t \frac{d}{d\vartheta}\mathbf{L}_{s,dq}\mathbf{i}_{s,dq} + p\mathbf{i}_{s,dq}^t \frac{d}{d\vartheta}\mathbf{M}_{sr,dq}\mathbf{i}_{r,dq} + \frac{1}{2} p\mathbf{i}_{r,dq} \frac{d}{dt}\mathbf{L}_{r,dq}\mathbf{i}_{r,dq} \end{aligned} \tag{1.57}$$

1.4. Synchronous Reluctance Machine

The model to describe a reluctance machine is obtained setting the excitation currents of the rotor equal to zero. It follows that, in the three phase system, the currents are:

$$\mathbf{i}_r = \begin{bmatrix} 0 & 0 & 0 \end{bmatrix}^t \tag{1.58}$$

Similarly, in the equivalent two phase machine

$$\mathbf{i}_{r,yz} = \begin{bmatrix} 0 & 0 \end{bmatrix}^t \tag{1.59}$$

Obviously, the electrical equation in case of a SynRM, and in general for every machine without rotor windings, only includes the stator quantities

$$\mathbf{u}_s = \mathbf{R}_s \mathbf{i}_s + \frac{d}{dt}\boldsymbol{\lambda}_s \tag{1.60}$$

Since only one winding is present, i.e. the one on the stator, the subscript s is omitted in vector notation hereafter.

The same relationship between flux and current can be expressed as in the case of doubly-fed three phase machine

$$\boldsymbol{\lambda} = \boldsymbol{\lambda}(\mathbf{i}, \vartheta) \tag{1.61}$$

and

$$\mathbf{i} = \mathbf{i}(\boldsymbol{\lambda}, \vartheta) \tag{1.62}$$

Combining the electrical equation with the relationship linking current and flux, the same expression (1.8) can be obtained. The only difference is that, in case of SynRM, the differential inductance matrix has size 3×3, and can be expressed as

$$\boldsymbol{\ell} = \boldsymbol{\ell}(\mathbf{i}, \vartheta) = \begin{bmatrix} \frac{\partial \lambda_{sa}}{\partial i_{sa}} & \cdots & \frac{\partial \lambda_{sa}}{\partial i_{sc}} \\ \vdots & \ddots & \vdots \\ \frac{\partial \lambda_{sc}}{\partial i_{sa}} & \cdots & \frac{\partial \lambda_{sc}}{\partial i_{sc}} \end{bmatrix} \tag{1.63}$$

1.4.1. Energy equations

The results obtained with the case of doubly-fed three phase machine can be easily extended to the case of SynRM. The energy balance is obtained multiplying the electrical equation (1.60) by $\mathbf{i}dt$. The result is (1.10).

In the same way it has been done in Sec. 1.2.1, it is possible to write

$$\mathbf{i}^t d\boldsymbol{\lambda} = dw_m + \tau d\vartheta_m \tag{1.64}$$

Differently, (1.13) has to be modified since the magnetic energy is a function of the position and the stator current only

$$dw_m = \frac{\partial w_m}{\partial \boldsymbol{\lambda}} d\boldsymbol{\lambda} + \frac{\partial w_m}{\partial \vartheta} d\vartheta = \frac{\partial w_m}{\partial \lambda_{sa}} d\lambda_{sa} + \cdots + \frac{\partial w_m}{\partial \lambda_{sc}} d\lambda_{sc} + \cdots + \frac{\partial w_m}{\partial \vartheta} d\vartheta \tag{1.65}$$

Combining (1.64) and (1.65) it is possible to write

$$\mathbf{i}^t d\boldsymbol{\lambda} - \tau d\vartheta_m = \frac{\partial w_m}{\partial \boldsymbol{\lambda}} d\boldsymbol{\lambda} + \frac{\partial w_m}{\partial \vartheta} d\vartheta \tag{1.66}$$

that can be separated and its two component

$$\mathbf{i}(\boldsymbol{\lambda}, \vartheta) = \frac{\partial w_m}{\partial \boldsymbol{\lambda}} \tag{1.67}$$

$$\tau(\boldsymbol{\lambda}, \vartheta) = -p \frac{\partial w_m}{\partial \vartheta} \tag{1.68}$$

where the former represents the winding current and the latter the torque expression.

The torque can be also expressed as a function of the current $\mathbf{i}$ and the position ϑ obtaining (1.18).

1.4.2. Model without saturation

In this section, the model of a SynRM is developed considering a linear magnetic curve as in Fig. 1.3. The results are obtained as an extension of the considerations made for the doubly-fed three phase machine.

In case of no saturation, the flux can be expressed as (1.19), where $\mathbf{L}$ is the 3×3 inductance matrix that can be written as

$$\boldsymbol{\lambda}(\mathbf{i}, \vartheta) = \mathbf{L}(\vartheta)\mathbf{i} \tag{1.69}$$

where $\mathbf{L}$ is the 3×3 inductance matrix that can be written as

$$\mathbf{L} = \begin{bmatrix} L_{s,a}(\vartheta) & M_{s,ab}(\vartheta) & M_{s,ac}(\vartheta) \\ M_{s,ba}(\vartheta) & L_{s,b}(\vartheta) & M_{s,bc}(\vartheta) \\ M_{s,ca}(\vartheta) & M_{s,cb}(\vartheta) & L_{s,c}(\vartheta) \end{bmatrix} \tag{1.70}$$

In case of linearity, the magnetic energy and coenergy are equal. The torque can be again written as in (1.23). It is worth highlighting that a significant difference can be found between the general doubly-fed machine and the SynRM when splitting the torque in its components. In Sec. 1.2.2 it has been shown that the torque of a doubly-fed three phase machine includes the reluctance, the electro-dynamic and the cogging torque. On the contrary, the torque produced by the SynRM has only one term, namely the reluctance torque, that can be expressed as

$$\tau(\mathbf{i}, \vartheta) = \underbrace{\frac{1}{2} p \mathbf{i}^t \left[\frac{d}{d\vartheta} \mathbf{L}(\vartheta) \right] \mathbf{i}}_{\tau_r} \tag{1.71}$$

The electrodynamic torque is produced by the variation of the mutual inductances between the stator and the rotor windings. This term is present not only in machines with a rotor winding but in permanent magnet machines as well. In this case, the torque is produced by the interaction of the magnet flux linkage with the stator windings. This component of torque is null in case of SynRM since the rotor has no permanent magnet neither windings.

The cogging torque is caused by the interaction between the rotor flux linkage and the stator anisotropies, mainly caused by slots opening. This term is present in both doubly-fed and permanent magnet machines. On the contrary, SynRM do not have this torque component.

The only component included in the torque expression (1.71) of the SynRM is the reluctance torque. The latter is related to the variation of the inductance matrix with the rotor position and it is present in every machine presenting an anisotropic rotor given by pole saliencies or flux barriers. It can be expressed as (1.25).

1.4.3. Machine with sinusoidally distributed windings

In AC machines, the stator winding is designed to enhance the fundamental component of the airgap flux distribution. Ideally, if the winding has a sinusoidal distribution around the airgap, the resulting flux linkage is sinusoidal with the rotor position. In this section, the equations of the SynRM are analyzed under the assumption of a sinusoidal distribution of the stator windings.

Under the assumption of distributed windings, the 3×3 inductance matrix of the three phase machine can be expressed as

$$\mathbf{L} = \frac{2}{3} \begin{bmatrix} L_\Sigma + L_\Delta \cos 2\vartheta & -\frac{L_\Sigma}{2} + L_\Delta \cos 2\vartheta_2 & -\frac{L_\Sigma}{2} + L_\Delta \cos 2\vartheta_1 \\ -\frac{L_\Sigma}{2} + L_\Delta \cos 2\vartheta_2 & L_\Sigma + L_\Delta \cos 2\vartheta_1 & -\frac{L_\Sigma}{2} + L_\Delta \cos 2\vartheta \\ -\frac{L_\Sigma}{2} + L_\Delta \cos 2\vartheta_1 & -\frac{L_\Sigma}{2} + L_\Delta \cos 2\vartheta & L_\Sigma + L_\Delta \cos 2\vartheta_2 \end{bmatrix} \tag{1.72}$$

where $\vartheta_1 = \vartheta - 2/3\pi$ and $\vartheta_2 = \vartheta - 4/3\pi$, $L_\Sigma = (L_d + L_q)/2$ and $L_\Delta = (L_d - L_q)/2$.

The current can be assumed by the general expression:

$$\begin{aligned} i_a &= I_M \cos(\vartheta + \frac{\pi}{2} - \gamma) \\ i_b &= I_M \cos(\vartheta_1 + \frac{\pi}{2} - \gamma) \\ i_c &= I_M \cos(\vartheta_2 + \frac{\pi}{2} - \gamma) \end{aligned} \tag{1.73}$$

The three phase flux linkages can be obtained starting from (1.72) and (1.73) as $\boldsymbol{\lambda} = \mathbf{L}\mathbf{i}$, obtaining

$$\begin{aligned} \lambda_a &= I_M[-L_\Sigma \sin(\vartheta - \gamma) + L_\Delta \sin(\vartheta + \gamma)] \\ \lambda_b &= I_M[-L_\Sigma \sin(\vartheta_1 - \gamma) + L_\Delta \sin(\vartheta_1 + \gamma)] \\ \lambda_c &= I_M[-L_\Sigma \sin(\vartheta_2 - \gamma) + L_\Delta \sin(\vartheta_2 + \gamma)] \end{aligned} \tag{1.74}$$

The result is consistent with the assumptions that the flux linkages can be described as a sinusoidal function.

The flux equation (1.74) can be similarly derived for the equivalent two phase machine. In particular, by applying the Clarke transformation to (1.72) it is possible to express the inductance matrix in the stationary reference frame, obtaining

$$\mathbf{L} = \begin{bmatrix} L_\Sigma + L_\Delta \cos 2\theta & L_\Delta \sin 2\theta \\ L_\Delta \sin 2\theta & L_\Sigma - L_\Delta \cos 2\theta \end{bmatrix} \tag{1.75}$$

The same transformation can be applied to (1.73), obtaining

$$\begin{aligned} i_\alpha &= -I_M \sin(\theta - \gamma) \\ i_\beta &= I_M \cos(\theta - \gamma) \end{aligned} \tag{1.76}$$

The flux linkage can be obtained starting from (1.75) and (1.76) as $\boldsymbol{\lambda} = \mathbf{L}\mathbf{i}$, obtaining

$$\begin{aligned} \lambda_\alpha &= I_M[-L_q \cos(\gamma) \sin(\theta) + L_d \sin(\gamma) \cos(\theta)] \\ \lambda_\beta &= I_M[L_q \cos(\gamma) \cos(\theta) + L_d \sin(\gamma) \sin(\theta)] \end{aligned} \tag{1.77}$$

Similarly, the equation of the two phase machine can be derived applying the Park tranformation, i.e. expressing the quantities in the reference frame rotating synchronously with the rotor.

The inductance matrix obtained with this transformation is

$$\mathbf{L}_{dq} = \begin{bmatrix} L_d & 0 \\ 0 & L_q \end{bmatrix} \tag{1.78}$$

In the dq reference frame, the currents can be expressed as

$$\begin{aligned} i_d &= I_M \sin(\gamma) \\ i_q &= I_M \cos(\gamma) \end{aligned} \tag{1.79}$$

Finally, repeating the same calculation done for the three phase system and for the two phase machine in the stationary reference frame, the flux linkage can be expressed as the product between (1.78) and (1.79)

$$\begin{aligned} \lambda_d &= I_M L_d \sin(\gamma) \\ \lambda_q &= I_M L_q \cos(\gamma) \end{aligned} \tag{1.80}$$

It is worth noticing that in this case, i.e. with a sinusoidal winding distribution at the airgap, the self inductances are constant and the mutual inductances $L_{dq} = L_{qd}$ are null. For this reason, starting from (1.57), the torque can be expressed as

$$\tau = p(\lambda_d i_q - \lambda_q i_d) \tag{1.81}$$

1.5. Conclusions

In this chapter the model of the synchronous reluctance machine has been developed. First, the equations have been derived considering the most general case of three phase electrical machine, i.e. the doubly fed three phase machine. This machine presents windings on both the stator and the rotor. It is worth highlighting that this model could represent the behaviour of every kind of synchronous machine, including permanent magnet and reluctance machines. The model has been developed with the only assumption of no hysteresis and no eddy currents. After that, the equations have been obtained introducing the hypothesis of linearity, i.e. neglecting iron saturation.

The three phase system has been transformed into a doubly fed two phase machine. The same considerations made for the three phase machine have been repeated, specifying the equation for the two phase system. Again, the model has been first developed with no restriction on the magnetic behaviour of the machine and later introducing the hypothesis of no iron saturation.

Finally, the results obtained for the doubly fed machines, both the three phase and the two phase, have been used to develop the model of the SynRM by imposing specific condition on the rotor currents. In particular, taking null rotor currents in the model of the doubly fed machine, it is possible to represent a synchronous reluctance machine. The equations have been developed considering the most general case, then introducing the hypothesis of linearity and finally considering a sinusoidal distribution of the windings.

Chapter 2

Predictive Current Control

Predictive current control schemes strongly rely on the knowledge of the plant model. The accuracy of the Model-based current prediction could be affected by parameters variation or mismatch, non idealities and other model inadequacies. In Synchronous Reluctance Machine this effect could be particularly critical since its inherent intense iron saturation causes the variation of the inductances in a wide range. Recently, Model-free prediction has been presented as an effective solution to overcome the model inadequacies. Control schemes based on this, do not require a model for the prediction since they rely on the stored current variations obtained by measurements. This innovative control techique guarantees robustness to parameter variations and mismatches. On the other hand, a frequent update of the stored current variations is mandatory to avoid the so called voltage vector stagnation that affects the performance leading to the loss of the control. In this chapter, Predictive Current Control schemes are analysed and presented focusing on both Model-based and Model-free prediction.

2.1. Introduction

Owing to its simplicity of comprehension and implementation, its improved dynamics and fast response, Predictive Control (PC) has been widely investigated and implemented. This kind of control is able to predict the future plant behaviour and uses this capability to select the control action. The choice of the latter is based on the evaluation of a cost function. In the fields of power electronics and electric drives, PC-based schemes have been often used to control the current flowing in the load, e.g. an electric motor, connected to the power converter [1]. This kind of schemes are referred as Predictive Current Control (PCC) and can be classified in two categories depending on how the switching signals for actuating the demanded voltages are generated. The first approach, named Convex Control Set (CCS), provides any voltage vector obtained with a combination (through a pulse width modulation stage) of two or three base vectors of the inverter. The second, called Finite Control Set (FCS), exploits the discrete nature of the power converter and does not require a modulator since it uses only the base vectors.

The prediction commonly relies on the plant model giving rise to Model-Based PCC

(MBPCC). Due to its nature, its performance largely depends on the accuracy of the model. The effect of parameter mismatch in the current prediction of FCS-MBPCC for a two level converter are deeply investigated in [2]. In this work it is shown that the prediction error depends not only on the uncertainty of the model parameters but also on the instantaneous values of load current and output voltage of the inverter. This effect is more severe in presence of inductance mismatches and in particular when the prediction model overestimates the real value. Considering an electric motor as the plant, the above mentioned situation could occur due to iron saturation and it could be particularly critical in a SynRM. The reason is that, due to the geometry and the wide range operation capability, the inductances are strongly dependent on the currents and they vary in a wide range introducing significant errors in the prediction. The latter, in turn, implies a deterioration of the drive performance.

The robustness of MBPCC has been addressed in different ways, such as by mean of disturbance state observer or online parameter estimation. In [3] and [4] an observer-based scheme is used to improve the performance of a PCC scheme for an induction machine. In the former a Luenberger observer is used to compensate for all the unknows dynamics, while the latter exploits a second order sliding mode observer. Both these works compare the performance with a traditional MBPCC scheme under the effect of parameter mismatch, showing the effectiveness of the observers. In [5] a robust predictive current control scheme for a Permanent Magnet Synchronous Machine (PMSM) is presented. In particular, the performance of a dead beat controller are improved against parameter variations by mean of an integral term. In [6], an adaptive MBPCC for PMSM is presented. Here the inductances are estimated online by mean of an adaptive observer and are used in the model prediction and in the current reference generation as well. Paper [7] analyses the effect of parameter variations in MBPCC for a PMSM and after that proposes an identification process based on least square minimization to ehnance the performance of the scheme.

An effective solution, referred as Model-Free PCC (MFPCC), to overcome the consequences of the model inadequacies has been proposed in [8] and then improved in [9]. In these works, the current variations relative to a certain voltage vector are recorded and stored in a Lookup Table (LUT). The current prediction is later obtained by accessing the LUT in the position related to the considered voltage vector. The results shown in [9] highlighted that a reliable current prediction can be achieved only if the LUT is frequently updated, i.e. avoiding the phenomenon called: voltage vectors stagnation. The simple anti-stagnation solution proposed in [9] consists in monitoring the age of the voltage vectors and, whether one of them overcomes a fixed threshold, applying it. Althought the ease of implementation, this solution has some significant drawbacks. Firstly, the proposed anti-stagnation method implies the application of non optimal vectors since they are not taken from the cost function minimization. Besides, the choice of the threshold is made on the base of empirical considerations, i.e. it could not be suitable for every working condition, and it represents a tradeoff between the reliability of the prediction and the compliance with the cost function minimization.

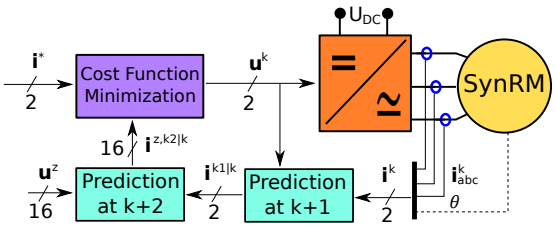

Figure 2.1: Predictive current control scheme

2.2. Predictive Current Control

A general representation of the PCC scheme is reported in Fig. 2.1. The idea behind PCC is to predict the future behaviour of the system and to choose the next control action according to a certain optimal criterion. In particular, in FCS-PCC, the choosen voltage vector is the one among the eight possible inverter states $\mathbf{u}^z = [u_d^z \; u_q^z]^t$ (with $z \in \mathcal{Q}$ and $\mathcal{Q} = \{0, \ldots, 7\}$) that minimize the cost function. The latter has to be carefully designed since the behaviour of the whole system is based on it. Different objective functions have been used in literature as will be analysed in Sec. 2.2.1. In this work, the considered cost function is

$$\min_{z \in \mathcal{Q}} \quad J = \left[i_d^* - i_d^{z,k2|k} \right]^2 + \left[i_q^* - i_q^{z,k2|k} \right]^2 \tag{2.1}$$

At each step, the current samples $\mathbf{i}^k = [i_d^k \; i_q^k]^t$ and the last voltage vector applied $\mathbf{u}^k = [u_d^k \; u_q^k]^t$ are used to predict the next values of current $\mathbf{i}^{k1|k} = [i_d^{k1|k} \; i_q^{k1|k}]^t$. The prediction at instant $k1 = k + 1$ can be generally expressed as

$$\begin{aligned} i_d^{k1|k} &= i_d^k + \Delta i_d^k \\ i_q^{k1|k} &= i_q^k + \Delta i_q^k \end{aligned} \implies \mathbf{i}^{k1|k} = \mathbf{i}^k + \boldsymbol{\Delta}\mathbf{i}^k \tag{2.2}$$

where $\boldsymbol{\Delta}\mathbf{i}^k = [\Delta i_d^k \; \Delta i_q^k]^t$ is the current variation between steps k and $k1$. The predicted currents $\mathbf{i}^{k1|k}$, together with the eight inverter states $\mathbf{u}^z$ (with $z \in \mathcal{Q}$), are used in turn to estimate the eight possible currents $\mathbf{i}^{z,k2|k} = [i_d^{z,k2|k} \; i_q^{z,k2|k}]^t$ at step $k2 = k + 2$. The latter are computed as

$$\begin{aligned} i_d^{z,k2|k} &= i_d^{k1} + \Delta i_d^{z,k1} \\ i_q^{z,k2|k} &= i_q^{k1} + \Delta i_q^{z,k1} \end{aligned} \implies \mathbf{i}^{z,k2|k} = \mathbf{i}^{k1} + \boldsymbol{\Delta}\mathbf{i}^{z,k1} \tag{2.3}$$

The values computed with (2.3) are used to evaluate the cost function (2.1) and to find the best voltage vector that will be applied at the next step. A two step prediction is required to compensate for the inherent delay in the digital implementation of the PCC scheme [10]. The significant difference between MBPCC and MFPCC stands in how the current variations $\boldsymbol{\Delta}\mathbf{i}^k$ and $\boldsymbol{\Delta}\mathbf{i}^{z,k1}$ in (2.2) and (2.3) are evaluated, as will be described in the next sections.

2.2.1. Cost function

The choice of the cost function represents a crucial aspect in the design of a control scheme. Different cost functions have been used in literature. In [8], a cost function based on the absolute error is employed in the *abc* three phase system for an Interior Permanent Magnet (IPM) machines. In [9], the same is employed in the $\alpha\beta$ stationary reference frame for a SynRM. The same is used in [11] for a Surface-mounted Permanent Magnet (SPM) machine. In [6] the cost function is based on the current squared error for an IPM machine. A detailed review of the proper choice of the cost function can be found in [12]. Here, different solutions are analysed and useful considerations are given on the weighting factors and the hard constraints (e.g. current limits included in the cost function).

In traditional Field Oriented Control (FOC) schemes, the dq currents are controlled by two indipendent regulators. This guarantees that (if no limitations are involved), both the references are precisely tracked even under dynamics according to the bandwidth of the two loops. PCC relies on the minimization of the only cost function that has to include both the current errors. Considering the SynRM application, the remarkable anisotropy could result in a too different behaviour in the two axes. In particular, an improper choice of the cost function could result in a biased control action giving the priority to one of two axes that could be particularly detrimental during the machine operation. Some considerations on this aspect are reported in this section.

The first cost function considered is the one based on the absolute error, that can be written as

$$\min_{z\in\mathcal{Q}} \quad J = |i_d^* - i_d^{z,k2|k}| + |i_q^* - i_q^{z,k2|k}| \tag{2.4}$$

Considering the ideal base point as the reference, the iso-level curves of this cost function are plotted in Fig. 2.2(b) with dashed lines.

In order to verify its suitability, the PCC based on (2.4) has ben tested in case of fast dynamics involving current steps. In particular, with the machine at standstill a speed step is given as a reference to the speed regulator. As a consequence, its output saturates to the maximum current amplitude, i.e. the ideal base point represents the current reference. The results of the simulation are reported in Fig. 2.2. In particular, the dq current waveforms, the torque and the voltage vector indexes are shown in Fig. 2.2(a). It is worth highlighting that, in the initial stage the regulator only acts to nullify the d-axis error. As can be seen, since at each step the voltage vector with index 4 is chosen (and $\vartheta = 0$),the d-axis current rapidly reaches the negative reference while the q-axis is still zero. A clear representation is given by the point of work trajectory in the dq plane (blue solid line in Fig. 2.2(b)). Once the direct current reaches the reference ($i_d^* = -1/\sqrt{2}$ [p.u.]), the predictive regulator starts choosing vectors able to increase the quadrature current, i.e. indexes 2 and 3. The control action is clearly twofold: (i) the current with the lower inductance is firstly pushed towards its reference and, only after, (ii) the error of the second current is minimized. A collateral effect is that the torque produced by the machine remains zero while one of the two current is null and this in turn implies a slower speed response.

The considerations made so far can be resumed as follows. Due to the significant rotor anisotropy, the control action presents a bias. In particular, the fastest way to reduce the current error is to shift the point of work first along the axis with the lower

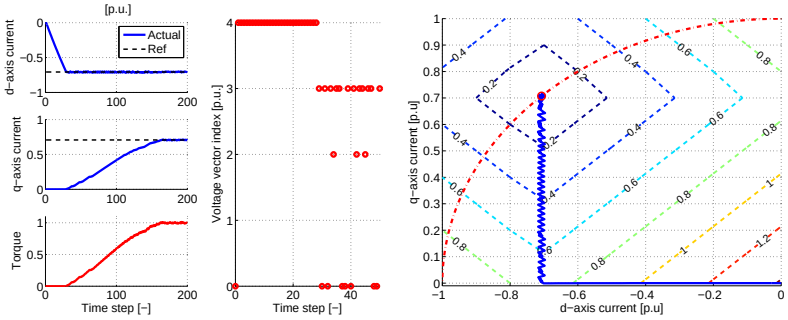

(a) Control quantities (b) dq current plane

Figure 2.2: Cost function based on absolute error

inductance. As a consequence, only one of the two currents rapidly reaches the reference. It is worth mentioning, that this undesired behaviour is obtained not only at the startup of the machine (as in the results of Fig. 2.2), but in all those operations involving big current errors. This effect is particularly evident when the d-axis is aligned with one of the six active voltage vectors of the inverter. In this situation, the predictive regulator chooses the aligned vector (or its opposite depending on the sign of the current) to fastly vary the d-axis current while keeping a constant quadrature current.

The first idea to overcome this undesired behaviour is to weight the two error components in the cost function. In particular, using an higher value for the q-axis would give more importance to its error avoiding that the current remains too distant from the reference. Since the bias is given by the anisotropy, a reasonable attempt is to weight the errors in the cost function with the saliency ratio obtaining

$$\min_{z\in\mathcal{Q}} \quad J = |i_d^* - i_d^{z,k2|k}| + \frac{L_q}{L_d}|i_q^* - i_q^{z,k2|k}| \tag{2.5}$$

The map of the latter is reported in Fig. 2.3(b) with dashed lines. The results of the PCC based on (2.5) are reported in Fig. 2.3. The behaviour obtained with the new cost function is completely different. It can be seen that, in the initial stage the predictive controller outputs the voltage vector with index 3. The latter pushes both the currents towards their reference avoiding the effect obtained using (2.4). As clearly shown in Fig. 2.3(b), althought the direct current is necessarily faster, the point of work does not move along the d-axis. As expected, the torque response is faster, i.e. it starts raising from the first step.

Another cost function is based on the squared error and it can be written as

$$\min_{z\in\mathcal{Q}} \quad J = \left[i_d^* - i_d^{z,k2|k}\right]^2 + \left[i_q^* - i_q^{z,k2|k}\right]^2 \tag{2.6}$$

Fig. 2.4(b) reports the iso-curves of the considered cost function.This choice should avoid that the point of work gets too far from the reference. Since the errors are squared in the cost function, as soon as one of the two currents move from its reference, its term becomes much bigger than the other one forcing the cost function to reduce it. This

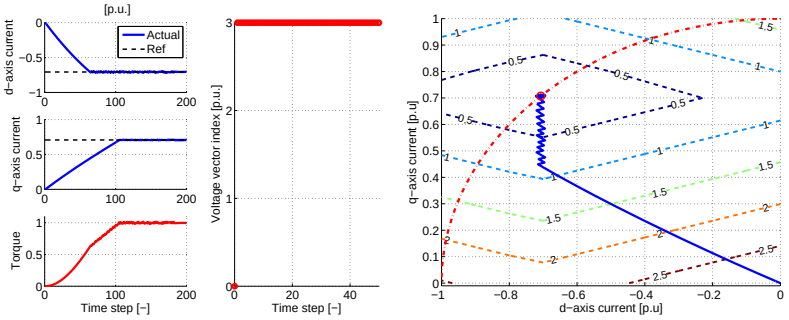

(a) Control quantities (b) dq current plane

Figure 2.3: Cost function based on weighted absolute error

cost function can be rewritten as

$$\begin{aligned} \min_{z\in\mathcal{Q}} \quad J &= \left[i_d^* - i_d^{z,k2|k}\right]\cdot\left[i_d^* - i_d^{z,k2|k}\right] + \left[i_q^* - i_q^{z,k2|k}\right]\cdot\left[i_q^* - i_q^{z,k2|k}\right] \\ &= w_d(\varepsilon_d)\cdot\underbrace{\left[i_d^* - i_d^{z,k2|k}\right]}_{\varepsilon_d} + w_q(\varepsilon_q)\cdot\underbrace{\left[i_q^* - i_q^{z,k2|k}\right]}_{\varepsilon_q} \end{aligned} \tag{2.7}$$

and it can be seen as a weighted sum of the current errors with variable weights $w_d(\varepsilon_d)$ and $w_q(\varepsilon_q)$ depending on the errors ε_d,ε_q themselves (the weights are thus equal to the errors).

The results obtained with (2.6) are reported in Fig. 2.4. As for the cost function with the absolute error, the first steps are commited to reduce the d-axis error. To do this, the predictive regulator chooses the voltage vector with index 4, that allows the fastest decrease of i_d while keeping the quadrature current at zero. The comparison with Fig. 2.2 shows that this operation lasts for a lower number of steps using the squared error. The reason is that, as soon as the error of the d-axis becomes lower than a certain threshold, the q-axis error results the dominant component in the cost function. As a consequence, after the short initial stage, the choosen voltage vector is the one with index 3. With the cost function (2.6) is therefore possible to shorten the biased control action (with null q-axis current and torque).

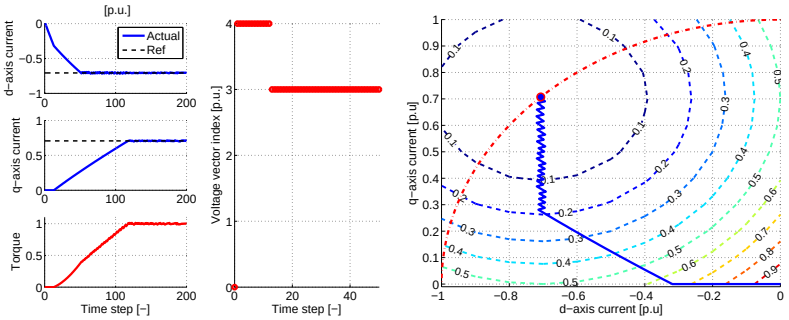

(a) Control quantities (b) dq current plane

Figure 2.4: Cost function based on squared error

The last cost function evaluated in this section is obtained combining the beneficial

effects of using the saliency ratio as a weight and the squared error. The resulting cost function is

$$\min_{z\in\mathcal{Q}} \quad J = \left[i_d^* - i_d^{z,k2|k}\right]^2 + \frac{L_q}{L_d}\left[i_q^* - i_q^{z,k2|k}\right]^2 \tag{2.8}$$

Fig. 2.5 shows the results obtained with (2.8). It can be seen that the performance are improved with respect to those of Fig. 2.4 and are the same of Fig. 2.3.

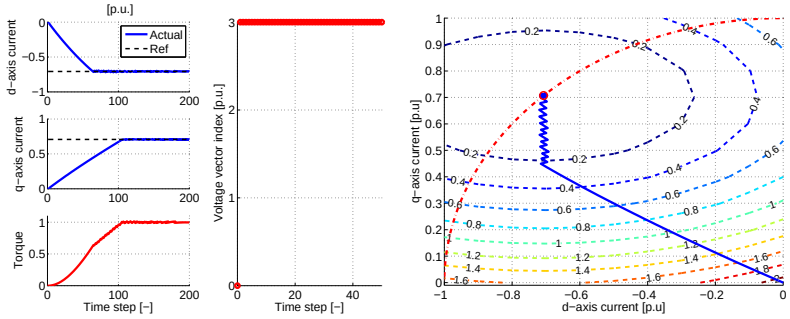

(a) Control quantities (b) dq current plane

Figure 2.5: Cost function based on weighted squared error

The results and the considerations presented in this section highlighted that a certain cost function could not be suitable for every operation of the SynRM. In particular, the rotor anisotropy could introduce a bias in the control action that in turn could affect the performance during dynamics. It is worth mentioning that all the considered cost functions exhibit comparable steady state performance.

The choice of introducing the saliency ratio as a weight in the cost function showed balanced performance. In particular, under strict dynamics in both axes, the voltage vector that pushes both the current towards their reference is chosen. The main drawback of this tecnique is that the knowledge of the saliency ratio is required, i.e. the inductances have to be precisely known. Besides, due to the significant iron saturation, their values are not constant but depend on the currents. For this reason, a perfect compensation would require the precise magnetic characterization of the machine in every working condition and, based on this, variable weights should be used.

In this part of the work, the cost function based on the squared error (2.6) has been considered. The dynamic test showed that it allows sufficiently good performance. Furthermore, it does not require the knowledge of the machine parameters. This guarantees robustness againts parameter uncertainty and variations and, considering the purpose of this part of the work, it represents the most suitable choice.

2.2.2. Model-Based PCC

Neglecting the effect of cross saturation and considering a sinusoidal distribution of the stator windings (see Chapter 1), the equivalent model of the SynRM can be expressed in the synchronous rotating reference frame as

$$\begin{aligned} \boldsymbol{\Delta}\mathbf{i}^k &= \mathbf{A}\mathbf{i}^k + \mathbf{B}\mathbf{u}^k \\ \mathbf{A} &= \begin{bmatrix} -R/\ell_d \cdot T_s & \omega L_q/\ell_d \cdot T_s \\ -\omega L_d/\ell_q \cdot T_s & -R/\ell_q \cdot T_s \end{bmatrix} \\ \mathbf{B} &= \begin{bmatrix} T_s/\ell_d & 0 \\ 0 & T_s/\ell_q \end{bmatrix} \end{aligned} \tag{2.9}$$

where, R stands for the stator winding resistance, $L_d(i_d^k)$ and $L_q(i_q^k)$ represent the apparent inductances, $\ell_d(i_d^k)$ and $\ell_q(i_q^k)$ are the differential inductances and ω is the electrical speed. For compactness, the current dependencies are omitted in (2.9).

Starting from the current samples at instant k, a viable model based prediction of the currents at the next step can be obtained considering an ideal SynRM model, in which the inductances are constant and $\ell_d = L_d$ and $\ell_q = L_q$. This allows obtaining the expression of the current variations $\boldsymbol{\Delta}\mathbf{i}^k$ between two consecutive samples as

$$\begin{aligned} \boldsymbol{\Delta}\mathbf{i}^k &= \mathbf{A}_m\mathbf{i}^k + \mathbf{B}_m\mathbf{u}^k \\ \mathbf{A}_m &= \begin{bmatrix} -R/L_d \cdot T_s & \omega L_q/L_d \cdot T_s \\ -\omega L_d/L_q \cdot T_s & -R/L_q \cdot T_s \end{bmatrix} \\ \mathbf{B}_m &= \begin{bmatrix} T_s/L_d & 0 \\ 0 & T_s/L_q \end{bmatrix} \end{aligned} \tag{2.10}$$

This linearized model is often used in literature to predict the current of synchronous machines. It is worth mentioning that the hypothesys of no iron saturation is more suitable for SPM machines where the effect of iron saturation is less significant than in IPM or SynRM.

Once the currents $\mathbf{i}^{k1|k}$ are obtained with (2.2), they are used to evaluate all the possible next current variations $\boldsymbol{\Delta}\mathbf{i}^{z,k1}$ (with $z \in \mathcal{Q}$) as

$$\boldsymbol{\Delta}\mathbf{i}^{z,k1} = \mathbf{A}_m\mathbf{i}^{k1|k} + \mathbf{B}_m\mathbf{u}^z \tag{2.11}$$

which in turn allows predicting the currents $\mathbf{i}^{z,k2|k}$ with (2.3). The latter are used in the evaluation of the cost function (2.1).

During the different machine operations, a mismatch betweeen the real and the expected parameters as well as between differential and apparent inductances could occur. Besides, SynRM presents magnetic characteristics that are strongly non linear, making the model used for the predictions (2.10) and (2.11) unsuitable.

2.2.3. Effect of parameter mismatch and variation

In this section, the effects given by parameter mismatch and variation are briefly investigated. Due to the nonlinear nature of MPC, it is not possible to analyse its behavior in terms of stability with traditional methods used for linear control schemes, e.g. the root locus and the closed loop analysis. Hence, the consequences of model parameter mismatch has been empirically evaluated by analysing the performance of the MBPCC under different affecting uncertainties. These studies have been carried out in applications involving current prediction and control with three-phase two-level inverters [12, 13], multiphase drives [14] and active front end applications [15]. Some of the above cited works concluded that the uncertainty in the load resistance has a less relevant or negligible influence on the MBPCC operation. In other works, the influence of resistance and inductance mismatch has been studied separately, identifying two different behaviour: resistance variations are responsible for steady-state errors while uncertainties on the value of the inductance are related to error in both steady-state and dynamics predicted currents. A mathematical analysis on the effect of parameter mismatch in the current prediction is investigated in [2]. The prediction error is demonstrated to be more severe when the actual inductance is lower than the expectations, i.e. with an overestimated modeled inductance. Besides, the drive performance are worsened by an increased ripple in the controlled currents.

The work presented in [2] considers a resistance and inductance mismatch between the values used for the prediction and the actual one in case of an RL load. Some considerations have to be done to extend the results obtained in [2] to the case of SynRM. In particular, this kind of machines exhibits an inherent significant iron saturation that can be identified as the main responsible for model inaccuracies. Whether iron saturation occurs, the effect is not only a variation in the inductance values but the machine model itself is different. Precisely, the exact model of the saturated machine (neglecting cross saturation) is the one reported in (2.9) while in case of iron linearity the exact model is (2.10).

It is worth evaluating the prediction error in case a linear model is used for the current prediction to control a saturated SynRM. This method is often used for its ease of implementation and because it does not require the precise magnetic characterization of the machine. The error can be computed as the difference of (2.9) and (2.10), obtaining

$$\begin{aligned} \boldsymbol{\varepsilon} &= \boldsymbol{\Delta A}\ \mathbf{i}^k + \boldsymbol{\Delta B}\mathbf{u}^k \\ \boldsymbol{\Delta A} = \mathbf{A} - \mathbf{A}_m &= \begin{bmatrix} R\left(\frac{\ell_d - \tilde{L}_d}{\ell_d \tilde{L}_d}\right) & \omega_{me}\left(\frac{\tilde{L}_d L_q - \tilde{L}_q \ell_d}{\ell_d \tilde{L}_d}\right) \\ \omega_{me}\left(\frac{\tilde{L}_d \ell_q - L_d \tilde{L}_q}{\ell_q \tilde{L}_q}\right) & R\left(\frac{\ell_q - \tilde{L}_q}{\ell_q \tilde{L}_q}\right) \end{bmatrix} T_s \\ \boldsymbol{\Delta B} = \mathbf{B} - \mathbf{B}_m &= \begin{bmatrix} \left(\frac{\tilde{L}_d - \ell_d}{\ell_d \tilde{L}_d}\right) & 0 \\ 0 & \left(\frac{\tilde{L}_q - \ell_q}{\ell_q \tilde{L}_q}\right) \end{bmatrix} T_s \end{aligned} \tag{2.12}$$

where ℓ and L stand for the actual differential and apparent inductance while $\tilde{L}$ is used for the expected value of the apparent inductance used in the linear model for the current prediction. The error expressed in (2.12) includes both the component given by the difference between the linear and the saturated model ($\ell \neq L$), and the compontent

given by the apparent inductance mismatch ($\tilde{L} \neq L$). The results obtained in [2] are still valid in case of SynRM considering a small variation analysis. In particular, the considerationss made in [2] can be extended, linearizing the model about a working point, i.e. considering a linear machine with inductance equal to the differential inductances in the considered operating point.

The effects of iron saturation are verified in Fig. 2.6 where the performance of an ideal and a saturated machine are shown. In both cases, the linearised model (2.10) is used to predict the currents. The test is performed with locked rotor and providing two current steps. The expected increased ripple is evident in Fig. 2.6(b).

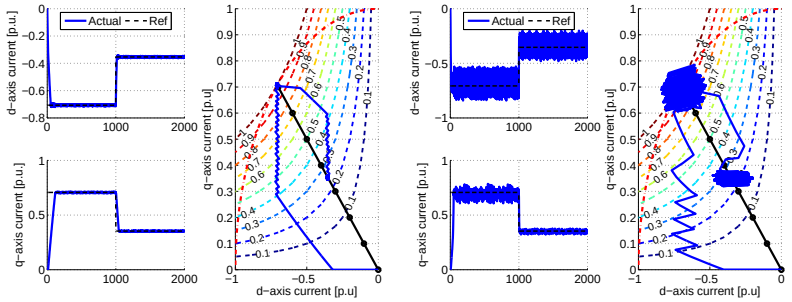

(a) Ideal machine (b) Saturated machine

Figure 2.6: Comparison between linear and saturated machine

It is clear from Fig. 2.6 that using a linearised model to control a saturated machine implies having a distorted current waveform. The reason is that since the expected behaviour is totally different from the actual one, the predictive regulator does not work properly. As a consequence, the voltage vectors chosen by the cost function minimization are different from the ideal case. Fig. 2.7 shows a detail of the current prediction accuracy and the voltage vector selection. As can be seen, the prediction (blue line with squared markers) is precise and reliable in case of ideal machine. On the other hand, it is clear that the prediction with the saturated machine is not precise. In particular, the current variations are always underestimated. As a consequence, the voltage vector selection is different in the two cases. In the considered example, with the ideal machine, the predictive regulator chooses indexes 3 and 5 to reduce (more negative values) the direct current. The former allows an increase while the latter a decrease of the q-axis current. The null state (index 0) is used to increase (more positive values) the d-axis while slowly reducing the quadrature current. Considering the saturated machine, two opposite vectors 1 and 4 are used to increase and reduce the direct current respectively while reducing the quadrature current. Vectors 2 and 3 allows increasing the q-axis value.

As shown in Fig. 2.7 the sequence of voltage vectors is completely different in the two cases. This implies a different number of switching. Fig. 2.8 shows the number of switching at each step and the total number. It can be seen that the switching pattern with the ideal machine involve only one leg. On the contrary, in case of saturated machine, at each step 1,2 or 3 legs can be involved. As a consequence, the total number of commutations is higher in the case of saturated machine. It is worth mentioning that the latter consideration is not general, i.e. it is not sure that using the nominal model in

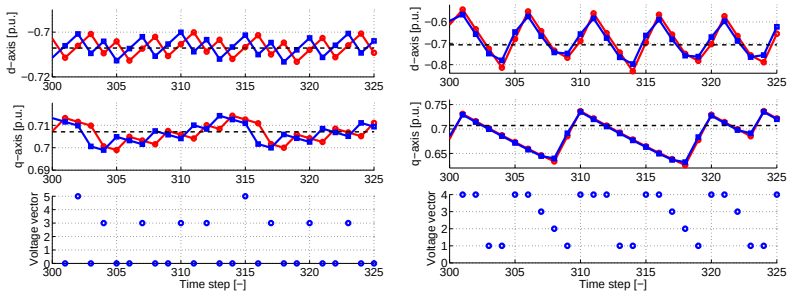

(a) Ideal machine (b) Saturated machine

Figure 2.7: Comparison between linear and saturated machine

the prediction while controlling a saturated machine does not imply an higher number of commutations. In general, the switching pattern obtained with an exact model and with an imprecise one is different. After that, the total number of commutations depends on the kind of operation, on the cost function (that could include a term to penalize the number of switchings) and other factors.

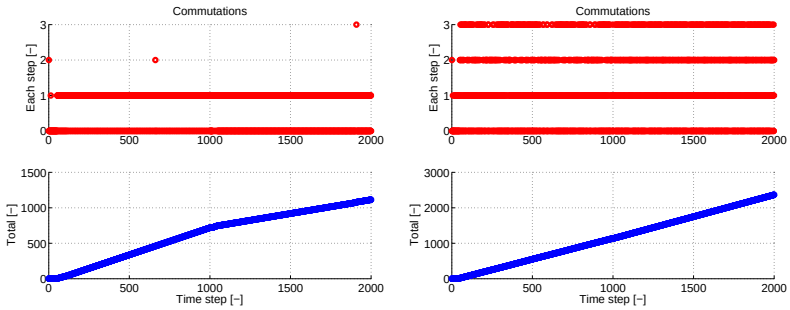

(a) Ideal machine (b) Saturated machine

Figure 2.8: Comparison between linear and saturated machine

2.2.4. Model-Free PCC

The concept of MFPCC has been first presented in [8] and then improved in [9]. The aim of this control scheme is to relieve the knowledge of parameters required by MBPCC and to improve the performance of current tracking even under the effect of strong iron saturation and, of course, under the effects of other phenomena affecting the prediction.

The basic idea of MFPCC can be described as follows. After a voltage vector is output from the cost function minimization, the resulting current variations in the two axes are recorded and stored in two different LUTs as represented in Fig. 2.9(a). In this way, eight values of Δi_d^z and eight values of Δi_q^z are linked to the corresponding inverter state $\mathbf{u}^z$ with $z \in \mathcal{Q}$. The current predictions (2.2) and (2.3) are easily obtained by accessing the values stored in the LUTs corresponding to the considered voltage vector (see Fig. 2.9(b)). Since the values of $\mathbf{\Delta i}^z$ are obtained from measurements, they

inherently contain the information about the real behaviour of the machine in conditions near to the actual ones.

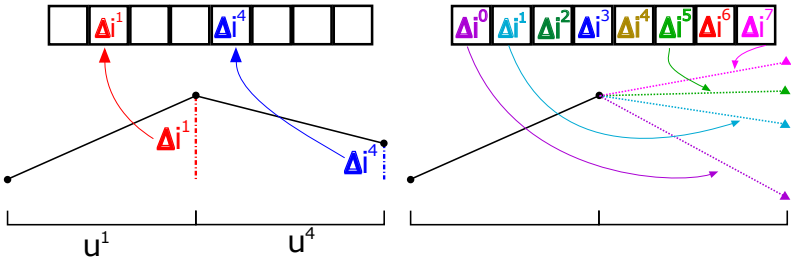

(a) Storing current vatiation (b) Model-free prediction

Figure 2.9: Representation of the Model-free prediction

Although the basic principle is the same, a different implementation is used in [8] and in [9]. The former is represented in Fig. 2.10. During each samplig time, two current measurement are performed. In order to obtain the correct difference signal and to avoid the current spikes given by the switches, the first current detection is finished before the (k)th switching state is performed while the second detection is delayed by a fixed time period after the (k)th switching is performed. As can be seen in Fig. 2.10(b), the starting point of the switching interval is lagging behind that of the corresponding sampling interval by a fixed amount of time. As a consequence, the stator current at the end of the (k)th switching interval will be measured in the (k + 1)th sampling interval. As a result, the current difference corresponding to the (k)th switching interval cannot be calculated in the (k)th sampling interval. In other words, the current difference corresponding to the previous switching state can be calculated in the present sampling interval.

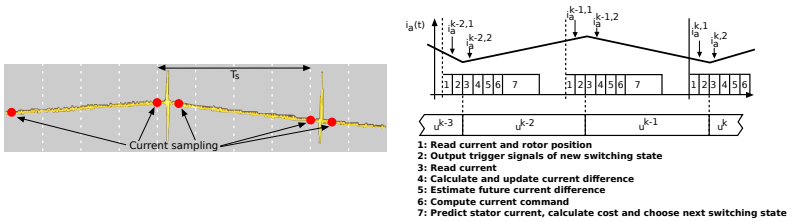

(a) Current difference detection technique (b) Scheme operations

Figure 2.10: MFPCC current variation detection and operation used in [8]

The current detection technique represented in Fig. 2.10 requires two samples at each interval. To avoid the detection of spikes, the second currrent measurement is delayed of a fixed interval of time after the new conducting mode is applied. However, since there are no general guidelines regarding the choice of the time delay, it largely depends on empirical experience and the inverter characteristics. A improper choice of the latter could result in permanent damages to the drive system. To finally resolve this issue, a single current detection method has been used in [9]. In each sampling period, the current detection is performed immediately before a conducting mode is applied, as

shown in Fig. 2.11.

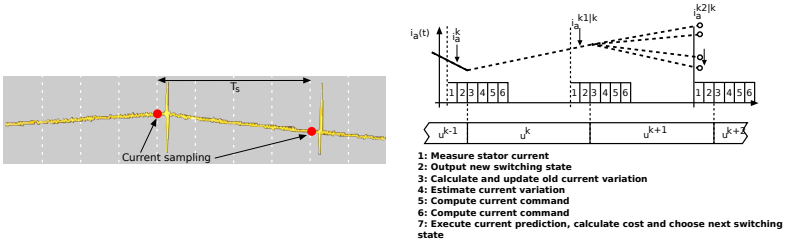

(a) Current difference detection technique

(b) Scheme operations

Figure 2.11: MFPCC current variation detection and operation used in [9]

Whether an inverter state is not used for several sampling intervals, the relative current variations are not updated for a long time. In [9], the authors refer to this issue as the stagnation of current variation update and they propose a simple solution to address it. In particular, if a voltage vector has not been applied for a number N_{old} of consecutive steps, this vector will be forced at the next interval. In this way, the output of the cost function minimization is discarded, feeding the machine with a non-optimal voltage vector. Some considerations on this aspect will be given later in this section.

The effectiveness of the model-free prediction is clearly shown in Fig. 2.12, where MBPCC and the MFPCC proposed in [9] are compared considering the saturated model on the SynRM. The results are obtained with a threshold $N_{old} = 200$. The plots show the results obtained with a speed step test with a reference of 100 [rpm] starting from standstill. As already described (see Fig. 2.6(b)), the MBPCC presents an increased current ripple due to the model inadequacy. On the contrary, since the MFPCC exploits the current measurements, i.e. the information on the model are obtained from the actual machine, it exhibits a better reference tracking and a low ripple, as in the case of non saturated machine. The same considerations can be made on the switching, i.e. the model-free prediction presents a different switching pattern that, in this test, allows achieving a lower number of commutations as shown in Fig. 2.12(b).

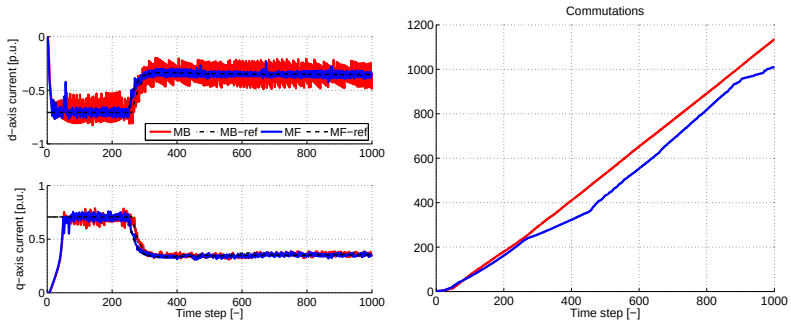

(a) Current waveforms

(b) Switching

Figure 2.12: Comparison between MBPCC and MFPCC with $N_{old} = 200$

As can be seen in Fig. 2.12(a), the current waveforms of the MFPCC present some evident spikes. These are given by the simple anti-stagnation solution proposed in [9].

Fig. 2.13(a) and Fig. 2.13(b) report the current waveforms obtained with $N_{old} = 100$ and $N_{old} = 50$ respectively.

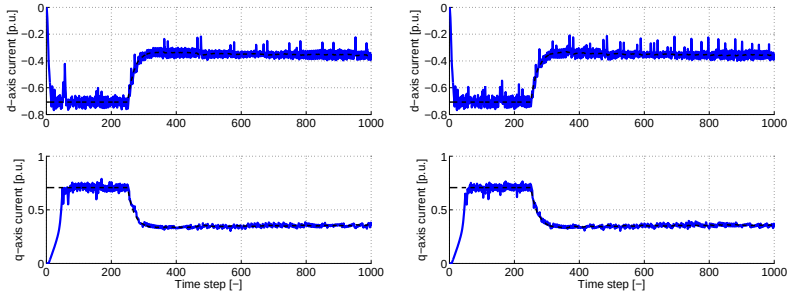

(a) $N_{old} = 100$ (b) $N_{old} = 50$

Figure 2.13: Test with different values of the threshold N_{old}

Introducing non-optimal voltage vectors allows avoiding the voltage vector stagnation but at the same time causes spikes in the current waveform. The amplitude of this spikes depends on several aspects, e.g. the rotor position and the values of inductance. For the sake of clarity, the results obtained with $N_{old} = 50$ are analysed in detail. In particular, a time interval of 100 steps is considered in Fig. 2.14. The position of the dq-axis at the beginning of this interval is shown in Fig. 2.15. During the normal opration, the predictive regulator outputs the results of the cost function minimization. Precisely, considering the rotor position, the three optimal vectors:

- index 4: allows a small reduction of the direct current and increases the q-axis current;
- index 6: decreases the d-axis current while obtaining a negative variation of the quadrature current;
- index 0: it is chosen to obtain small variations towards the origin of both the currents (used when the point of work is close to the reference).

The latter and the relative current variations are pointed with red color in Fig. 2.14(a), in the second plot of Fig. 2.14(b) and in Fig. 2.15. In addition to the cost function minimization, the algorithm introduces different indexes to guarantee a frequent LUT update. The first plot of Fig. 2.14(b) shows the age of the eight vectors. Each time a vector is found to be old, i.e. when it has not been applied for 50 consecutive steps, the algorithm applies it. It can be seen that in this case, the stagnat vectors are 1, 2 and 3 (drawn with black color). After the application of one of these three non optimal vectors, another non-optimal vector is applied to bring the currents back to the reference. This vector (index 5 in this example with blue color) is not forced by the anti-stagnation algorithm since it does not reach the threshold N_{old}, but it is chosen by the cost function to bring the point of work back to the reference. In other words, this voltage vector represents an optimal choice in the modified situation after the application of old vectors, but it is not taken as optimal during the normal operation. This example shows that, during the steady state operation, the anti-stagnation method proposed in [9] forces

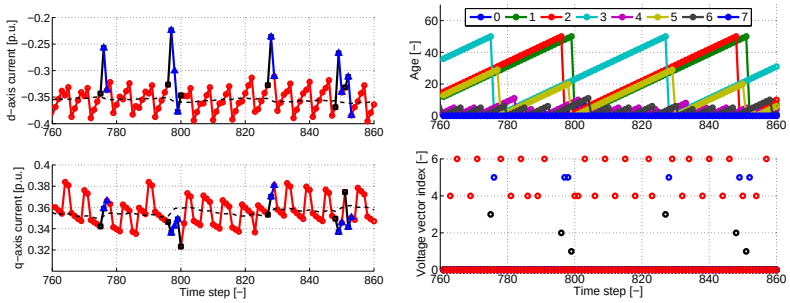

(a) Current waveforms (b) Age and voltage vector index

Figure 2.14: Detail of the MFPCC operation

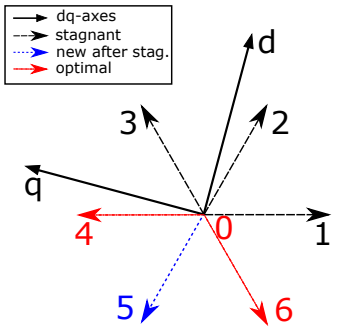

Figure 2.15: Detail of the MFPCC operation

voltage vectors that are not chosen by the cost function minimization and that could be even in opposition with the optimal vectors.

The choice of N_{old} is based on empirical considerations and it represents a trade off between the compliance with the cost function minimization and the LUT updating frequency, which is directly linked with the prediction accuracy and in turn with the stability of the control scheme. The lower the threshold, the more frequent the update and the higher the number of non optimal vectors applications. The higher the threshold, the higher the accordance with the cost function output but the lower the prediction accuracy. This considerations are qualitatively reported in the plot of Fig. 2.16

Resuming the considerations and the results shown so far it it possible to highlight that the anti-stagnation solution proposed in [9] has a main drawback, i.e. the application of non optimal voltage vectors. Indeed, every time that an inverter state is found to be old, the algorithm applies it, discarding the output of the cost function minimization. Besides, the choice of N_{old} represents a trade off between the quality of the prediction and the compliance with the cost function minimization. In other words, a small value of N_{old} implies a frequent table update and largely avoids stagnation while oftenly applying a big number of non optimal voltages. On the other hand, choosing a bigger value of N_{old} allows preserving the optimal control but the current prediction could be severely worsened. Finally, N_{old} is found based on empirical observations and its value could not guarantee the stability at every working condition.

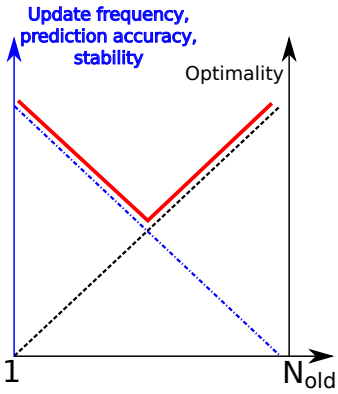

Figure 2.16: Qualitative representation of the choice of N_{old}

2.3. Conclusion

In this section the general Predictive Current Control is described and analysed. Some considerations about the choice of the proper cost function in case of salient machines have been provided. In particular, the effect given by the rotor anisotropy have been analysed during transient operations involving current steps, e.g. the machine startup. It has been shown that the cost function based on the absolute error could result in a biased behaviour, giving the priority to the axis with the lower inductance. The result is that during the first steps, while the current on the axis with the lower inductance fastly reaches its reference, the other one remains zero. A collateral effect is that the torque in null during this interval, resulting in a slower speed response. It has been shown that introducing a weighting factor equal to the saliency ratio allows overcoming this behaviour. With this solution, the bias is compensated and the error on the two axes are reduced in a balanced way. The main drawback of this solution is that it requires the knowledge of the saliency ratio, i.e. the values of the inductance. In SynRM, these values are strongly dependent on the current due to iron saturation. For this reason, using a constant weighting factor considering the nominal apparent inductances could not be a suitable compensation during all the machine operations. The results obtained with the cost function based on the squared error have showed a sufficiently balanced behaviour on both axes. Besides, it does not require the knowledge of the machine inductances. For this reasons, this cost function has been chosen for this part of the work.

The operation of the predictive regulator has been described considering the two steps prediction required to compensate for the delays introduced by the digital implementation. After that, both the Model-based and the Model-free prediction have been presented. In the former case, the effect of parameter mismatch and variation have been investigated. In particular, in SynRM applications, iron saturation has been recognised as the main responsible for model inadequacies.

Chapter 3

Avoiding stagnation in Model-free Predictive Current Control

Due to its nature, Model-free prediction is inherently robust to parameter variations. Since the current variations used for the prediction are directly obtained from measurements, the predictive regulator precisely knows the actual model. A crucial aspect for the proper operation of the drive, is the LUT update. In particular, a precise prediction requires that the latter is performed frequently, otherwise the values stored in the LUT are not reliable anymore and they could lead to a severe worsening of the drive performance and, in the worst case, the loss of control. Whether a voltage vector is not applied for several intervals, the relative current variation is not updated and the prediction based on this value is extremely different from the actual behaviour. This phenomenon is referred as stagnation of the voltage vector. In this chapter, an analysis of the effects of the voltage vector stagnation is provided. After that a novel anti stagnation method is proposed and tested.

3.1. Introduction

MFPCC has been developed in [8] and [9] and implemented for the current control of an IPM and a SynRM respectively. These works show the great advantages given by the Model-free prediction and the consequent enhanced performance of the drive. The results demontrated the feasibility and the effectiveness of this kind of control, showing that MFPCC is a promising technology although recent. Thanks to its inherent robustness to parameter variations, its spread could produce great benefits in industrial applications. First of all, the field of applicability of predictive control could be greatly extended since it is currently limited by the demanding need of the precise knowledge of the model. Without it, traditional predictive schemes lose their effectiveness and become unsuitable, making other well-established methods, e.g. linear control, the first choice in industry and in particular in drives applications. Furthermore, the absence of any requirements on the knowledge of the machine parameters has several outstanding effects. It results in an ease of implementation since it only requires current measurements and it avoids complex and time consuming computations. The design

is even effortless: no tricky tuning of gains and thresholds as other traditional control schemes, e.g. proportional-integral regulators, observers and estimators etc.. . This in turn represents an even more attractive feature: the possibility to be used in the development of an universal drive, i.e. machines with completely different characteristics could be controlled without changing the control algorithm and without laborious self-commissioning or identification procedures.

Despite the great potentialities, after MFPCC has been presented in [8], only one another work, proposed by the same authors, has been published on the same topic. Surely, further research is needed to develop this kind of control and to make it competitive.

The first crucial aspect that has to be addressed is the so called voltage vector stagnation. This phenomenon occurs when a value of current variation is not updated for several steps, i.e. the relative voltage vector is not applied in that time interval. Since the current response under a certain inverter output dramatically changes (in both sign and amplitude) with the machine state, an infrequent update of the LUT causes completely wrong predictions that drive the machine in unexpected operations. If stagnation is not prevented or readily solved, the performance are gradually worsened and end up with the total loss of control.

While this significant issue has not been mentioned in [8], it has been addressed with a simple solution in [9]. As already described in Chapter 2, this method presents some evident drawbacks: it forces non optimal vectors and it requires the tuning of a threshold that is made with empirical considerations and that could not be suitable for every operation

In this chapter a novel anti-stagnation solution is presented. It exploits the relationship between the current variations given by the eight inverter states. Based on this, it uses the three most recent values stored in the LUT to reconstruct the other four (the two null vectors cause the same current variation), achieving a continuous update.

3.2. Analysis of stagnation effects

The MFPCC schemes presented in [8] and [9] rely on the current variations stored in the LUT. In particular, every time that a voltage vector is applied, the relative current variation is updated. As explained in the next sections, the current variation given by a certain voltage vector depends on the machine state, i.e. on the current level, on the position and on the speed. In particular, both its amplitude and sign depend on the latter. This means that, every time a voltage vector is not chosen by the cost function for a number of steps, the relative current variation is not update in the considered time interval. In this case, the values contained in the LUT could be significantly different from the actual ones. Clearly, the longer the time interval in which the update is not performed the bigger the error between the LUT and the actual response of the machine. The negative effects given by these errors on the control, depend on the machine operation.

For the sake of clarity, an example of the effects of stagnation is provided in Fig. 3.1. The simulation is carried out providing a speed step. At the startup, the prediction is based on the nominal model and after 25 steps the model-free prediction is started.

The model-based startup allows filling the LUT with correct values of current variation. After that the MFPCC is able to track the current and the speed references but before step $k = 2000$ the control is lost, i.e. the current errors start increasing and the speed gradually reaches zero. The first plot of Fig. 3.1(b) shows that, after instant $k = 1000$ the predictive regulator start choosing only indexes 0, 5 and 6. This means that only the three relative current variations are updated in the LUT, while the other are remains constant and equal to the last update. At the end, only index 0 and 6 are ouput from the cost function minimization and the control is not able to regain the references. The reason can be found considering the values of the current variations in the two LUT plotted in Fig. 3.1(b). It can be seen that after a certain instant, in both the LUT, the most of the current variations have the same sign. In particular, in the LUT of the direct axis, all the values are positive but the one related to index 6. Similarly, in the q-axis, all the stored values are positive but indexes 0 and 1. For this reason, the predictive regulator uses the values stored in the LUT to evaluate the cost function and to reduce the current errors with no avail. In particular, it chooses index 6 to produce a negative variation of the direct current and 0 to produce a negative variation on the q-axis. All the other wrong values stored in the LUT, falsify the cost function evaluation, making impossible for the predictive regulator to choose a different index.

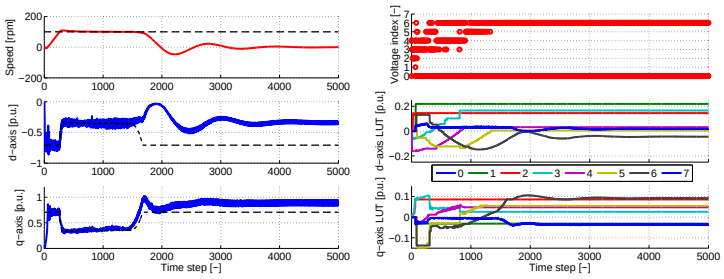

(a) Speed and currents (b) Voltage vector index

Figure 3.1: Example of the stagation effects

The example provided in this section allowed to give a qualitative explanation of the phenomenon of stagnation. It has been shown the behaviour of the predictive regulator in presence of stagnant vector, i.e. when the values stored in the LUT are not reliable. It has been verified that if the current variations are not readily updated the cost function evaluation is misrepresented leading to a wrong choice of the optimal voltage vector. Once the algorithm enters this condition, it could be impossible for him to regain the control of the machine.

A general analysis on the phenomenon of stagnation is not possible since its effects depend on a multitude of different aspects such as the kind of test, the cost function etc .. .

3.3. Proposed anti-stagnation method

The proposed updating method is described in this section. The aim is to find the relationship between the current variations given by the eight inverter states and to exploit it for the LUT update. In this way it would be possible to use the most recent values stored in the table to reconstruct the others. This method is expected to provide a continuous LUT update, which in turn means having a precise and reliable current prediction, without forcing non optimal voltage vectors.

Considering the discrete model of the SynRM (2.9), the current variation in the dq reference frame caused by the z-th voltage vector can be expressed as

$$\boldsymbol{\Delta}\mathbf{i}^{z,k} = \boldsymbol{\delta}\mathbf{i}^{\emptyset} + \boldsymbol{\delta}\mathbf{i}^{z} \tag{3.1}$$

where the total current variation $\boldsymbol{\Delta}\mathbf{i}^{z,k}$ is expressed as the sum of two different vectors, namely $\boldsymbol{\delta}\mathbf{i}^{\emptyset} = [\delta i_d^{\emptyset}\ \delta i_q^{\emptyset}]$ and $\boldsymbol{\delta}\mathbf{i}^{z} = [\delta i_d^{z}\ \delta i_q^{z}]$. The latter can be expressed as

$$\begin{aligned} \boldsymbol{\delta}\mathbf{i}^{\emptyset} &= \mathbf{A}\mathbf{i}^{k} \\ \boldsymbol{\delta}\mathbf{i}^{z} &= \mathbf{B}\mathbf{u}^{z} \text{ with } z \in \mathcal{Q} \end{aligned} \tag{3.2}$$

where the former represents the current variation caused by the null state of the inverter $\mathbf{u}^{\emptyset} = \mathbf{u}^{z} = [0\ 0]$ with $z = 0, 7$. In other words, this is the evolution of the system with null input voltage, i.e. the natural response. The second term $\boldsymbol{\delta}\mathbf{i}^{z}$ is given by the active voltage vector $\mathbf{u}^{z}$ with $z \in \mathcal{Q}$ and it can be seen as the forced response. Obviously $\boldsymbol{\Delta}\mathbf{i}^{\emptyset} = \boldsymbol{\delta}\mathbf{i}^{\emptyset}$.

It is worth noticing that $\boldsymbol{\delta}\mathbf{i}^{\emptyset}$ depends on the actual currents and speed, i.e. $\boldsymbol{\delta}\mathbf{i}^{\emptyset} = f(\mathbf{i}^{k}, \omega)$. Besides, the second term $\boldsymbol{\delta}\mathbf{i}^{z}$ depends on the currents (that affect the inductance value), on the direct and quadrature voltages that change with the index z and the electrical rotor position ϑ, i.e. $\boldsymbol{\delta}\mathbf{i}^{z} = f(\mathbf{i}^{k}, z, \vartheta)$. In other words, given a voltage vector (that means fixing z), the relative current variation $\boldsymbol{\Delta}\mathbf{i}$ varies with the current, the speed and the position. In particular, it is possible to express the current variations by splitting them in the two dq components obtaining

$$\begin{aligned} \Delta i_d^{z} &= \delta i_d^{\emptyset}(\mathbf{i}^{k}, \omega) + \delta i_d^{z}(\mathbf{i}^{k}) \cdot \cos(\vartheta - \vartheta_z) \\ \Delta i_q^{z} &= \delta i_q^{\emptyset}(\mathbf{i}^{k}, \omega) + \delta i_q^{z}(\mathbf{i}^{k}) \cdot \sin(\vartheta - \vartheta_z) \end{aligned} \tag{3.3}$$

where ϑ_z is the position of the eight voltage vectors in the $\alpha\beta$ plane. At steady state, i.e. with constant current $\mathbf{i}^{k}$ and speed ω, the variations (3.3) can be represented as the sum of a constant offset and an oscillating term with constant amplitude. Fig. 3.2 reports this situation.

It is worth highlighting that if the values stored in the LUT have been recorded several time intervals before, i.e. with a different machine state, they are not reliable anymore and they could strongly differ from the correct values. In this case, the cost function evaluation, and in turn the choice of the next voltage vector, is based on wrong values and lead to an incorrect machine operation.

The proposed updating method is based on the following remarks. At each step, i.e. fixed the currents, the speed and the position, (i) the null state component $\boldsymbol{\delta}\mathbf{i}^{\emptyset}$ is the same for all the vectors $\boldsymbol{\Delta}\mathbf{i}^{z}$. Besides, due to the rotor anisotropy, (ii) the eight

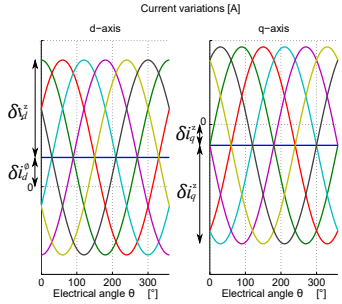

Figure 3.2: Current variations at steady state

vectors $\boldsymbol{\delta}\mathbf{i}^z$ are placed along an ellipse in the dq plane. The idea is then to combine three measured vectors $\boldsymbol{\Delta}\mathbf{i}^z$ and, exploiting remarks (i) and (ii), to reconstruct the others.

It is worth mentioning that (i) and (ii) hold considering the vectors $\boldsymbol{\Delta}\mathbf{i}^z$ at the same instant, i.e. for the same currents,speed and position. During the real drive operation, the current variations are obtained at different instants introducing an approximation. For this reason, a suitable algorithm for the sequence identification has to be designed in order to guarantee a frequent update of the LUT as will be explained in Sec. 3.4.

A qualitative representation of remarks (i) and (ii) is provided in Fig. 3.3.

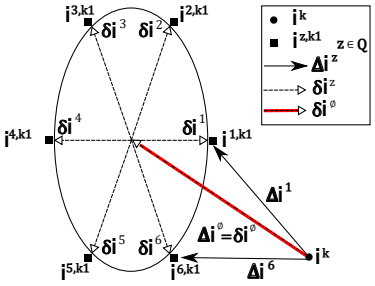

Figure 3.3: Vectorial representation

Five different sequences $s =< s_1, s_2, s_3 >$ composed by three measured vectors can be used to for a complete LUT update, i.e. estimating the other four older values. In the following, the sequences are expressed considering $z = 1$ as the minimum index of the triplets. The results can be easily extended to $z \in \mathcal{Q}$ by mean of a proper index shifting and rotation.

Combining a maximum of three current variations given by active vectors it is possible to obtain the value related to the null vector in three different ways. These relationships are used in each one of the five possible sequences to reconstruct the missing values starting from the most recent current variations. In particular, the null vector can be obtained combining (i) two opposite vectors (example in Fig. 3.4(a)), (ii) three consectutive vectors (example in Fig. 3.4(b)) or (iii) three vector with a phase shift of $2/3\pi$ (example in Fig. 3.4(c)).

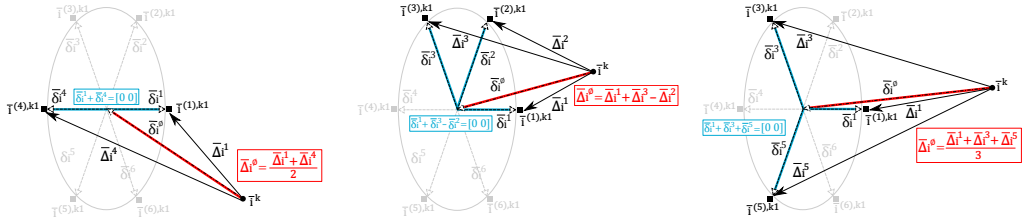

(a) Two opposite vectors (b) Three consecutive vectors (c) Three vectors with a $2/3\pi$ phase shift

Figure 3.4: Combination of $\bar{\delta}i^z$ resulting in the null vector [0 0]

Sequence 1

Composed by three consecutive active vectors, e.g. $s =< 1, 2, 3 >$ as shown in the example of Fig. 3.5(a). The LUTs can be updated with

$$\begin{aligned} \boldsymbol{\Delta}\mathbf{i}^{\emptyset} &= \boldsymbol{\Delta}\mathbf{i}^{1} + \boldsymbol{\Delta}\mathbf{i}^{3} - \boldsymbol{\Delta}\mathbf{i}^{2} \\ \boldsymbol{\Delta}\mathbf{i}^{4} &= 2\boldsymbol{\Delta}\mathbf{i}^{\emptyset} - \boldsymbol{\Delta}\mathbf{i}^{1} \\ \boldsymbol{\Delta}\mathbf{i}^{5} &= 2\boldsymbol{\Delta}\mathbf{i}^{\emptyset} - \boldsymbol{\Delta}\mathbf{i}^{2} \\ \boldsymbol{\Delta}\mathbf{i}^{6} &= 2\boldsymbol{\Delta}\mathbf{i}^{\emptyset} - \boldsymbol{\Delta}\mathbf{i}^{3} \end{aligned} \tag{3.4}$$

First, the variaton of the null vector is found combining the three consecutive vectors (as in Fig. 3.4(b)). After that, by inverting the relationship between two oppostite active vectors and the null vector (as in th example of Fig. 3.4(a)), it is possible to find the current variations related to the three other active vectors.

Sequence 2

Composed by three active vectors with two opposite, e.g. $s =< 1, 2, 4 >$ as shown in the example of Fig. 3.5(b). The LUTs are„ updated with,

$$\begin{aligned} \boldsymbol{\Delta}\mathbf{i}^{\emptyset} &= \frac{1}{2}(\boldsymbol{\Delta}\mathbf{i}^{1} + \boldsymbol{\Delta}\mathbf{i}^{4}) \\ \boldsymbol{\Delta}\mathbf{i}^{3} &= \boldsymbol{\Delta}\mathbf{i}^{2} + \boldsymbol{\Delta}\mathbf{i}^{4} - \boldsymbol{\Delta}\mathbf{i}^{\emptyset} \\ \boldsymbol{\Delta}\mathbf{i}^{5} &= 2\boldsymbol{\Delta}\mathbf{i}^{\emptyset} - \boldsymbol{\Delta}\mathbf{i}^{2} \\ \boldsymbol{\Delta}\mathbf{i}^{6} &= 2\boldsymbol{\Delta}\mathbf{i}^{\emptyset} - \boldsymbol{\Delta}\mathbf{i}^{3} \end{aligned} \tag{3.5}$$

The response to the null vector is obtained combining the two available opposite vectors (as in Fig. 3.4(a)). After that, the active vector consecutive to two af the available vectors (in this case $z = 3$) can be found by inverting the relationship expressed in Fig. 3.4(b). The othe two missing values, namely 5 and 6 are computed exploiting the relationship between two opposite vectors.

Sequence 3

Composed by two active consecutive vectors and a null vector, e.g. $s =< 1, 2, 0 >$ as shown in the example of Fig. 3.5(c). The LUTs can be updated with

$$\begin{aligned} \boldsymbol{\Delta}\mathbf{i}^4 &= 2\boldsymbol{\Delta}\mathbf{i}^{\emptyset} - \boldsymbol{\Delta}\mathbf{i}^1 \\ \boldsymbol{\Delta}\mathbf{i}^5 &= 2\boldsymbol{\Delta}\mathbf{i}^{\emptyset} - \boldsymbol{\Delta}\mathbf{i}^2 \\ \boldsymbol{\Delta}\mathbf{i}^3 &= \boldsymbol{\Delta}\mathbf{i}^2 + \boldsymbol{\Delta}\mathbf{i}^4 - \boldsymbol{\Delta}\mathbf{i}^{\emptyset} \\ \boldsymbol{\Delta}\mathbf{i}^6 &= 2\boldsymbol{\Delta}\mathbf{i}^{\emptyset} - \boldsymbol{\Delta}\mathbf{i}^3 \end{aligned} \tag{3.6}$$

First, the vectors in opposition with the two available active vectors can be found inverting the relationship expressed in Fig. 3.4(a). Then, combining one of the known value ($z = 2$) and one reconstructed ($z = 4$) with the null vector, it is possible to find the vector consecutive to the considered two active vectors. The last value is found exploiting the relationship in Fig. 3.4(a).

Sequence 4

Composed by two active vectors with a phase shift of $2/3\pi$ and a null vector, e.g. $s =< 1, 3, 0 >$ as shown in the example of Fig. 3.5(d). The LUTs can be updated with

$$\begin{aligned} \boldsymbol{\Delta}\mathbf{i}^2 &= \boldsymbol{\Delta}\mathbf{i}^1 + \boldsymbol{\Delta}\mathbf{i}^3 - \boldsymbol{\Delta}\mathbf{i}^{\emptyset} \\ \boldsymbol{\Delta}\mathbf{i}^4 &= 2\boldsymbol{\Delta}\mathbf{i}^{\emptyset} - \boldsymbol{\Delta}\mathbf{i}^1 \\ \boldsymbol{\Delta}\mathbf{i}^6 &= 2\boldsymbol{\Delta}\mathbf{i}^{\emptyset} - \boldsymbol{\Delta}\mathbf{i}^3 \\ \boldsymbol{\Delta}\mathbf{i}^5 &= 2\boldsymbol{\Delta}\mathbf{i}^{\emptyset} - \boldsymbol{\Delta}\mathbf{i}^2 \end{aligned} \tag{3.7}$$

The three availabe values are used to find the vector between the two known active. After that, similarly to Sequence 1, the next step consists in finding the missing vectors by mean of the relationship that links two opposite vectors and the null.

Sequence 5

Composed by three active vectors with a mutual phase shift of $2/3\pi$, e.g. $s =< 1, 3, 5 >$ as shown in the example of Fig. 3.5(e). The LUTs can be updated with

$$\begin{aligned} \boldsymbol{\Delta}\mathbf{i}^{\emptyset} &= \frac{1}{3}(\boldsymbol{\Delta}\mathbf{i}^1 + \boldsymbol{\Delta}\mathbf{i}^3 + \boldsymbol{\Delta}\mathbf{i}^5) \\ \boldsymbol{\Delta}\mathbf{i}^2 &= 2\boldsymbol{\Delta}\mathbf{i}^{\emptyset} - \boldsymbol{\Delta}\mathbf{i}^5 \\ \boldsymbol{\Delta}\mathbf{i}^4 &= 2\boldsymbol{\Delta}\mathbf{i}^{\emptyset} - \boldsymbol{\Delta}\mathbf{i}^1 \\ \boldsymbol{\Delta}\mathbf{i}^6 &= 2\boldsymbol{\Delta}\mathbf{i}^{\emptyset} - \boldsymbol{\Delta}\mathbf{i}^3 \end{aligned} \tag{3.8}$$

The first step allows finding the null vector component with the expression in Fig. 3.4(b). After that, the other three vectors are found as the opposite of both available measured and reconstructed values.

All the other sequences that do not start with element 1 can be connected with the sequences represented in Fig. 3.5. In particular this can be done by sorting in ascending

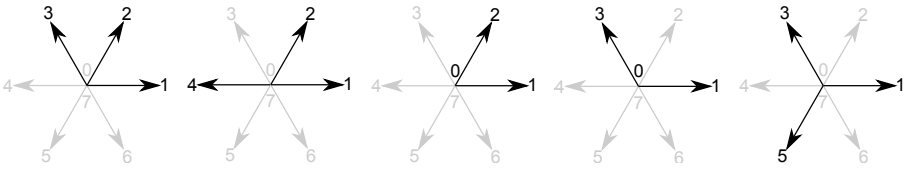

(a) Sequence 1 (b) Sequence 2 (c) Sequence 3 (d) Sequence 4 (e) Sequence 5

Figure 3.5: Voltage vector sequences

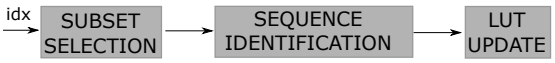

Figure 3.6: Sequence identification flowchart

order the elements of the general sequence. At this point the first element $s[1]$ is the minimum index included in the sequence. After that all the elements of are subtracted by the quantity $s[1] - 1$. In this way, for each possible triplets, a new sequence is obtained. The latter starts with index 1 and keeps the same spatial displacements between the three vectors of the original sequence. It is worth mentioning, that if the triplets already has minimun element equal to 1, then the subtraction has no effect since $s[1] - 1 = 0$.

3.4. Sequence Identification

A proper algorithm for the sequence identification has been developed considering the following requirements. First, it has to recognize whether the voltage vectors obtained by the cost function minimization form a suitable sequence. Besides, it has to record the order in which the vectors are chosen. This implies that, considering the five cases defined in Sec. 3.3 and only one null vector, 192 different sequences are eligible to update the LUT. Finally, the algorithm must be suitable for real time applications.

The core is described in Algorithm 1. The 192 triplets are stated as in the previous section with $s =< s_1, s_2, s_3 > \in \mathcal{S}$ and for each of them, a flag f_s is introduced. The input voltage vector index idx is compared with $s[f_s]$ and f_s is updated accordingly (lines 5 and 6). When a triplet is completed, i.e. when all its three elements are found, the LUT update is executed (lines 10 and 11). After the update is performed, the first element of the identified sequence $s[1]$, i.e. the oldest voltage vector, is discarded to obtain a reliable update during the machine operation (line 12). The set $\mathcal{A}$ includes all the indexes that at each step can be used to form a suitable sequence, i.e. those vectors that have already been chosen by the cost function mminimization (line 7) and that have not been discarded after the LUT update.

To reduce the computational burden, the algorithm has to be selective to avoid the evaluation of all the 192 different triplets at each step. For this reason,the sequence identification is made considering only the sequences $s \in \mathcal{S}_{idx,j} \subseteq \mathcal{S}$, where the subset is defined as $\mathcal{S}_{i,j} \equiv \{s \in \mathcal{S} | \exists k, s[k] = i \wedge s[1] = j\}$. This means reducing the research to all the sequences including idx and starting with q. The basic idea is that a sequence is evaluated either if its first element is idx and $idx \notin \mathcal{A}$ or if its first element is $q \neq idx$ and $q \in \mathcal{A}$ (line 4).

Algorithm 1 Sequence Identification

Input: idx: is the current voltage vector index. $S_{idx,q}$ is the subset containing idx and starting with $q \in \mathcal{Q}$. $\mathcal{A}$ is the subset including all the indexes that can be used to form a triplet, $f_s \forall s$
for each $q \in \mathcal{Q}$ **do**
    for each $s \in \mathcal{S}_{idx,q}$ **do**
        if $(q \in \mathcal{A} \wedge q \neq idx) \vee (\text{idx} \notin \text{A})$ **then**
            if $idx == s[f_s]$ **then**
                $f_s \leftarrow f_s + 1$
$\mathcal{A} \leftarrow \mathcal{A} \cup \{idx\}$
for each $q \in \mathcal{Q}$ **do**
    for each $s \in \mathcal{S}_{idx,q}$ **do**
        if $f_s == 3$ **then**
            function LUT UPDATE
            $\mathcal{A} \leftarrow \mathcal{A} \backslash \{s[1]\}$

A schematic representation of the algorithm is reported in Fig. 3.6. As explained, it consists of three main parts. The first (subset selection), allows reducing the total number of sequence evaluations considering the new input index idx. The core of the algorithm is idenfied with the block sequence identification, in which the indexes are compared with the eligible sequences and the relative flags are updated. Finally, whether a sequence is identified, the LUT are updated accordingly.

An example of the algorithm operation is reported in Fig. 3.7. On the left, the output of the cost function minimization are listed step by step. On the right, the operation of the algorithm are briefly described. In the example, at the first step, the input index is 1. The algorithm, update the flag of all the sequences starting with it. At the second step, the input is index 4. The flags of the sequences starting with this index are updated. Besides, the sequences starting with 1 and with 4 in the second position are as well updated. At the next step, the input is 0. The sequences starting with this index, and those starting with 4 and having 0 in the second position, are updated. Since, $s =< 1, 4, 0 >$ is not a possible sequence it is not possible to update the LUT at this step. At the last step, the input index is 2. At this point, the sequence $s =< 4, 0, 2 >$ is identified and it will be used for the LUT update. The first element of the sequence, namely 4, is then discarded. This means that this index is not available anymore for the LUT update. The simple example represented in Fig. 3.7 demostrate the behaviour

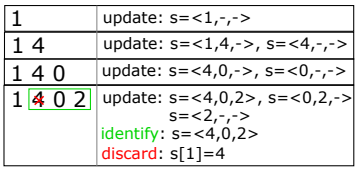

Figure 3.7: Example of the sequence identification

of the algorithm. It is worth highlighting that, after the first element of the identified sequence is discarded (4 in the example), there still could be older indexes (1 in the example). This could represent an issue since the LUT update could be performed using

old index despite the discarding method employed. On the other hand, discarding all the older values would require the knowledge of the age of the indexes, or at least the order in which the indexes are put inside the set $\mathcal{A}$. This solution has not been implemented because it would make the algorithm more complex, going againts the requirement of applicability in real time applications. Besides, the analysis of the results obtained during the preliminary tests, confirmed that the implemented solution is sufficiently efficient and that it does not suffer from the above mentioned issue.

Fig. 3.8 shows the d-axis LUT without and with the proposed updating method. A speeds step test has been performed in the simulation. Red solid lines are analytically computed and compared with the values obtained with the current variation measurements (blu dashed lines). It is worth highlighting that without any method to prevent and avoid stagnation, the loss of control occurs. This effect can be recognised because the red lines are not sinisoids anymore at the end of the test. This happens since the currents do not track the references commanded by the speed regulator to produce the required torque. In this situation, the speed gradually decrease until it becomes zero. On the contrary, thanks to the proposed anti-stagnation technique, the LUT are continuously updated obtaining a precise and reliable prediction, which in turn guarantees the proper operation of the machine.

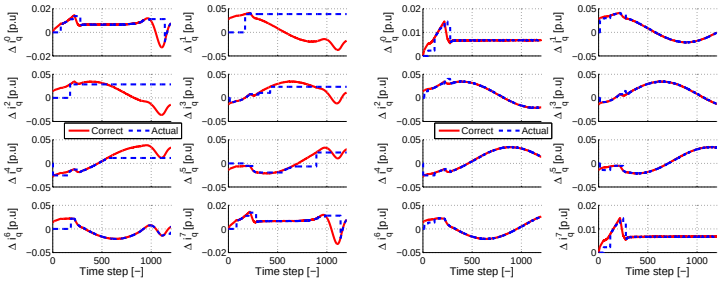

(a) LUT w/i stagnation (b) Updated LUT

Figure 3.8: Effectiveness of the proposed algorithm

3.5. Model validation

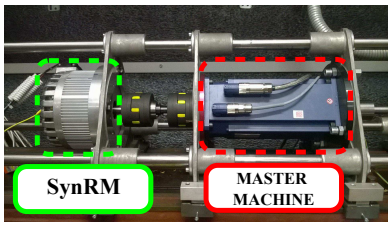

Figure 3.9: Experimental set-up

The proposed scheme has been implemented on the experimental setup of Fig. 3.9 with a sampling time of $T_s = 200[\mu s]$ and the main data of the SynRM are reported in Table 3.1. The steady state performance have been evaluated and compared with

Table 3.1: Motor data

Pole pair number	p	2
Phase resistance	R	4.5 Ω
Direct inductance	L_d	60 mH
Quadrature inductance	L_q	190 mH
Nominal current	I_N	10 A_{pk}

a traditional MBPCC scheme. Fig. 3.11 shows the results obtained at constant speed $n = 100$ [rpm] and for different loads. The current references are generated considering an ideal unsaturated machine, i.e. assuming a linear Maximum Torque Per Ampere (MTPA) trajectory. Obviously, due to iron saturation,the actual MTPA differs from the ideal one and for this reason the machine operation is not optimal. However, tracking the actual trajectory requires the precise knowledge of the machine model. Although the choice of using the ideal MTPA has evident drawbacks, e.g. more Joule losses and reduced maximum torque capability, it allows keeping the scheme completely free from the model.

A first test has been performed to verify the effectiveness of the proposed MFPCC. In particular, a transition between the Model-based and the Model-free prediction has been done during the steady state operation of the machine. The results are reported in Fig. 3.10 where the instant when the transition is executed can be easily recognised (step $k = 500$). It is worth highlighting that after the transition the ripple is reduced in both axes. The effect is more evident in the quadrature axis, where iron saturation causes a remarkable mismatch between between the actual and the nominal model used for the prediction. During the MBPCC stage, the LUT are updated with the proposed anti-stagnation method, but they are not used for the prediction.

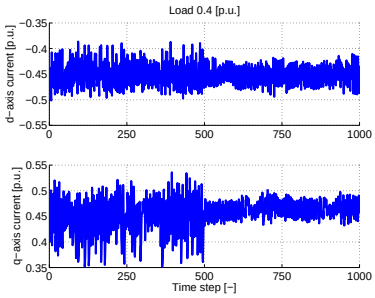

Figure 3.10: Transition between MBPCC and MFPCC

Fig. 3.11(a) shows the dq current waveforms of the MBPCC and the proposed MFPCC. It can be seen that at low load, the performance of the two schemes are comparable in terms of ripple. In this situation, the d-axis presents an higher ripple due to the rotor anisotropy, i.e. $L_q > L_d$. At higher loads, iron saturation is more intense and the effects are mainly in the quadrature axis. As a consequence, the model used for the prediction is significantly different in the q-axis while the d-axis is less subject to iron saturation. The last plot of Fig. 3.11(a) shows that a wrong model used in the prediction causes

an increase in the current ripple, confirming the analysis presented in [2]. This effect is heavier in the quadrature axis where the inductance is overestimated. At low loads, the current ripple is higher in the axis presenting the lower inductance, namely the d-axis. Depending on the strength of the iron satuation and in turn on the parameter mismatch, the current waveforms could present the opposite behaviour, i.e. the ripple is higher in the other axis. As can be seen, the MFPCC does not present the same effect and the current ripple does not change with the load.

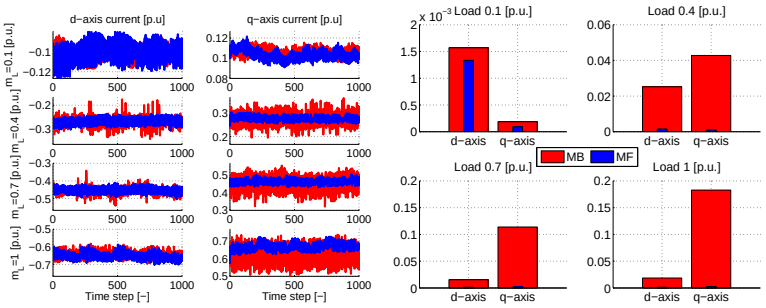

(a) Current waveforms (b) ISE criterion

Figure 3.11: Experimental results at 100 [rpm] and different loads

A detail of the prediction accuracy is shown in Fig. 3.12. Here, the red solid line and the blu dashed line represent the actual and the predicted current. It can be seen that, the predicted values is accurate since it perfectly replies the waveform of the measured current but one step in advance. The prediction accuracy of the two schemes is compared in Fig. 3.11(b) by mean of the Integral Squared Error (ISE) criterion. It can be seen that for the MBPCC, the higher the load the higher the prediction error caused by the mismatch in the model. Besides, the q-axis error is higher than the d-axis one. The MFPCC errors are constant and do not change in the four tests. The effectiveness of the model free prediction is particularly evident in the last. The results clearly show that the prediction is reliable in every working condition.

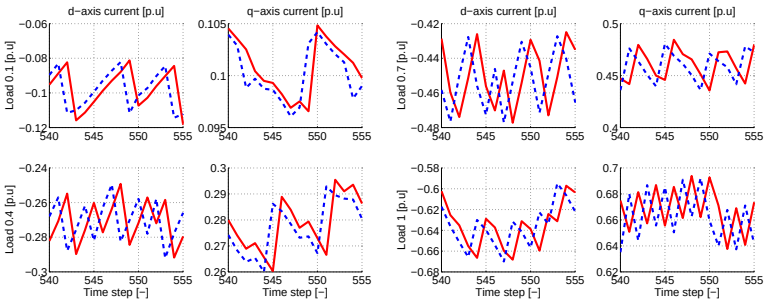

(a) Low load (b) High load

Figure 3.12: Detail of the prediction accuracy

Fig. 3.13 and Fig. 3.14 show the output of the cost function minimization and the number of switching per step for both the MBPCC and the MFPCC. It can be noticed that switching pattern of the two schemes in the test with load $0.1[p.u.]$ is very

similar. This confirms that the nominal model used for the prediction in the MFPCC is sufficiently precise in this working condition. Differently, at higher loads, the cost function chooses different voltage vectors in the two schemes. In particular, the MFPCC does not present changes between opposite vectors, i.e. no transitions that requires 3 commutations are involved.

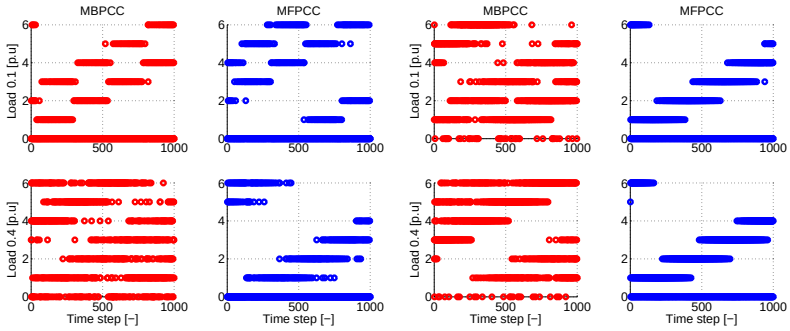

(a) Low load (b) High load

Figure 3.13: Cost function ouput

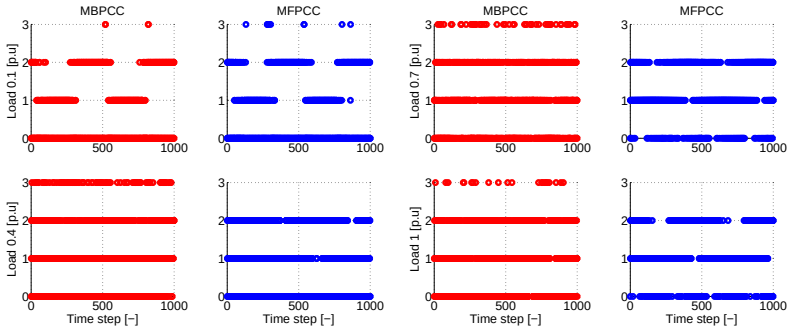

(a) Low load (b) High load

Figure 3.14: Number of commutation per step

Fig. 3.15 shows the LUT for the tests with load and high. It can be seen that, the update is frequent and effective and allows obtaining smooth current variation waveforms.

3.6. Limitations and inherent stagnation

The results shown in the previos section highlihghted the feasibility of the proposal. Besides, the comparison with the MBPCC confirmed its effectiveness. Nevertheless, it is worth mentioning which have been the difficulties encountered during the implementation and which are the situations that represent a criticality for the MFPCC.

First, it exists a combination of three indexes that does not allow the LUT update. In particular, for all the triplets that can be represented as the one in Fig. 3.16, i.e. the sequences composed by two opposite vectors and a null vector, it is not possible to

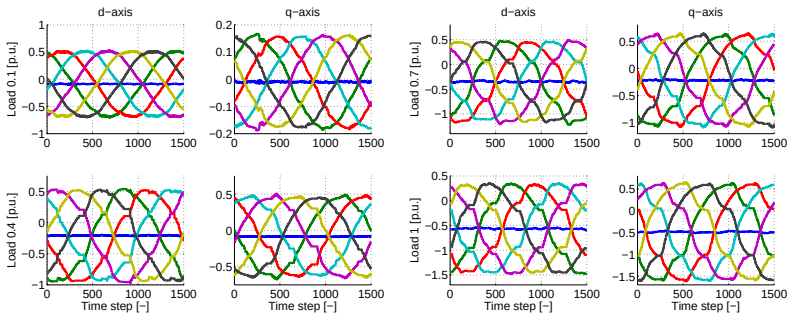

(a) Low load (b) High load

Figure 3.15: Current variations LUT

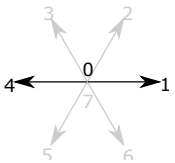

Figure 3.16: Unsuitable sequence

reconstruct the other unknown values. However, it is unlike that this situation actually represent a criticality during the MFPCC operation. The reason can be qualitatively explained as follows. The predictive regulator inherently brings the point of work as close as possible to the reference and, once it reaches it, it tends to remain close to it. It is highly unlike that two opposite vectors that cause opposite responses are alternately and uniquely, together with the null vector, chosen as the optimal.

A significant criticality concerns situations in which the stagnation is unavoidable. The proposed anti-stagnation solution is based on the identification of sequences composed by triplets of voltage vectors indexes. As a consequence, if no sequences are identified, the proposed method cannot work. The results shown in Sec. 3.5, confirmed that during the normal machine operation, a sufficent number of sequences are identified to guarantee the stable operation of the drive. On the other hand, particular operations, such as fast transients involving big current errors, could represent an obstacle to the proper operation of the MFPCC. Precisely, in presence of current steps, the same voltage vector could be chosen for a number N of interval. During this time, only one value of the LUT is updated, while the others are not since no triplets are formed. For this reason, if after N steps the actual state of the machine is drastically changed, the Model-free prediction will lead the machine to unexpected operations. The higher the value of N the higher the risk of instability. (it is worth highlighting that this situation represents a criticality even for the MFPCC proposed in [9], since their method would apply six non optimal vectors consecutively).

The prediction used by the predictive current regulator in the proposed MFPCC is based on the measured current variations. Since this, the current aquisition has to be precise and free from high frequency noises otherwise the values stored in the LUT and then used in the prediction are not reliable. It has to be noticed that, if a wrong value is stored in the LUT, this could be later used to update all the current variations

related to old voltage vectors, resulting in a diffusion of the error in the whole table. It is worth mentioning that the presence of offset in the measurements does not represent a criticality for the control scheme. The reason is that, every possible constant offset is eliminated by the current subtraction. On the other hand, high frequency noise could affect the behaviour of the scheme. To prevent any wrong operation caused by the presence of noise in the measured waveforms, the LUT have been low-pass filtered. This solution allows avoiding erroneous spikes in the values stored in the LUT. The time constant of the filter has to be properly designed in order to cut the high frequency noise while not introcing delays in the current variation waveforms . As already explained in Sec. 2.2.4, the disturbance given by the switching can be avoided by properly placing the current sampling. This can be done by shifting the synchronization of the interrupt service routine. On the other hand, in the experimental setup of the laboratory (see Fig. 3.9), two machines are simultaneously controlled, namely the SynRM and the master. The two power converters are not isolated since they share the ground connection. Besides, although the sampling times used in the two are the same (or are multiples), there still are some slight differences. For these reasons, the disturbances introduced by the commutations of the inverter of the master machine affect the current measurements of the SynRM. Since the small difference between their frequencies, the disturbance is not fixed in a certain position of the sampling time of the SynRM but it slides from the beginning to the end. It is clear that, it is not possible to avoid this kind of homopolar disturbance by easly placing the current samplings in a proper position. This means that, periodically, i.e. when the disturbance occur in correspondance to the current samplings, the three-phase currents will be affected by it. Often in three-phase system, only two currents are measured while the third is obtained by subtracting the other two as shown in (3.9) where i_a, i_b, i_c are the actual current, i_a^s, i_b^s, i_c^s are the sampled values and Δi is the homopolar disturbance. If this method is emplyed, the disturbance on the abc three phase system is then transferred to the equivalent two phase system and the control scheme is consequently affected. This effect is shown in considering the Clark transformation in (3.10), where it can be seen that even the two phase currents include a term given by the homopolar disturbance.

$$\begin{cases} i_a^s &= i_a + \Delta i \\ i_b^s &= i_b + \Delta i \\ i_c^s &= -i_a^s - i_b^s = \underbrace{-i_a - i_b}_{i_c} - 2\Delta i \end{cases} \tag{3.9}$$

$$\begin{cases} i_\alpha^s &= \frac{2}{3}\left[i_a^s - \frac{1}{2}i_b^s - \frac{1}{2}i_c^s\right] = \frac{2}{3}\left[i_a - \frac{1}{2}i_b - \frac{1}{2}i_c + \frac{3}{2}\Delta i\right] \\ i_\beta^s &= \frac{\sqrt{3}}{3}\left[i_b^s - i_c^s\right] = \frac{\sqrt{3}}{3}\left[i_b - i_c - \Delta i\right] \end{cases} \tag{3.10}$$

Differently, if all the three currents are measured (3.11) the disturbance is not transferred to the two phase system (3.12). For this reason, this solution has been adopted in the implementation.

$$\begin{cases} i_a^s &= i_a + \Delta i \\ i_b^s &= i_b + \Delta i \\ i_c^s &= i_c + \Delta i \end{cases} \tag{3.11}$$

$$\begin{cases} i_\alpha^s &= \frac{2}{3}\left[i_a^s - \frac{1}{2}i_b^s - \frac{1}{2}i_c^s\right] = \frac{2}{3}\left[i_a - \frac{1}{2}i_b - \frac{1}{2}i_c\right] \\ i_\beta^s &= \frac{\sqrt{3}}{3}\left[i_b^s - i_c^s\right] = \frac{\sqrt{3}}{3}\left[i_b - i_c\right] \end{cases} \tag{3.12}$$

Another possible solution that allows having two only current measurements while avoiding homopolar disturbance in the two phase system, consists in measuring two current differences as shown in (3.13) and the consequent two phase transformation results as in (3.14).

$$\begin{cases} i_a^s - i_b^s &= i_a - i_b \\ i_b^s - i_c^s &= i_b - i_c \end{cases} \tag{3.13}$$

$$\begin{cases} i_\alpha^s &= \frac{2}{3}\left[(i_a^s - i_b^s) + 1/2(i_b^s - i_c^s)\right] = \frac{2}{3}\left[i_a - \frac{1}{2}i_b - \frac{1}{2}i_c\right] \\ i_\beta^s &= \frac{\sqrt{3}}{3}\left[i_b^s - i_c^s\right] = \frac{\sqrt{3}}{3}\left[i_b - i_c\right] \end{cases} \tag{3.14}$$

Another strong limitation of the proposed method is represented by the computational burden. Althought the sequence identification algorithm does not include complex calculations, i.e. only logical comparisons and additions are executed, the big number of sequences that have to be evaluated causes an increase of the turnaround time. The real time application is obviously constrained by the sampling time, i.e. the complete algorithm has to be executed in a time interval lower than T_s.

During the implementation of the algorithm in the experimental setup, a number of overruns occured with $T_s = 100[\mu s]$. Not every test was affected by this kind of fault. The reason can be found on how the algorithm is made selective. As explained in Sec. 3.4, the number of sequences that have to be evaluated at each step depends on the input index and on the elements of the set $\mathcal{A}$. As a consequence, during a certain test, the size of the selected sequence subset could or could not cause the overrun of the real time application.

In order to avoid accidental overrun situations, to have stable experiments and reproducible results, the sampling time has been increased to $T_s = 200[\mu s]$. This choice has some significat effects on the proper operation of the proposed MFPCC. In particular, as explained in Sec. 3.3, the relationship that links the current variations and that is used to update the LUT is based on the assumption that the eight values are taken at the same instant. If this hypothesis does not hold, the vectors of the current variations are not placed on an ellipse. During the real operation, the values are stored in the LUT at different instants, that means introducing an approximation. Obviously, the smaller the time intervals between the current variation measurements the less the impact introduced by the approximation. Due to the real time constraint and the consequent choice of $T_s = 200[\mu s]$, this implementation of the MFPCC does not allow the stagnation avoidance during certain operations. In particular, it has been found that stagnation could occur during high speed tests or fast dynamics.

3.7. Startup

At the machine startup, when no current variations have been measured yet, the LUT are empty. In this case, the current prediction cannot be obtained. In [8] and [9] the startup of the MFPCC is not addressed. Here, two different solutions are proposed.

A first easy solution could be represented by a Model-based startup. In particular, during the first steps the model could be used to predict the currents. Either after a certain number of steps or after the LUT have been updated for the first time, the control could be switchted to the Model-free prediction. It is worth highlighting that using fixed number of steps as the criterion for the transition could not be suitable for all the operation of the machine. The reason is that the time interval in which the model-based prediction is used could be suitable during certain tests, allowing the LUT to be updated before the model-free prediction is started, but it could be not so during other tests. In other words, the choice of this threshold is not unique and it is based on the experience of the designer. Besides, the main drawabck is that this method would require the knowledge of the machine parameter. Although a mismatch between the model and the actual plant could be reasonably accepted for a limited number of time steps, in this part of the work it has been decided to completely exclude every solution that requires the knowledge of the model, achieving a completely model-free control scheme. For this resojn, the model-based startup has not been implemented.

A suited startup procedure has been developed and implemented. The idea is to output all the eight voltage vectors before the machine is started. In this way the LUT are filled and the machine can start running using the prediction based on the stored current variation measurements. The sequence of indexes during this procedure has to avoid that the currents increase or decrease reaching dangerous level for the machine. To do this a sequence of opposite vectors is provided. For the sake of clarity a numerical simulation has been carried out and the results are shown in Fig. 3.17. It can be seen that the sequence is ordered to provide opposite vectors, i.e $1-4$, $2-5$ and $3-6$. In this way the current variations have opposite directions, avoiding dangerous level for the machine. The sign of the current variation under each voltage vector depends on the position of the machine, in this case $\vartheta_{me} = -\pi/2$. In the example, each index is given for 10 steps to clearly show the results. It is worth highlighting that the same procedure could be done applying each index for just one step.

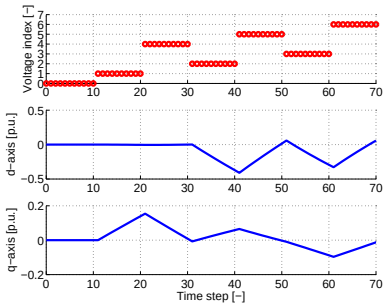

Figure 3.17: Simulated startup procedure

The proposed startup procedure has been implemented and tested and the results are reported in Fig. 3.18. The detail of the startup procedure are shown in Fig. 3.18(b).

It can be seen that after the latter is executed, a speed step is given as a reference to the speed regulator. A constant load of $0.3[p.u.]$ is provided by the master machine. Thanks to the suited procedure, the predictive regulator is able to recognize which vector is the best to reduce the current error and in turn to track the speed reference.

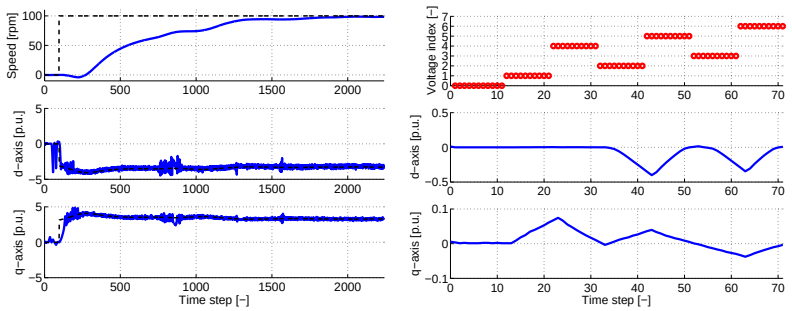

(a) Speed and currents (b) Detail of the startup

Figure 3.18: Startup procedure

3.8. Conclusions

In this chapter, the effects of voltage vector stagnation on MFPCC schemes have been evaluated. An example of what happens in presence of infrequent LUT update has been provided.

A novel updating method has been presented. This technique allows reconstructing all the current variations using only the values related to the three most recent voltage vectors. The proposed solution is based on the relationship linking the current variations given by the eight voltage vectors. The latter can be exploited to reconstruct the older values in the LUT starting from the most recent stored current varitions. The relationship holds under the assumption that all the eight values are taken at the same instant. Differently, during the machine operation, the current variations are obtained at different steps, introducing an approximation that is negligible if the time between the considered values is sufficiently short. For this reason, a suitable algorithm for the sequence identification has been developed and implemented. The aim of the latter is to recognize wheter the voltage indexes pattern forms a suitable sequence for the LUT update. The algorithm has been developed considering the strict constraint given by the real time application. In particular, the number of possible sequences that has to be evaluated is reduced depending on the input voltage index.

The proposed algorithm has been validated by mean of experiments.The results have been compared with MBPCC based on the nominal model of the SynRM to highlight the effectiveness of the proposed scheme even under the effect of parameter variations. In particular, the tests have been performed with different loads to evaluate the behaviour of the scheme with strong iron saturation. The results clearly showed the benefits of the Model-free prediction. In particular, the prediction error is greatly reduced and, as a consequence, the current waveforms present a reduced ripple.

The limitations of the proposed control scheme have been evaluated. In particular,

it has been highlighted the presence of situations in which stagnation is unavoidable, i.e. when no sequences can be identified and used for the LUT update. This actually represents a significant criticality. Besides, since the prediction is based on the measured current variations, the presence of noises or disturbances could affect the performance of the drive. In the implementation, three current measurements and a low-pass filter for the LUT have been used to avoid issues related to high frequency noises and homopolar disturbances introduced by the power converter of the master machine. Another, significat issue is given by the computational burden. In order to avoid overrun faults, the sampling time has been doubled.

Finally, a procedure for the startup has been proposed. In this condition, the LUT are empty meaning that the predictive regulator cannot evaluate the effect of the eight voltage vectors. The drawbacks given by a model-based startup have been highlighted and, after that, a suited procedure has been implented. The latter allows filling the LUT before the machine startup.

Chapter 4

Model Predictive Hysteresis Current Control

In this chapter, a Model Predictive Hysteresis Current Control scheme for Synchronous Reluctance machine is presented. The proposed algorithm predicts the plant behaviour considering the finite set of the power converter states and it chooses the most suitable voltage vector in order to minimize the cost function. The latter is designed to meet different goals depending on the operating conditions of the machine. In particular the Maximum Torque Per Ampere trajectory, the Flux Weakening region and the Maximum Torque Per Voltage operation are considered. In this way, a wide speed range operation is achieved and the current and voltage limits are inherently observed. Besides, after the cost function outputs a certain voltage vector, the same vector is kept until the error amplitude goes beyond a fixed threshold. For this reason, the proposed scheme belongs to Hysteresis control.

4.1. Introduction

The conventional Direct Torque Control (DTC) is a technique based on the control of the torque and the stator flux vector module without needing current loops. In those schemes, a speed regulator provides the two references and the main controller acts to keep torque and flux errors within an hysteresis band [16]. Well known merits of these schemes are the simple and robust control structure and the fast torque dynamic which are in contrast with the high torque and current ripples and the variable switching frequency. Besides, short sampling time is required to keep the torque within the hysteresis region [17, 18].

In further development of the conventional scheme, the switching of the inverter is not based on the torque and flux hysteresis controller but on the minimization of a cost function. This represents a migration of DTC towards Model Predictive Control (MPC) and it can be identified as MP-DTC [19–24].

Several works presented DTC schemes for SynRM as for instance [25]. This machine tipology features an inherent wide speed range operation. Therefore, an effective control

scheme for SynRM machine should exploit the machine capabilities in all operative conditions. In particular, depending on the speed of the machine, the Maximum Torque Per Ampere (MTPA), the Flux Weakening (FW) and Maximum Torque Per Voltage (MTPV) trajectories have to be tracked. A DTC scheme for SynRM able to control the machine in all the aforementioned regions is presented in [26]. The scheme is based on the duty ratio regulation introduced in [27] which allows reducing the torque ripple retaining the dynamic performance of the conventional DTC. Besides, an adaptive stator flux reduction algorithm based on the status of the duty ratio is proposed for FW operation.

In this work an advanced control scheme for wide speed operation of SynRM machine is presented. The machine is controlled to accurately track the MTPA, the FW and the MTPV trajectories by introducing the *operating line*. This is a locus of operating points located between MTPA and MTPV trajectories; it coincides with former for speed lower than the base speed, i.e. voltage lower than the nominal one, while it coincides with the latter for the highest speed up to the maximum drive speed.

Differently from conventional DTC schemes, the algorithm does not consider the torque and flux errors for the decision of the most suitable voltage vector. Instead, the current amplitude error and the distance from the operating line are used to build a complex error which in turn is used to compute a cost function to be minimized each time the error amplitude exceeds a given threshold. The first term of the complex error is evaluated comparing the reference provided by the speed controller and the measured currents. The second component is obtained evaluating the distance between the actual point of work and the operating line.

Increasing the speed, the transition between the MTPA and FW is obtained by rotating the operating line from the MTPA up to the MTPV trajectory by mean of an innovative voltage loop. Conventional voltage loop are based on the knowledge of the base speed, which in turn requires the machine parameters under every working condition. Disturbance, parameter uncertainties and variations could lead to a severe worsening of the drive performance or to a non fully utilization of the DC bus [26].

In order to overcome these issues, in this chapter it is proposed an adaptive algorithm able to drive the machine at high speed reducing the machine flux. The algorithm is based on the fact that when the bemf becomes larger than the available voltage, the control strategy can not find a voltage vector able to bring the error back inside the limit. Therefore, the repetitive violation of a specific convergence criterion can be used as an index.

Since the choice of the voltage vector to be applied is based on the minimization of the cost function which depends on the complex error composed by (i) the current amplitude error and (ii) the distance from the operating line, the proposed control scheme is referred as a Model Predictive Hysteresis Current Control (MP-HCC). Besides, it belongs to the class of FC since it predicts the machine behaviour considering the eight possible inverter states.

It is worth highlighting that the proposed control strategy relies on the knowledge of the machine parameter for every working condition.

4.2. Proposed control scheme

The overview of the proposed control scheme is reported in Fig. 4.1. This is composed by a speed regulator (PI_n), a voltage loop (VL) and the MP-HCC logic block which represents the core of the scheme.

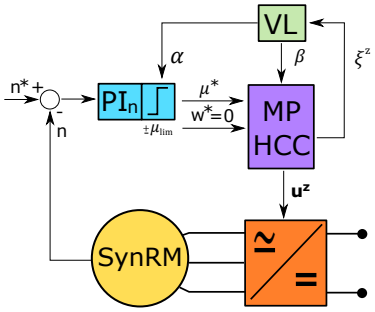

Figure 4.1: Control scheme

4.2.1. Speed loop

The output of the PI speed controller is defined in (4.1) and it includes the current vector amplitude $|I^*|$ and the sign of the torque demand m^*. This quantity represents the current amplitude command to track the speed reference n^*. The limits $\pm\mu_{lim}$ (4.2) of the regulator depend on the external voltage loop parameter α and are described in Sec. 4.2.4.

$$\mu^* = |I^*| \cdot sign(m^*) \tag{4.1}$$

$$\mu_{lim} = \pm\alpha \cdot I_N \tag{4.2}$$

The difference between the reference μ^* and the actual value μ estimated from the measured currents represents the first component of the complex error introduced in Sec. 4.2.3.

4.2.2. Operating line

A linear SynRM model is here considered for the sake of simplicity. In this case, the MTPA and the MTPV trajectories are straight lines in the dq-current plane as defined in (4.3) and (4.4) respectively, where $i_d \leq 0$ and $i_q > 0$ is for motor operation.

$$i_q = \pm i_d \tag{4.3}$$

$$i_q = \pm\frac{L_d}{L_q} \cdot i_d \tag{4.4}$$

Starting from this, the idea developed in this work is to obtain the reference trajectory by rotating the MTPA. To do this, the operating line w has been defined in two different ways. The first (4.5), separately considers the distance from the MTPA and the MTPV, stated with w_{MTPA} and w_{MTPV} respectively, and then it takes a weighted

sum of the two terms. The second (4.6), is obtained starting from the point to line distance formula. In particular, $s_L(\beta)$ is the slope of a general line through the oring between the MTPA and the MTPV. In both the definitions, the rotation is obtained by mean of the parameter β which is the output of the voltage loop described in Sec. 4.2.4.

$$\begin{aligned} w &= \beta \cdot w_{MTPA} + (1-\beta) \cdot w_{MTPV} \\ w_{MTPA} &= i_d^2 - i_q^2 \\ w_{MTPV} &= i_d^2 - \left(\frac{L_q}{L_d}\right)^2 i_q^2 \end{aligned} \tag{4.5}$$

$$\begin{aligned} s_L(\beta) &= \frac{sign(m^*)}{\beta\left(\frac{L_q}{L_d} - 1\right) - \frac{L_q}{L_d}} \\ w(\beta) &= \frac{|i_q - s_L(\beta) i_d|}{\sqrt{1 + s_L(\beta)^2}} \end{aligned} \tag{4.6}$$

According to the two different definitions of the operating line, the hysteresis band has been represented in the dq current plane in Fig. 4.2. The magenta and the black circles represent the hysteresis band computed with (4.5) and (4.6) respectively. It is worth noticing that, using the definition (4.5), despite the hysteresis band is a circle in the error plane, its shape results deformed in the current plane depending on the point of work. This could result in a improper track of the current reference and a different behaviour could be obtained in the two axes depending on the point of work. On the contrary, (4.6) allows obtaining a regular shape in the whole plane.For this reason, the latter has been chosen and implemented.

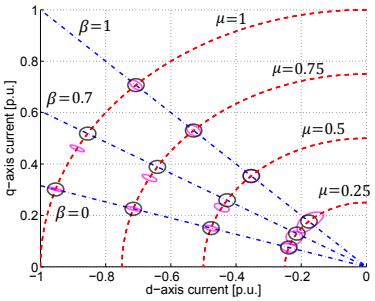

Figure 4.2: Hysteresis band in the dq current plane

The distance between the actual point of work and the operating line represents the second term of the complex error defined in Sec. 4.2.3.

It is worth noticing that the definition of the quantity w can be easily extended to the case of saturated machine, provided that the MTPA and MTPV loci are given. In particular, a solution suitable for its ease of implementation, consists in linearizing the actual trajectories of the machine as qualitatively represented in Fig. 4.3. Here, the MTPA and the MTPV are linearized considering the intersection between the actual curves and the current circumference limit. Using the linearized trajectories introduces an approximation. On the contrary, the base point and the starting point of the MTPV are the same of the actual curves. The great advantage of this simplified solution is

given in terms of ease. First, it does not require the complete knowledge of the machine magnetic characteristics since only two points are needed, namely the intersections of the actual curves with the current circumference. Besides, with the linearized curves, the same algorithm presented for the linear case can be used, i.e. the same definition of operating line (4.5) ca be used.

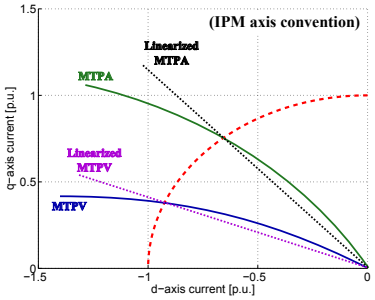

Figure 4.3: Actual and linearized trajectories

4.2.3. MP-HCC logic

The core of the scheme is the MP-HCC logic block. From the control stage, the block receives as input μ^* from the speed controller, the reference of the distance from the operating line $w^* = 0$ and the coefficient β from the voltage loop. Furthermore, the currents and the position are measured from the machine and provided to the MP-HCC block. The output is the voltage vector $\bar{u}_j$ which is directly applied to the power converter.

Similarly to [28], an error vector $\mathbf{E} = [E_\mu \; E_w]^t$ is introduced (4.7), where E_μ, E_w are the normalized error components, E is the error amplitude and ϕ_E its phase.

$$\begin{aligned} E_\mu &= \frac{\mu^* - \mu}{I_N} \qquad E_w = \frac{w^* - w}{I_N^2} \\ E &= \sqrt{E_\mu^2 + E_w^2} \qquad \phi_E = tan^{-1}\left(\frac{E_w}{E_\mu}\right) \end{aligned} \tag{4.7}$$

The target of the control is to observe (4.8), i.e. keeping the module of the error within a circumference of radius E_{max}.

$$E \leq E_{max} \tag{4.8}$$

If at instant k, E reaches the limit, the control acts on the feeding voltage in order to bring the point of work inside the limit circle. In particular, the voltage vector at the next step $k+1$ is choosen among one of the eight possible inverter state $\mathbf{u}^z$ with $z \in \mathcal{Q}$ in order to reduce the error E so that (4.8) is observed again. The selected voltage vector $\mathbf{u}^{k1}$ has to guarantee a reduction of E, i.e. the convergence condition is obtained by imposing a negative derivative of the error amplitude(4.9), where the dot stands for derivative.

$$\begin{aligned} &\frac{d}{dt}E \leq 0 \\ &\frac{d}{dt}\sqrt{E_\mu^2 + E_w^2} = \frac{E_\mu \dot{E}_\mu + E_w \dot{E}_w}{E} \leq 0 \end{aligned} \tag{4.9}$$

Different criteria can be adopted for the choice of the voltage spatial vector if more than one meets (4.9). They follow different requirements, e.g. reducing the switching frequency or the switching losses. In [28] the algorithm chooses the spatial vector that minimize (maximum negative) the derivative of the error (4.9). Differently, in this work the control strategy predicts the trajectory of the working point for the eight possible voltage vectors $\mathbf{u}^z$, and it selects the one that keeps the error within the limit for the longest time.

The MP-HCC operation can be described as follows. At instant k the currents $\mathbf{i}^k$ and the speed ω^k are measured while the voltages $\mathbf{u}^k$ are known from the previous step *k-1*. The dq currents at the next sampling time $\mathbf{i}^{k1|k}$ are predicted with (2.10) and (2.2). The predicted currents are used to calculate μ^{k1}, w^{k1} and the errors E_μ^{k1}, E_w^{k1}, E^{k1} as well. If the predicted error observes (4.8), then the next applied voltage vector is the same as in the actual step. Otherwise, the derivative of the error is computed for the eight possible inverter states $\mathbf{u}^z$ with $z \in \mathcal{Q}$. Knowing the latter, it is possible to estimate the error trajetories and the time ΔT^z in which the point will stay within the limit E_{max}. The chosen voltage vector is the one that entails the maximum value of ΔT^z and it will be activated at instant *k+1*. Therefore the cost function f to be minimized is reported in (4.10).

$$f = \frac{1}{\Delta T^z} \tag{4.10}$$

For the sake of clarity, the operation of the algorithm are represente in Fig. 4.4.

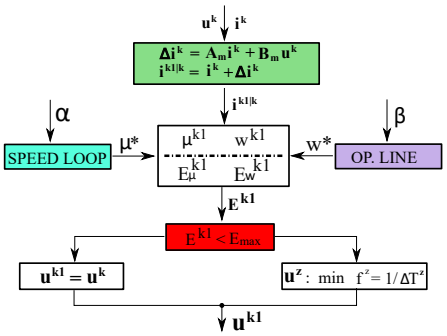

Figure 4.4: Representation of the MPHCC operation

The value of ΔT^z can be computed as follows. Let $\mathbf{E}$ be the error at instant k, defined as in (4.7). Predicting the error at the next instant *k+1*, it is possible to compute the derivative $\dot{\mathbf{E}}^z = [\dot{E}_\mu \ \dot{E}_w]^t$ expressed as in (4.11). The amplitude $\dot{E}^z$ is the speed ν^z by which the operating point moves in the error plane along the direction of $\dot{\mathbf{E}}^z$.

Fig. 4.5 represents the point of work and its trajectory in the error plane assuming $E = E_{max}$. Here, φ^z is the angle between the error and its derivative and γ^z is its complementary as expressed in (4.12).

$$\dot{E}^z = \sqrt{(\dot{E}_\mu^z)^2 + (\dot{E}_w^z)^2} \qquad \phi_{\dot{E}^z} = tan^{-1}\left(\frac{\dot{E}_w^z}{\dot{E}_\mu^z}\right) \tag{4.11}$$

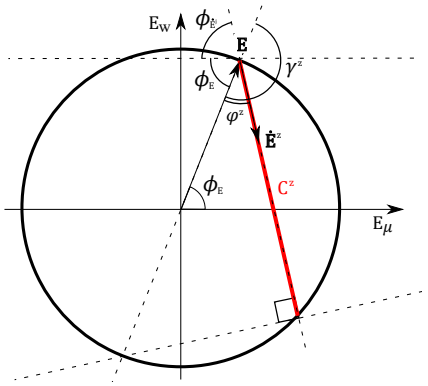

Figure 4.5: Error plane

$$\varphi^z = \pi - \gamma^z \quad and \quad \gamma^z = \phi_E + \phi_{\dot{E}^z} \tag{4.12}$$

Assuming the speed ν^j constant, the point moves along the chord C^j remaining within the circumference for a time ΔT^j computed in (4.13).

$$\Delta T^z = \frac{C^z}{v^z} = \frac{2E_{max} \cdot cos(\varphi^z)}{\dot{E}^z} \tag{4.13}$$

4.2.4. Voltage loop

Beyond the base speed, the bemf becomes larger than the available DC bus. In this condition, the MP-HCC searches for the best voltage vector able to shift the error within the circumference with no avail. This behaviour can be used to distinguish whether it is necessary to weak the flux of the machine.

The condition reported in (4.9) is not suitable to be used as a criterion to rotate the operating line. Although observing the latter condition means finding a vector that reduce the error amplitude, it does not imply the convergence to the circumference. In other words, observing the amplitude reduction only is not sufficient and the error direction has to be considered as well.

Fig. 4.6 shows the general case when the error $\mathbf{E}$ lies outside the limit E_{max}. A suitable voltage vector is able (i) to reduce the error amplitude and (ii) to shift the point towards the limit circle. This represents a constraint on the value of the angle γ^z defined in (4.12) and it can be expressed as in (4.14) as a function of $\varphi^z_{lim} = sin^{-1}(E_{max}/E)$. The latter delimits the feasible area for the error at the next instant $\mathbf{E}^{k1}$. In the example depicted in Fig.4.6, the error at *k+1* has a smaller amplitude but the trajectory does not cross the circumference, i.e. condition (4.9) is observed while (4.14) is not.

$$\begin{gathered} \gamma^z \in \pi \pm \varphi^z_{lim} \\ cos(\gamma^z) < -cos(\varphi^z_{lim}) \\ \xi^z = E_\mu \dot{E}^z_\mu + E_w \dot{E}^z_w + \dot{E}^z \cdot \sqrt{E^2 - E^2_{max}} < 0 \end{gathered} \tag{4.14}$$

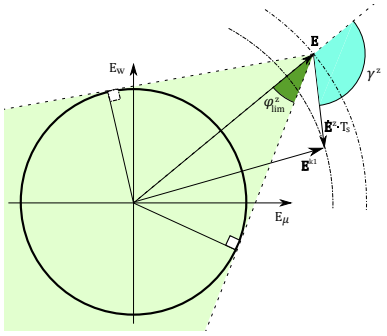

Figure 4.6: Example of the error feasible area

Condition (4.14) is always observed when the machine is below the base speed while it does not hold when the bemf reaches the maximum available voltage. Due to this fact, (4.14) represents the criterion to recognize whether it is necessary to weak the flux of the machine and it can be used to drive the machine along the FW and the MTPV trajectories. In particular, the algorithm monitors the value of ξ^z and it regulates the operation of the machine acting on the parameter η accordingly. The logic can be described as follows: if there is at least one voltage vector observing (4.14), i.e. $\xi^z < 0$, this event is recorded increasing the value of the counter $cnt_\eta \geq 0$. A second counter cnt_{cycle} is updated at every iteration. After N_{cycle} steps, if $cnt_\eta = 0$ it means that during the considered interval the MP-HCC never found a suitable voltage vector and the parameter η is reduced of a quantity $\Delta\eta$. On the contrary, if $cnt_\eta = N_{cycle}$ it means that at every instant at least one voltage vector $\mathbf{u}^z$ observed (4.14). If this is the case, the algorithm tries increasing the value of η. After N_{cycle} steps the counters cnt_η and cnt_{cycle} are zeroed and the process is repeated.

It is worth mentioning that the performance of the algorithm strongly rely on the proper tuning of the parameters N_{cycle} and $\Delta\eta$.

The algorithm flow chart is reported in Fig.4.7. It is worth highlighting that $\eta \in [-1; 1]$: the upper bound of the interval implies the MTPA operation while the lower limit is achieved for the machine maximum speed.

Starting from the value of η two different coefficients are introduced. The first, namely α, is used to limit the speed controller output μ^* within the range $\pm\alpha \cdot I_N$ as previously described in (4.2).

The second output β is used to rotate the operating line from the MTPA to the MTPV trajectory, as described in Sec.4.2.2.

For the sake of clarity, the behaviour of the voltage loop and the values of the three parameter η, α and β are reported in Fig. 4.8 for different points of work, namely the MTPA, the FW region and the MTPV trajectory, in the dq current plane.

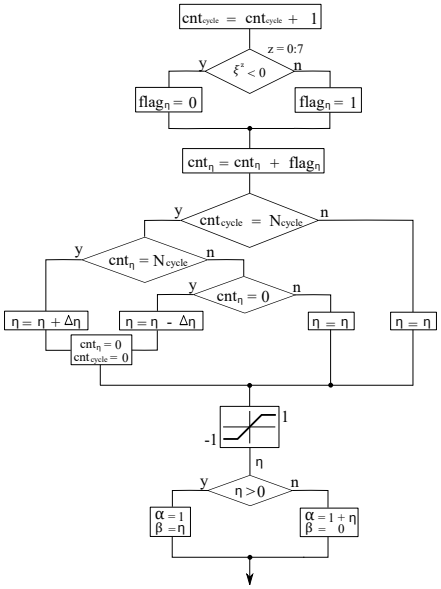

Figure 4.7: VL algorithm flow chart

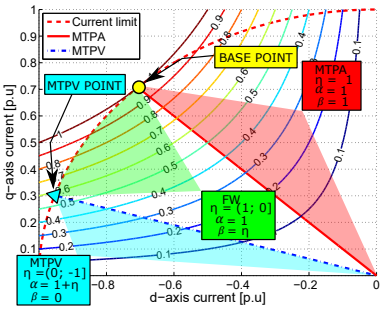

Figure 4.8: Voltage loop operation

4.3. Implementation and Results

The MP-HCC strategy has been implemented and experimentally tested. Fig. 3.9 shows the experimental set-up. The main data of the SynRM and the setting parameters are reported in Table 3.1. The amplitude of the hysteresis band has been fixed to $E_{max} = 2.5e^{-2}$.

A first test has been carried out to verify the current control strategy for all the operative conditions. In particular, the SynRM has been dragged with the master motor with a speed ramp starting from zero to values beyond the base speed. The PI speed regulator of the SynRM machine has been artificially saturated to the maximum value $\mu^* = \alpha \cdot I_N$. In this way, the point of work will start from the base point and will move along the maximum current circumference during FW and along the MTPV trajectory. Since the setting of this experiment, the control strategy can be tested with the machine working at its limits.

The results are reported in Fig. 4.9, where the dq-axis currents and the VL parameter are shown. Here the validity of the control strategy in confirmed, showing that it

is able to drive the machine in the whole speed range.The different operations, namely MTPA,FW and MTPV, are clearly identified.

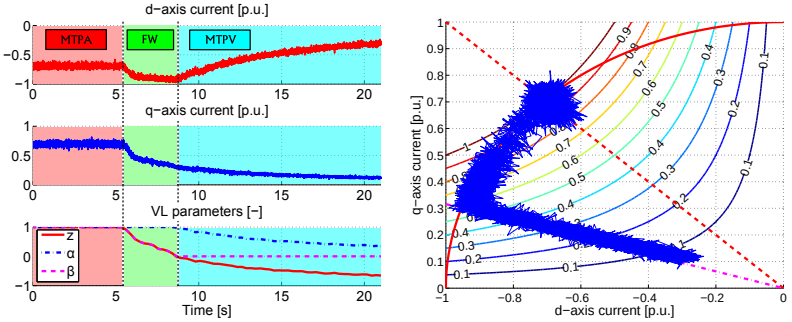

(a) Current response and VL parameters

(b) Complete range operation in dq-current plane

Figure 4.9: First test: control strategy validation

The first test allowed verifing the validity of the model but it does not evaluate the system in its completeness, since the PI speed regulator action has been intentionally excluded. A deeper analysis is required to understand the real performance of the system and in particular the interaction between the speed and the voltage loops, which should not cause oscillations and instabilities.

Fig. 4.10 reports the results obtained providing a constant speed reference to the SynRM. Since this value is below the base speed, providing an increasing braking torque with the master motor implies the movement of the point of work along the MTPA trajectory. During the whole torque ramp, the dq currents closely track the MTPA trajectory and the the VL outputs $\eta = \alpha = \beta = 1$.

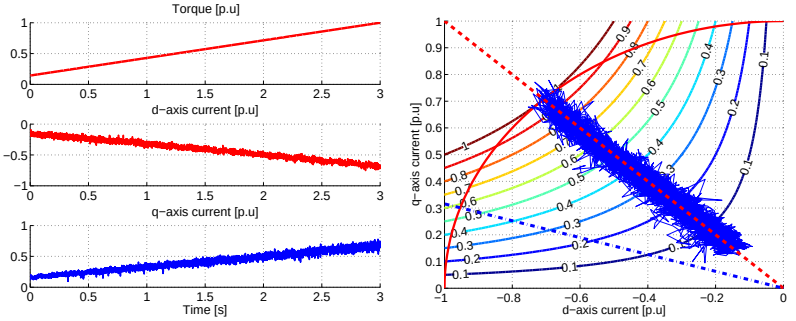

(a) Torque reference and current response

(b) MTPA trajectory in dq-current plane

Figure 4.10: Results of the torque ramp test

Finally, the control scheme has been tested with a speed step. The initial value is below the base speed, while the final reference is beyond it. The results of this experiment are reported in Fig. 4.11. It can be seen that the parameter η and β start decreasing at instant $t = 1[s]$, causing the rotation of the operating line. Its slope is gradually reduced until it coincides with the MTPV line, i.e. $\beta = 0$. After this moment, η goes on decreasing to negative values provoking the reduction of α. The latter has no effect on the currents since they are below the value $\alpha \cdot I_N$ and therefore the actual

current amplitude does not reach the limit circle.

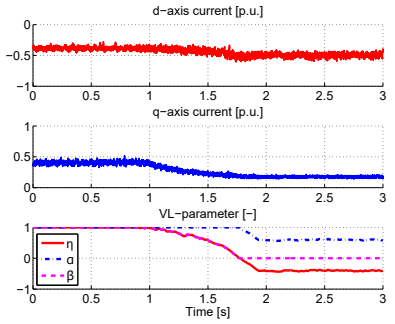

(a) Current and VL parameter

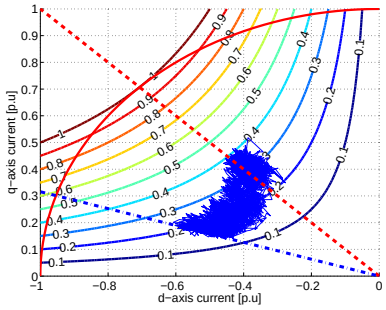

(b) MTPA to MTPV transition in the dq-current plane

Figure 4.11: Results of the speed step test

The switching frequency of the proposed control scheme has been evaluated and compared with that of a traditional Space Vector Modulation (SVM) strategy. Different tests have been executed to verify the behaviour of the scheme in every working condition. The ratio between the number of commutations of the two schemes (defined in (4.15)) has been used as index of comparison. It has been verified that the ratio is in the range $N_{sw} = 4 - 5.5$, meaning that the proposed scheme achieve 4 to 5.5 times lower number of commutations.

$$N_{sw} = \frac{N_{SVM}}{N_{MPHCC}} \tag{4.15}$$

Fig. 4.12 shows the experimental test carried out to evaluate the number of commutation in the MTPA region. Fig. 4.12(a) shows the speed, the currents and the point of work in the dq plane. Fig. 4.12(b) shows the number of switching on each phase and the total. It can be noticed that the commutations are equally distrubuted on the three phases.

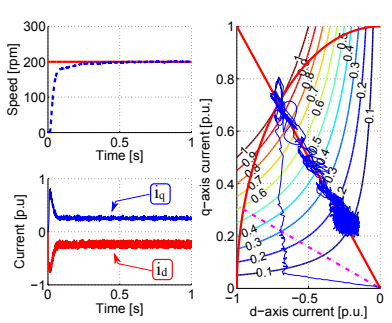

(a) MTPA test

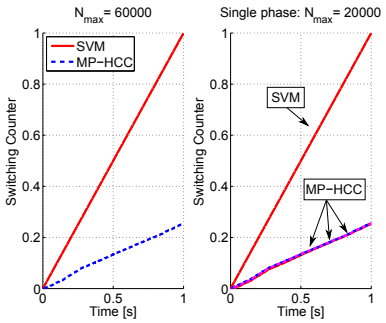

(b) Number of switching

Figure 4.12: Comparison between SVM and MPHCC

It is worth highlighting that the results reported in this section showed a remarkable current ripple. The reason of the latter is twofold. Fist, the prediction is made exploiting the nominal model of the SynRM. As explained in Sec. 2.2.3, this causes an

increased ripple in the current waveforms. Besides, this is an hysteresis based control that inherently presents an higher ripple compared to common current control. The considerations made on the number of switching highlighted that the proposed scheme achieve a lower number of commutations. For this reason, the current ripple could be mitigated by increasing the frequency without exceeding the number of commutations obtained with a traditional SVM control strategy.

The behaviour of the system with $T_s = 30[\mu s]$ has been evaluated with a simulation. The results are reported in Fig. 4.13. It can be seen that the ripple is significantly reduced from 30.8% to 14.8%. Besides, the number of commutations is still lower than in SVM since the ratio is $N_{sw} = 3.3$. Finally, it should be noticed from the last plot of Fig. 4.13(a) that the amplitude of the error E is drastically decreased and it mostly remains below the limit E_{max}. For this reason the hysteresis band amplitude can be reasonably reduced.

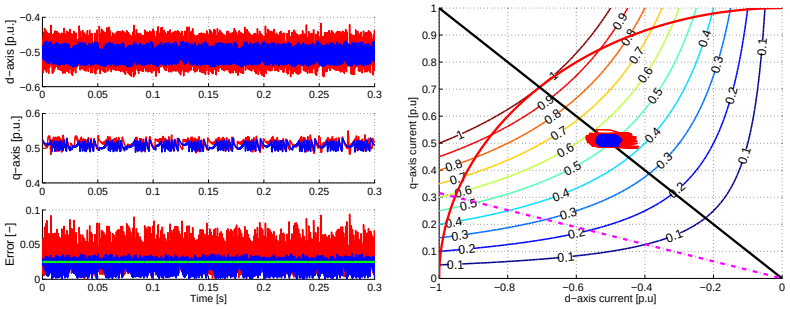

(a) Currents and error

(b) Point of work in the dq current plane

Figure 4.13: Comparison between $T_s = 100[\mu s]$ and $T_s = 30[\mu s]$

The same test has been repeated with halved hysteresis band. The results are shown in Fig. 4.14 where a comparison with case of $T_s = 100[\mu s]$ is reported. Reducing the hysteresis band allows a further decrease of the current ripple. In this test its value is 8.3%. It is worth mentioning that the number of communtation achieved in this test is still lower than SVM and $N_{sw} = 1.5$.

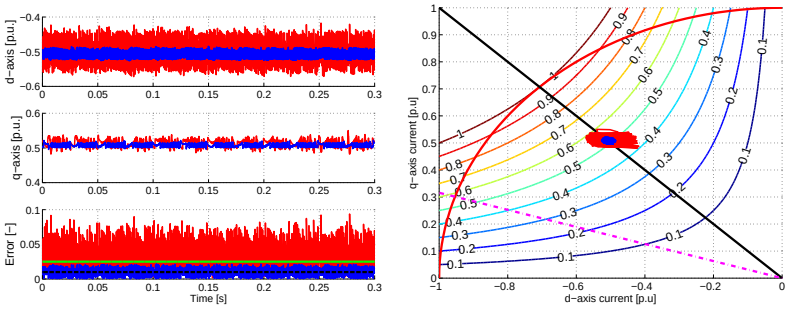

(a) Currents and error

(b) Point of work in the dq current plane

Figure 4.14: Test with halved hysteresis band

4.4. Conclusions

In this chapter an advanced control scheme for wide speed operation of SynRM machine is presented. The scheme belongs to the class of Model Predictive Control since the algorithm is based on the minimization of the cost function. The solution obtained by this process is the one that allows keeping the error within the hysteresis band for the longest time.

The model is developed considering a linear SynRM in both the prediction and in the reference generation, i.e. in the definition of the operating line. Nevertheless, a simplified method to include the effects of iron saturation has been proposed.

The proposed control scheme allows the full exploitation of the synchronous reluctance machine potentials. In particular, it has been shown the effectiveness of the algorithm in all operating points under MTPA, FW and MTPV trajectories. The wide speed capabilities are achieved by rotating the operating line and reducing the PI speed controller limits by mean of an innovative voltage loop. The latter receives information on the error status from the control strategy, it inherently recognizes when the voltage limit is reached and it operates accordingly.

Finally, a comparison with a traditional SVM strategy has been made. In particular, the number of switching of the two schemes has been evaluated. Since the proposed scheme belongs to hysteresis control, fixed the sampling time, the number of commutations is significantly lower than in SVM. This allowed to decrease the sample time to reduce the current ripple. The latter is caused the model-based prediction that relies on the nominal model of the SynRM. Besides, hysteresis control schemes commonly presents an increased ripple.

The control scheme has been described in detail and verified by mean of experiments. The results obtained on the test bench showed its feasibility and its effectiveness. In particular, good performance have been highlighted in the whole speed range and in the transition between different operation of the machine.

Conclusions

In the first part of this work the model of the synchronous reluctance machine has been developed. The electrical equations have been obtained considering the most general case of three phase electrical machine, i.e. the doubly fed three phase machine. It is worth highlighting that this model could represent the behaviour of every kind of synchronous machine, including permanent magnet and reluctance machines. The model has been developed with the only assumption of no hysteresis and no eddy currents. After that, the equations have been obtained introducing the hypothesis of linearity, i.e. neglecting iron saturation. The three phase model has been then transformed in the equivalent two phase system, introducing a general reference frame. The equations have been finally obtained considering a stationary and a synchronously rotating reference frame.

The results obtained for the doubly fed machines, both the three phase and the two phase, have been used to develop the model of the Synchronous Reluctance machine by imposing specific condition on the rotor currents. In particular, taking null rotor currents in the model of the doubly fed machine, it is possible to represent this kind of machine. The analysis reported in this chapter are the basis of this work and are used throughout the thesis.

Predictive Current Control has been described and analysed in the second chapter. Some considerations about the choice of the proper cost function in case of salient machines have been provided considering the biased behaviour in presence of rotor anisotropy. It has been shown that the cost function based on the absolute error could present non optimal behaviour during particular operations, resulting in low dynamics in the axis with the lower inductance. It has been shown that introducing a weighting factor equal to the saliency ratio allows overcoming this behaviour. With this solution, the bias is compensated and the error on the two axes are reduced in a balanced way. The main drawback of this solution is that it requires the knowledge of the saliency ratio, i.e. the values of the inductance. It has been shown that, using a cost function based on the squared error, allows obtaining sufficiently balanced behaviour on both axes without any requirements on the knowledge of the machine parameters. For these reasons, this cost function has been chosen in this work.

The operation of the predictive regulator has been described considering the two step prediction required to compensate for the delays introduced by the digital implementation. After that, both the Model-based and the Model-free prediction have been

presented. In the former case, the effect of parameter mismatch and variation have been investigated. In particular, in Synchronous Reluctance applications, iron saturation has been recognised as the main responsible for model inadequacies.

Model-free prediction has been further analysed in chapter three, providing some considerations on the detrimental effects of voltage vector stagnation. To overcome instabilities and the loss of control given by an infrequent LUT update, a novel updating method has been presented. This technique allows reconstructing all the current variations using only the values related to the three most recent voltage vectors. The relationship between the eight current variations has been used to efficiently update the LUT. A suitable algorithm for the sequence identification has been developed and implemented. The aim of the latter is to recognize wheter the voltage indexes pattern forms a suitable sequence for the LUT update. The algorithm has been developed considering the strict constraint given by the real time application. In particular, the number of possible sequences that has to be evaluated is reduced depending on the input voltage index.

The proposed algorithm has been validated by mean of experiments and the results have been compared with those of traditional Model-based predictive control, to highlight the effectiveness of the proposed scheme even under the effect of parameter variations. In particular, the tests have been performed with different loads to evaluate the behaviour of the scheme with strong iron saturation. The results have clearly shown the benefits of the Model-free prediction. In particular, the prediction error is greatly reduced and, as a consequence, the current waveforms present a reduced ripple.

The limitations and the criticalities of the proposed control scheme have been highlighted. In particular, the presence of situations in which stagnation is unavoidable, the sensitivity to noises and disturbances and the increased turnaround time of this particular implementation are the main issues.

A procedure for the startup has been proposed. In this condition, the LUT are empty meaning that the predictive regulator cannot evaluate the effect of the eight voltage vectors. The drawbacks given by a model-based startup have been highlighted and, after that, a suited procedure has been implemented.

The last part of this work is commited to the development of an advanced control scheme for wide speed operation of Synchronous Reluctance machine. The scheme belongs to both Model Predictive and Hysteresis control since the algorithm is based on the minimization of the cost function and the result of this process is the one that allows keeping the current error within a fixed threshold for the longest time.

The model has been developed considering a linear machine in both the prediction and in the reference generation, i.e. in the definition of the operating line. Nevertheless, a simplified method to include the effects of iron saturation has been proposed.

It has been shown that, the proposed control scheme allows the full exploitation of the Synchronous Reluctance machine potentials in all operating points under MTPA, FW and MTPV trajectories. The wide speed capabilities have been achieved by rotating the operating line and reducing the PI speed controller limits by mean of an innovative voltage loop. The latter receives information on the error status from the control strategy, it inherently recognizes when the voltage limit is reached and it operates accordingly.

A comparison with a traditional Space Vector Modulation strategy has been done. In particular, the number of switching of the two schemes has been evaluated. Since the proposed scheme belongs to hysteresis control, fixed the sampling time, the number of commutations is significantly lower. Consequently, it has allowed to decrease the sample time to reduce the current ripple. The latter is caused by two aspects: hysteresis-based schemes inherently present a increased ripple and besides the current prediction is obtained using the nominal model that does not include the effects of iron saturation.

Future works

This thesis reports a part of the work done during the three years of Ph.D. studies. Being now at the end of this path, I firmly believe that there still are wide room for improvements and further developments, beyond that new open topics. These are some future works that I personally would like to do if my Ph.D. was not limited in time.

Model-free introduces great advantages in terms of accuracy of the prediction. On the other hand, this technique suffers from voltage vector stagnation that could lead to instability if this phenomenon is not taken into account and prevented. In this work, a novel method to guarantee a frequent and precise current variations LUT update has been presented. Nevertheless, as already mentioned, some critical situations, in which stagnation is unavoidable, could occur during the machine operation. Differently, Model-based control features an always stable operation even under the effects of (reasonable) parameters mismatch. For this reason, it could be interesting to use a prediction based on a model in which the parameters are identified during the machine operation. In particular, the same method used for the LUT update could be adapted to develop a suitable parameter identification algorithm, which output could be used to feed the Model-based prediction.

Thanks to method proposed in this work, the LUT contains precise informations about the actual state of the machine. For this reason, the values of the current variations stored in the LUT could be used to recognize whether the voltage limit has been reached. This relevant feature, combined with other solutions developed in this work, could be used to develop a voltage loop for Flux Weakening and Maximum Torque per Voltage operations.

Bibliography

[1] P. Cortes, M. P. Kazmierkowski, R. M. Kennel, D. E. Quevedo, and J. Rodriguez, "Predictive control in power electronics and drives," *IEEE Transactions on Industrial Electronics*, vol. 55, no. 12, pp. 4312–4324, Dec 2008.

[2] H. A. Young, M. A. Perez, and J. Rodriguez, "Analysis of finite-control-set model predictive current control with model parameter mismatch in a three-phase inverter," *IEEE Transactions on Industrial Electronics*, vol. 63, no. 5, pp. 3100–3107, May 2016.

[3] B. Wang, X. Chen, Y. Yu, G. Wang, and D. Xu, "Robust predictive current control with online disturbance estimation for induction machine drives," *IEEE Transactions on Power Electronics*, vol. 32, no. 6, pp. 4663–4674, June 2017.

[4] B. Wang, Z. Dong, Y. Yu, G. Wang, and D. Xu, "Static-errorless deadbeat predictive current control using second-order sliding-mode disturbance observer for induction machine drives," *IEEE Transactions on Power Electronics*, vol. PP, no. 99, pp. 1–1, 2017.

[5] T. TÃ¼rker, U. Buyukkeles, and A. F. Bakan, "A robust predictive current controller for pmsm drives," *IEEE Transactions on Industrial Electronics*, vol. 63, no. 6, pp. 3906–3914, June 2016.

[6] Z. Chen, J. Qiu, and M. Jin, "Adaptive finite-control-set model predictive current control for ipmsm drives with inductance variation," *IET Electric Power Applications*, vol. 11, no. 5, pp. 874–884, 2017.

[7] J. Sawma, F. Khatounian, E. Monmasson, L. Idkhajine, and R. Ghosn, "Analysis of the impact of online identification on model predictive current control applied to permanent magnet synchronous motors," *IET Electric Power Applications*, vol. 11, no. 5, pp. 864–873, 2017.

[8] C. K. Lin, T. H. Liu, J. t. Yu, L. C. Fu, and C. F. Hsiao, "Model-free predictive current control for interior permanent-magnet synchronous motor drives based on current difference detection technique," *IEEE Transactions on Industrial Electronics*, vol. 61, no. 2, pp. 667–681, Feb 2014.

[9] C. K. Lin, J. t. Yu, Y. S. Lai, and H. C. Yu, "Improved model-free predictive current control for synchronous reluctance motor drives," *IEEE Transactions on Industrial Electronics*, vol. 63, no. 6, pp. 3942–3953, June 2016.

[10] P. Cortes, J. Rodriguez, C. Silva, and A. Flores, "Delay compensation in model predictive current control of a three-phase inverter," *IEEE Transactions on Industrial Electronics*, vol. 59, no. 2, pp. 1323–1325, Feb 2012.

[11] M. Siami, D. A. Khaburi, A. Abbaszadeh, and J. RodrÃguez, "Robustness improvement of predictive current control using prediction error correction for permanent-magnet synchronous machines," *IEEE Transactions on Industrial Electronics*, vol. 63, no. 6, pp. 3458–3466, June 2016.

[12] J. Rodriguez and P. Cortes, *Predictive Control of Power Converters and Electrical Drives*. John Wiley & Sons, Ltd, 2012.

[13] J. Rodriguez, J. Pontt, C. A. Silva, P. Correa, P. Lezana, P. Cortes, and U. Ammann, "Predictive current control of a voltage source inverter," *IEEE Transactions on Industrial Electronics*, vol. 54, no. 1, pp. 495–503, Feb 2007.

[14] B. Bogado, F. Barrero, M. R. Arahal, S. Toral, and E. Levi, "Sensitivity to electrical parameter variations of predictive current control in multiphase drives," in *IECON 2013 - 39th Annual Conference of the IEEE Industrial Electronics Society*, Nov 2013, pp. 5215–5220.

[15] S. Kwak, U. C. Moon, and J. C. Park, "Predictive-control-based direct power control with an adaptive parameter identification technique for improved afe performance," *IEEE Transactions on Power Electronics*, vol. 29, no. 11, pp. 6178–6187, Nov 2014.

[16] G. S. Buja and M. P. Kazmierkowski, "Direct torque control of pwm inverter-fed ac motors - a survey," *IEEE Transactions on Industrial Electronics*, vol. 51, no. 4, pp. 744–757, Aug 2004.

[17] R. Morales-Caporal and M. Pacas, "Encoderless predictive direct torque control for synchronous reluctance machines at very low and zero speed," *IEEE Transactions on Industrial Electronics*, vol. 55, no. 12, pp. 4408–4416, Dec 2008.

[18] J. Beerten, J. Verveckken, and J. Driesen, "Predictive direct torque control for flux and torque ripple reduction," *IEEE Transactions on Industrial Electronics*, vol. 57, no. 1, pp. 404–412, Jan 2010.

[19] J. Rodriguez, R. M. Kennel, J. R. Espinoza, M. Trincado, C. A. Silva, and C. A. Rojas, "High-performance control strategies for electrical drives: An experimental assessment," *IEEE Transactions on Industrial Electronics*, vol. 59, no. 2, pp. 812–820, Feb 2012.

[20] T. Geyer, G. Papafotiou, and M. Morari, "Model predictive direct torque control - part i: Concept, algorithm, and analysis," *IEEE Transactions on Industrial Electronics*, vol. 56, no. 6, pp. 1894–1905, June 2009.

[21] H. Miranda, P. Cortes, J. I. Yuz, and J. Rodriguez, "Predictive torque control of induction machines based on state-space models," *IEEE Transactions on Industrial Electronics*, vol. 56, no. 6, pp. 1916–1924, June 2009.

[22] W. Xie, X. Wang, F. Wang, W. Xu, R. M. Kennel, D. Gerling, and R. D. Lorenz, "Finite-control-set model predictive torque control with a deadbeat solution for pmsm drives," *IEEE Transactions on Industrial Electronics*, vol. 62, no. 9, pp. 5402–5410, Sept 2015.

[23] M. Preindl and S. Bolognani, "Model predictive direct torque control with finite control set for pmsm drive systems, part 1: Maximum torque per ampere operation," *IEEE Transactions on Industrial Informatics*, vol. 9, no. 4, pp. 1912–1921, Nov 2013.

[24] ——, "Model predictive direct torque control with finite control set for pmsm drive systems, part 2: Field weakening operation," *IEEE Transactions on Industrial Informatics*, vol. 9, no. 2, pp. 648–657, May 2013.

[25] S.-J. Kang and S.-K. Sul, "Highly dynamic torque control of synchronous reluctance motor," *IEEE Transactions on Power Electronics*, vol. 13, no. 4, pp. 793–798, Jul 1998.

[26] X. Zhang and G. H. B. Foo, "A robust field-weakening algorithm based on duty ratio regulation for direct torque controlled synchronous reluctance motor," *IEEE/ASME Transactions on Mechatronics*, vol. 21, no. 2, pp. 765–773, April 2016.

[27] Y. Ren, Z. Q. Zhu, and J. Liu, "Direct torque control of permanent-magnet synchronous machine drives with a simple duty ratio regulator," *IEEE Transactions on Industrial Electronics*, vol. 61, no. 10, pp. 5249–5258, Oct 2014.

[28] S. Bolognani and A. Faggion, "Effective formulation of the dtc strategy for convergence and stability analysis - the ipm motor drive case study," in *2013 IEEE International Symposium on Sensorless Control for Electrical Drives and Predictive Control of Electrical Drives and Power Electronics (SLED/PRECEDE)*, Oct 2013, pp. 1–8.

Acknowledgments

This Thesis is written in LaTeX.
An electronic version is available at: *http://paduaresearch.cab.unipd.it*